N° d'ordre: 40791 **Année: 2012**

THESE DE DOCTORAT

Université Lille 1, Sciences et Technologies

Ecole Doctorale: Science de la Matière, du Rayonnement et l'Environnement

Discipline : Optiques et Lasers – Physico-chimie – Atmosphère

présentée par

Abdallah CHAHADIH

Photo-croissance organisée de nano-objets métalliques ou semiconducteurs dans les matériaux diélectriques destinés à la photonique

Soutenue le 20 mars 2012, devant le jury composé de :

Pr. Georges WLODARCZAK	Université Lille 1, Sciences et Technologies	Président
Pr. Rachid MAHIOU	Université Blaise Pascal, Clermont-Ferrand	Rapporteur
Pr. Nathalie DESTOUCHES	Université Jean Monnet, Saint Etienne	Rapporteur
Dr. Jean-Philippe BLONDEAU	Université d'Orléans	Examinateur
Dr. Laurence BOIS	Université Claude Bernard Lyon 1	Examinateur
Pr. Mohamed BOUAZAOUI	Université Lille 1, Sciences et Technologies	Directeur de thèse
Pr. Bruno CAPOEN	Université Lille 1, Sciences et Technologies	Co-directeur de thèse
Dr. Odile CRISTINI-ROBBE	Université Lille 1, Sciences et Technologies	Co-directrice de thèse

Thèse effectuée au sein du laboratoire de Physique des Lasers, Atomes et Molécules (PhLAM), UMR CNRS 8523-Université Lille 1, Science et Technologies, 59650 Villeneuve d'Ascq Cedex.

Acknowledgement

I thank God for making impossible things possible for me to finish this study.

I would like to express my deep and sincere gratitude to my supervisor, Prof. Mohamed Bouzaoui for allowing me to join his team, for his expertise, kindness, and most of all, for his patience. It has been an honor to be his Ph.D. student. His wide knowledge and logical way of thinking have been of great value for me. His understanding, encouraging and personal guidance have provided a good basis for the present thesis.

I am grateful to my co-supervisors, Prof. Bruno Capoen and Dr. Odile Cristini-Robbe for their valuable advices, enthusiasms, guidance and constant support during the thesis. They paid great efforts to explain things clearly and simply, as well as drafting of this thesis. Their ideas and concepts have had a remarkable influence on my entire career in the field of nanoscience.

Besides my advisors, I would like to thank the thesis committee for their accepting to be the jury of my Ph.D.

Many thanks go in particular to the Prof. Georges Wlodarczak, director of the PhLAM laboratory for allowing me to do my Ph.D. in the best conditions.

I owe my most sincere gratitude to Dr. Hicham El-Hamzaoui for his valuable advices and friendly help. I would like to thank him for introducing me to nanoscience, and helping with preparation and characterisation of the samples. His extensive discussions and his interesting ideas around my work have been very helpful for this study.

I gratefully acknowledge the funding sources that made my Ph.D. work possible. I was funded by the French Agence Nationale de la Recherche (ANR) in the frame of the POMESCO project (Organized Photo-growth of Metallic and Semi-Conductor Nano-Objects Intended to Optic Devices), the “Conseil Régional Nord Pas de Calais Picardie” and the “Fonds Européen de Développement Economique des Régions”.

During this work I have collaborated with many colleagues for whom I have great regard, and I wish to extend my warmest thanks to all those who have helped me with my work in the PhLAM laboratory. My sincere thanks are due to Dr. Laurent Bigot, Dr. Géraud Bouwmans, Dr.Antoine Le Rouge, Dr. Rémy Bernard, and Dr. Luc Boussekey for their helping in the characterisation of the samples.

I should particularly like to thank Dr. Christophe Kinowski and Dr. Ihsaan Sfecksy for all their friendly help, encouragement and support.

My special gratitude is due to my mother, brothers and sisters for their never ending care, patience, encouragement, support and above all love.

I owe my gratitude to my wonderful fiancee Nour Assi for her never ending love, encouragement and support.

I wish to thank my friends, Ahmad Fakih, Ali Mroue, Lionel Ghaddar, Julian Boudani and Farah kawtharani for helping me get through the difficult times, and for all the emotional support, camaraderie, entertainment, and caring they provided. Special thanks go to my childhood friends Abed Issa and Mortada Al-Armaly for their encouragement, support and sense of humour.

Table of Contents

General Introduction

New directions of modern research have emerged during the last decade, which has been broadly defined as nanoscale science and technology [1, 2]. These new trends involve the ability to fabricate, characterize, and manipulate artificial structures, the features of which are controlled at the nanometer scale. The nano-materials manifest useful properties, which can be exploited in a wide variety of research and development applications. In particular, semiconductor and metallic nanostructures are regarded as strong contenders for the development of the next generation of optical and optoelectronic components [3-6].

Recently, the synthesis of metal and semiconductor nanoparticles has become very important. There is a great interest in controlling their size, shape and structure since these parameters influence their optical and electrical properties. These nanoparticles should be grown inside host matrices, in order to use them in sustainable applications, capable to enhance and to improve the performance of devices like optical fibres, saturable absorbers or optical switchers. One of these matrices is silica, a material presenting an unrivalled combination of purity, high temperature resistance and high optical transparency [7].

The major effort in the synthesis of metallic and semiconductors nanocrystallites inside silica matrices is based on two methods: melting process and sol-gel route. Both methods have been widely used [8-12], and recently, the sol-gel techniques have attracted a great attention due to their low processing temperature, possibility of controlling the size and morphology of particles. Moreover, this process allows the production of variously shaped monolithic materials [7], thin films [13], fibres [14], powders etc.

In this study, attention is mainly focused on the photo-assisted organized growth of metallic and semiconductor nano-objects inside silica materials. The aims of this study were to master the localization and the organization of nano-objects formed inside silica matrices. Up to now, methods for structuring materials at a nanometer scale have been based either on soft chemical processes for self-organization of nano-structures using the laws of hydrodynamics or a random precipitation of nano-crystals during thermal treatment. The “in situ” nanostructuration proposed in this project is based on the combination of laser irradiation and/or heat-treatment. The local character of the matter-light interaction allows the generation of the nucleation centers leading to the formation of nano-objects in selected areas. Hence, it is possible to control the spatial

distribution the nano-crystallites, as well as their mean size. Moreover, we have studied the physical phenomena that occur during the generation and the organization of nano-objects inside the bulk silica: the processes at the origin of the size evolution, the shape and the size distribution depend on the experimental parameters such as doping, laser irradiation or thermal treatment.

Different metals and semiconductors have been studied: Semiconductors like CdS and PbS continue to attract a significant attention because of their tunable optical properties [15,16], which are expected to arise from the confinement of the charge carriers when the particle size becomes of the order of the exciton Bohr radius (a_B) [17]. As a result of this quantum confinement effect, the absorption and photoluminescence wavelengths can be adjusted from the ultraviolet to the infrared region simply by changing the size or the surface states of the quantum dots. On the other hand, glass–metal nanocomposites (Au-SiO_2, Ag-SiO_2 or Cu-SiO_2) are the subject of an ongoing investigation in the literature. It is well known that the optical properties, the absorption in particular, of the nanosized metals differ drastically from the properties of bulk metals. The physical origin of the light absorption by metallic nanoparticles is the excitation of coherent oscillations of the conduction band electrons by light, which is known as surface plasmon resonance [18].

This thesis is structured into four chapters. In the first chapter is presented a general background about the physical properties of semiconductor and metal nanoparticles. The outline of this chapter is as follows. In Section I.1, we explain the origin of the physical properties of semiconductor materials at the nanoscale level, which are different from that of bulk materials. Following this discussion, we give a brief description of quantum confinement effect in semiconductors. Models used to calculate the band gap energy and the optical properties of semiconductors nanocrystallites are presented. In Section I.2, metal nanoparticles and their physical properties are discussed. Herein, attention is mainly focused on the optical properties of metallic nanoparticles and the theories that explain their optical response.

Chapter II is devoted to the synthesis and characterisation of the nanoparticles embedded inside our silica sol-gel matrices. In the first part of this chapter, we provide an overview on the principles of the sol-gel process and on the most interesting products for us, namely porous and dense silica. In Section II.2, we explain the doping methods used to precipitate the semiconductors and metals inside the silica matrices. Incorporation of nanoparticles inside

microstructured optical fibres and the characterisation techniques used in this thesis are presented in section II.3 and section II.4, respectively.

Chapter III presents our results concerning the photo-growth of semiconductor nanoparticles inside porous silica matrices. This chapter is divided into two parts. In the first part, we report on the precipitation of cadmium sulphide (CdS) nanoparticles, while in the second part, we present results concerning the precipitation of lead sulphide (PbS) nanocrystallites. In both parts, our aim was to find the physical phenomena that occurred during the formation of these nano-objects, as well as the parameters that affect the particle size and their optical response.

The last chapter of this thesis concentrates on the precipitation of metallic nanoparticles inside silica sol-gel matrices. This chapter is organized into three sections. Section IV.1 shows our experimental studies about the precipitation of gold and silver nanoparticles embedded inside porous silica matrix under laser irradiation. Section IV.2 reports on silver and copper nanoparticles embedded inside dense silica glasses. In the last section of this chapter, we describe our first attempt to obtain a microstructured fibre doped with copper nanoparticles from a Cu-doped silica bulk matrice.

References

1. N. Lane. J. Nanopart. Res. **3,** 95 (2001).
2. R.F. Service. Science **290,** 1526 (2000).
3. J. Masek, A.Ishida, H. Zogg. IEEE Elec. Device. Lett. **11,** 12 (1990).
4. D. Asunskis, I. Bolotin, A. Wroble, A. Zachary, L. Hanley. Macromol Symp. **268,** 33 (2008).
5. L.Dan, L. Chunjun, L. Yw, Q. Shixiong. J. Lumin. **122,** 549 (2007).
6. S.A. Maier, H.A. Atwater. J. Appl. Phys. **98,** 11101 (2005).
7. H. El Hamzaoui, L. Courthéoux, V. Nguyen, E. Berrier, A. Favre, L. Bigot, M. Bouazaoui and B. Capoen. Mater. Chem. Phys. **121,** 83 (2010).
8. M.G. Ventura, A.J. Parola, A. Pires de Matos. J. Non-Cryst. Solids **357,** 1342 (2011).
9. A.O. Yeshchenko, I.M. Dmitruk, A.M. Dmytrukb, A.A. Alexeenko. Mater. Sci. Eng. B **137,** 247 (2007).
10. C.S. João, M.P. Coelho, A.Ruivo, A. Pires de Matos. Mater. Lett. **64,** 705 (2010).
11. N.N. Parvathy, G.M. Pajonk and A.V. Rao. Mater. Res. Bull. **32,** 397 (1997).
12. B. Capoen, T. Gacoin, J.M. Nedelec, S. Turell and M. Bouazaoui. J. Mater. Sci. **36,** 2565 (2001).
13. Wenyan. et *al*. J. Appl. Phys. **19,** 9553 (2003).
14. L. Bigot, H. El Hamzaoui, A. Le Rouge, G. Bouwmans, F. Chassagneux, B. Capoen and M. Bouazaoui. Opt. Exp. **19**, 19061 (2011).
15. L.C. Voon. Electronic and Optical Properties of Semiconductors: A Study Based on the Empirical Tight Binding Model, Amazon, 1997.
16. A.D. Zdetsis Rev. Adv. Mater. Sci. **11,** 56 (2006).
17. AL.L. Efros and AL. Efros. Sov. Phys. Semicond. **16,** 772 (1982).
18. K.L. Kelly, E. Coronado, L.L. Zhao, G.C. Schatz. J. Phys. Chem. B. **107,** 668 (2003).

Chapter I: Basic Background and Bibliography

Nanostructured materials are witnessing an expanding development and utilization in a variety of applications. They demonstrate a breadth of fundamental properties that can be tailored extensively to design new and adapted functionalities. In particular, nanostructured optical media are regarded as strong contenders for the development of the next generation of ultra-integrated optical and optoelectronic applications. The diversity of the nanoparticles arises from their wide chemical natures, shapes, morphologies and the medium in which the particles are present. Nanoscale particles can be formed from most elements of the periodic table, and they can be classified as insulators, metals or semiconductors. Semiconductor and metallic nanoparticles are of great interest because of their unique electronic nature: they follow quantum mechanical rules which may strongly differ from the laws governing bulk materials.

A wide range of fundamental and collective optoelectronic properties can be realized in the semiconductor nanocrystals by varying the size at the nanoscale level. Specifically, the size-tunable electronic and optical properties arise from the phenomenon of quantum confinement [1], which means that electronic charges are confined to length scales smaller than the Bohr exciton radius (a_B). It gives rise to atomic-like electronic energy levels and opens up the possibility of tailoring the properties not only through varying the chemical composition but also by using the perturbation due to the size [2]. On the other hand, the most striking phenomenon encountered in metal nanoparticles is electromagnetic resonances due to the collective oscillation of the conduction electrons. This so-called Surface Plasmon Resonance (SPR) induces a strong interaction with light, and the wavelength at which this resonance occurs depends on the local environment, shape, size and orientation of the particles [3-5].

In this chapter, we will review and explore in general the physical properties of both semiconductor and metallic nanoparticles. In section I, we will discuss the physical properties of semiconductors at the nanoscale level, the model that have been used to estimate the bang gap energy of the semiconductor nanocrystals and their optical properties. In section II, we will present the physical properties of the metallic nanoparticles. Herein, we will describe in a few words the theories that have been used to model the optical response of the spherical metallic nanoparticles and at the end of this section, we will illustrate the parameters that affect these optical properties.

I.1. Semiconductor Nanoparticles

I.1.1. Semiconductors at nano-scale level

One of the primary motivations for studying nanometer-scale semiconductor crystallites, or nanocrystals, is to understand the physical phenomena in semiconductors which appear at this nanoscale level. This question has been studied not only for its fundamental importance but also for its practical impact. Semiconductor nanocrystals (NCs), also known as quantum dots, are a special class of materials, often composed of atoms from the periodic groups II-VI, III-V or IV-VI. The most notable and interesting property of semiconductor nanoparticles is the large magnitude change in optical properties as a function of particle size. The three-dimensional quantum-size effect, leading to an increase in band gap with a decrease in particle size, is well-known for semiconductor colloids, where the individual colloidal particles are dispersed in a liquid [6].

Narrow band gap semiconductor Nanocrystals embedded in dielectric matrices were also found to behave as quantum boxes when their radii are smaller than their exciton Bohr radius, the circumstances under which their optical properties are strongly modified as compared to bulk [7]. The sustained interest in using unique optoelectronic properties of NCs in devices led to their successful use in optical switches [8], solar cells [9-11], light-emitting diodes (LEDs) [12-14], photodetectors [15, 16], and biological labelling [17]. In particular, by virtue of their large band gap tunability, high luminance efficiency, narrow spectral emission, and high photostability, semiconductor NCs are an attractive choice as luminophores in next-generation LEDs with a highly saturated emission and enhanced luminous power efficiency. Moreover, their compatibility with low-temperature solution processing opens up the possibility of fabricating organic or inorganic hybrid devices at low cost with device performances similar to their all-inorganic counterparts. To summarize, the size, the shape, the capping material and the surface characteristics have strong influence on the properties of the semiconductor nanoparticles [18].

I.1.2. Quantum confinement effect

Width of the band gap is an important parameter of a semiconductor material. In macroscopic semiconductors at ambient temperature, the width of this gap is fixed and intrinsic parameter of the material. However, the situation changes in nanoscale semiconductor particles with sizes of the order or smaller than the Bohr exciton radius (Figure I.1). This size range corresponds to the regime of quantum confinement, for which electronic excitations ‘‘feel’’ the presence of the

particle boundaries and respond to changes in the particle size by adjusting their energy spectra. This phenomenon is known as the quantum size effect, occurring in nanoscale particles that are often referred to as quantum dots (QDs).

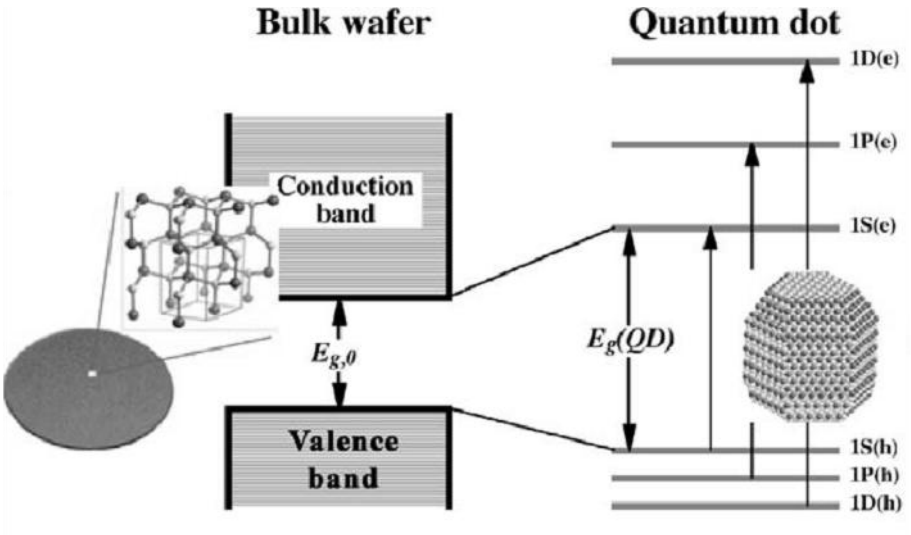

Figure I. 1 *A bulk semiconductor has continuous conduction and valence energy bands separated by a ''fixed'' energy gap, $E_{g,0}$ (left), whereas a quantum dot (QD) is characterized by discrete atomic like states with energies that are determined by the QD radius R (right).*

A quantum dot exhibits 3D confinement, meaning that electrons are confined in all three dimensions. In nature, 3D confinement is found in atoms, so that a quantum dot can be loosely described as an artificial atom [19], which is reflected in the discretization of conduction and valence bands caused by quantum confinement of charge-carriers (Figure I.1, right). This analogy is very important since we cannot readily manipulate regular atoms because they are too small and too difficult to isolate in an experiment. Quantum confinement is vitally important for one thing: it leads to new electronic properties that are not present in today's semiconductor devices. The density of states functions plotted against energy for bulk (3-D), and 0-D systems are shown in Figure I.2, making apparent the continuous energy levels of the bulk and the discrete energy levels for quantum dots.

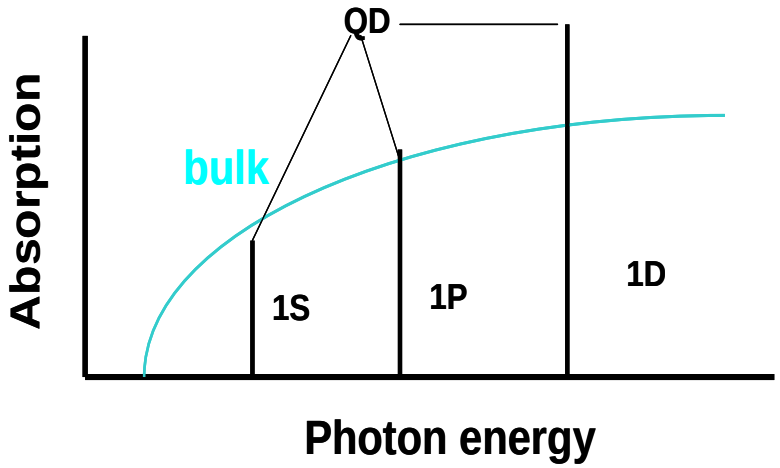

Figure I. 2 *Density of states functions plotted against energy for bulk (3-D blue) and quantum Dot (0-D black).*

Quantitatively, the exciton Bohr radius, a_B, can be expressed as:

$$a_B = \frac{\hbar^2 \varepsilon}{e^2}\left[\frac{1}{m_e} + \frac{1}{m_h}\right] \qquad \textbf{Eq.(I.1)}$$

Where ε is the bulk dielectric constant, $\hbar$ is the reduced Planck's constant, e is the electronic charge, m_e and m_h are the electron and hole effective masses, respectively. This excitonic Bohr radius is the particle typical size for which the confinement effects become important.

I.1.3. Quantum confinement regimes

The quantum confinement regimes in semiconductor nanocrystallites are classified into three regimes (strong, weak and intermediate), depending on the relative size of the crystallites as compared to the exciton Bohr radius. The confinement is strong when the size of crystallites is smaller than the Bohr radius. At this limit, the electron-hole (e-h) Coulomb interaction is negligible and the optical transmissions are determined mainly by the motion confinement of the individual electron and hole. Conversely, the weak confinement occurs if the size crystallite is much greater than the Bohr radius. In this case, the confinement energy is very much less than the coulomb potential energy between the electron and hole. Therefore, in this regime, the both carrier types are confined in the particle. In the intermediate regime, the physical radius of the crystallites is larger than the hole Bohr radius but smaller than the electron one because the effective mass of the holes is generally greater than that of the electrons. In this case, the hole undergoes a weak confinement whereas the electron is strongly confined, not subjected to Coulomb interaction.

I.1.4. Models to calculate the band gap energy

Several models have been proposed to explain the dependence of exciton energy on cluster size [1, 20, 21]. One of them, which is frequently used, is the effective mass approximation model (EMA), first proposed by Efros and Efros [1] and later modified by Brus [20]. It assumes a spherical particle in a potential well with an infinite potential barrier at the boundaries. It is known that for a free electron, delocalized waves follow a quadratic relationship between wave vector *k* and energy *E*:

$$E = \frac{\hbar^2 k^2}{2m_e} \qquad \textbf{Eq.(I.2)}$$

where *E* is the electron energy, *k* its wave vector and m_e its effective mass. In the effective mass approximation, the above relationship is assumed to hold for an electron or a hole in the periodic potential well of crystalline semiconductor, implying that the energy band is parabolic near the band gap. In strong confinement regime, the size-dependent band gap energy shift in a nanocrystal of radius *R* with respect to bulk counterpart can thus be derived as:

$$\Delta Eg = \frac{\hbar^2 \pi^2}{2\mu R^2} - \frac{1.8e^2}{\varepsilon R} = \frac{\hbar^2 \pi^2}{2R^2}\left(\frac{1}{m_e} + \frac{1}{m_h}\right) - \frac{1.8e^2}{\varepsilon R} \qquad \textbf{Eq.(I.3)}$$

where μ is the reduced effective mass of an electron-hole pair $\left(\frac{1}{m_e} + \frac{1}{m_h}\right)$. The first term in Eq.(I.3) contains the well-known $1/R^2$ dependence associated with the particle-in-a-box treatment and shows the energy shift to higher values due to quantum localization. The second term in Eq.(I.3) shows a $1/R$ dependence and is representative of the screened Coulomb interaction energy. The EMA model is not quantitatively accurate, as shown by the deviation from the experimental values, particularly for very small nano-crystals (Figure I.3).

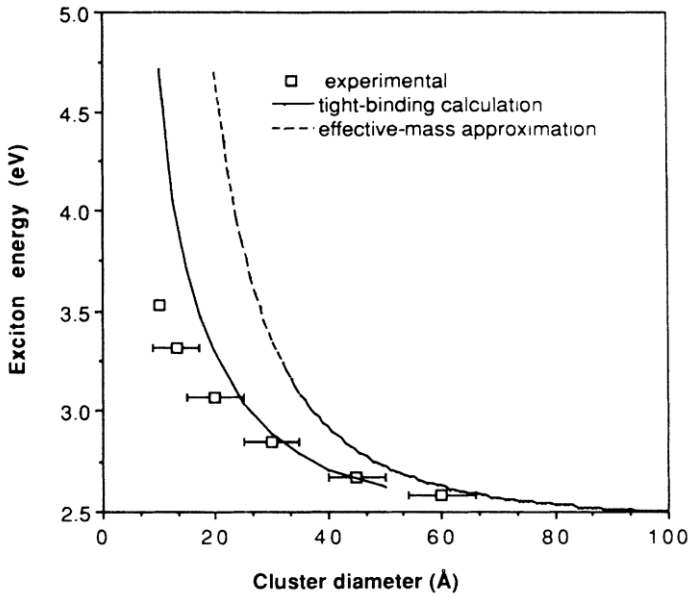

Figure I. 3 *Experimental exciton transition energy of CdS nanoclusters as a function of cluster diameter, along with fits to the data based on the tight-binding model [22] and the effective-mass approximation.*

This breakdown of the EMA model may be caused by two important aspects. First, the energy bands can significantly deviate from the assumed parabolic shape, and typically more as the particle size is reduced [22, 23]. The deviation is especially evident in semiconductor compounds possessing a relatively small band gap. It implies that the effective mass approximation is no longer valid, except in the region where $k = 0$. Secondly, while the structures found in NCs are often quite similar to those observed in the corresponding bulk materials, crystalline differences could significantly change the effective masses of the electrons and holes. Nevertheless, this model is particularly useful, from a practical point of view, in predicting size-dependent energy shifts in a large number of nanocrystalline semiconductors.

Another approach, which has been used to understand and explain quantum confinement effects quantitatively, is the tight-binding approximation model. This approach can be understood as the opposite extreme of the nearly free electron model since it regards the solid as an assembly of weakly interacting neutral atoms [24]. It basically considers the overlap of atomic orbitals in a bonded system as the source for corrections of the isolated atom picture [24]. It provides a real space picture of the electronic interactions and is extremely useful in the study of changes in band structure, density of states, and related functions due to variations in the electronic configuration. This is well displayed in a three dimensional tight-binding energy equation [25]:

$$E(k) = E_0^{'} + 4\gamma\left[\sin^2\left(\frac{k_x a}{2}\right) + \sin^2\left(\frac{k_y a}{2}\right) + \sin^2\left(\frac{k_z a}{2}\right)\right] \qquad \textbf{Eq.(I.4)}$$

with *E(k)* the band energy as a function of the wave vector coordinates, $E_0^{'}$ the energy at the bottom of the band and 4γ the bandwidth. Also Figure I.3 illustrates the comparison between the experimental and theoretical band gap as a function of CdS nanocrystal size [25]. From Figure I.3, it can be seen that the model is also not accurate enough in the smallest size regime, as it was the case of EMA. However, it shows a good agreement with the experimental values for the CdS nanoparticles with cluster diameters greater than 3 nm.

Both the "electron-hole in a box" model with EMA and the molecular orbital approach (tight-binding model) can not explain the observed size dependence of narrow band gap semiconductors in the strong confinement regime, especially for PbS nanoparticles. For this reason, Wang et *al.* [21] have developed two theoretical models, both including the effect of the band non-parabolicity: the hyperbolic band model and the cluster model.

The hyperbolic band model is an extension of the EMA model, considering the full dispersion curves of the electron and hole bands. Those bands are hyperbolic but they approach parabolic behaviours near the *L* point of the Brillouin zone [21]. The derived band gap is as follows:

$$\Delta E = \left(E_g^2 + \frac{2\pi^2\hbar^2 E_g}{m^* R^2}\right)^{1/2} \qquad \textbf{Eq.(I.5)}$$

where E_g is the bulk band gap energy, *R* the quantum dot radius and *m** the effective mass of both electron and hole.

Figure I.4 shows that equation (I.5) with E_g = 0.41 eV and m^*/m_e = 0.085 adequately describes the observed band gap of PbS for all but the smallest particles (D < 2 nm). For comparison, it can be seen that the effective mass approximation starts to break down for PbS particles smaller than about 10 nm.

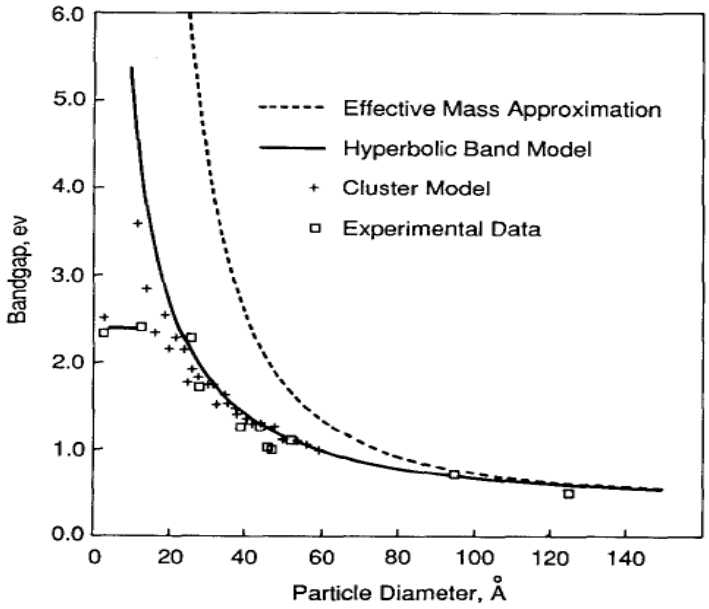

Figure I. 4 *Band gap of PbS as a function of particle size with different theoretical model.*

The "cluster" model has been developed to treat more accurately smaller clusters. It proceeds from the bulk two-band model (hyperbolic band) translated into a local tight-binding hamiltonian. The Hamiltonian has been solved for an increasing number of atoms in a basis set of *ab initio* pseudo-functions consisting of sp^3 orbitals centered on the Pb and S atoms. In the monomolecular limit, the cluster model gives the PbS gap of 2.5 eV, which compares closely with the first allowed excited state of PbS in gas phase, 2.33 eV. Figure I.4 also shows the calculated band gap for cluster chosen in the form of crystals bounded by spheres centered in the center of a cubic PbS building block. For particle sizes larger than 4 nm, the cluster model gives the same result as that of hyperbolic band model. Below that size, the cluster model gives lower values of ΔE than Eq.(I.5), in accordance with experimental measurements. Hence, the cluster model has been used in this thesis in order to estimate the diameter sizes of PbS nanoparticles embedded inside silica xerogel matrices.

I.1.5. Optical properties of quantum dots

I.1.5.1. Linear optical properties of QDs

The optical properties of semiconductor NCs are determined by factors such as size, shape, surface and bulk defects, impurities, and crystallinity. The dependence on the Q-dot size, the parameter that exerts the greatest influence, arises from changes in the surface-to-volume ratio and quantum confinement, which modifies the density of states near the band edges. Size-dependent optical properties of semiconductor nanoparticles, synthesized by different methods

and embedded in different matrices, have been widely studied. Optical properties of quantum dots have been observed since the beginning of the last century, for instance in CdS colloids [26]. As we have discussed in the previous section, the most striking effect in semiconductor nanoparticles is the widening of the gap E_g between the highest occupied electronic states (the top of the original valence band) and the lowest unoccupied states (the bottom of the original conduction band) [27]. This directly affects the optical properties of quantum dots as compared to the corresponding bulk material. Light with energy lower than E_g cannot be absorbed by the quantum dot. Since the band gap depends on the size of a quantum dot, the onset of absorption is also size-dependent [28, 29]. In Figure I.5, it can be seen that smaller quantum dots have an absorption spectrum that is shifted to shorter wavelengths with respect to larger quantum dots and to the bulk material.

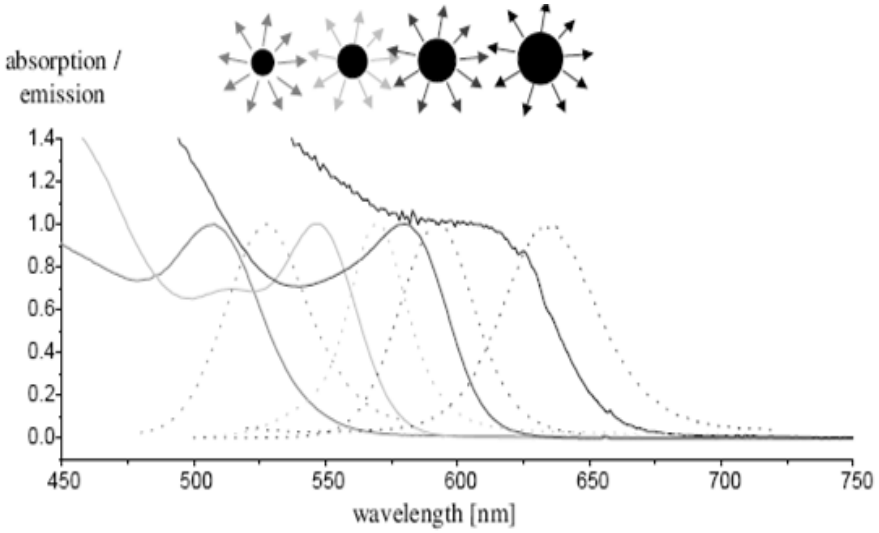

Figure I. 5 *Absorption (plain lines) and emission spectra (dotted lines) of colloidal CdSe quantum dots of different sizes.*

Excitons in semiconductors have a finite lifetime because of the recombination of the photo-excited electron-hole pair. In quantum dots, the energy released upon exciton annihilation is too large to be dissipated only by vibrational modes. Instead, it is released in the form of emitted photons. Radiative decay through emission of photons, in other words fluorescence, is a highly probable decay channel in quantum dots [30]. As is the case of organic fluorophores, the range of energies emitted from a colloidal dot sample after excitation is centered at a value smaller than the one required to excite the sample. In other words, the wavelength of the fluorescence is longer than that of the absorbed light. The shift between the lowest energy peak in the absorption spectrum of a quantum dot and the corresponding emission peak is called the ‘‘Stokes shift’’ (Figure I.5) [31]. The position of the luminescence peak is also dependent on the

average quantum dot size, and its width is correlated to the nanocrystals size distribution. Consequently, the maximum of the emission spectrum and its width can be used to estimate the mean size and the size distribution during nanocrystal growth, under the assumption of spherical shapes.

I.1.5.2. Parameters that affect the optical properties of semiconductor nanocrystals

Other important parameters, determining the nanocrystal absorption or emission, are surface defects and shape effects. For example, due to an increasing surface-to-volume ratio with decreasing the particle size, the surface trap states exert an enhanced influence over photoluminescence properties, including emission efficiency, spectral shape, position, and emission dynamics. Further, it is often through their surfaces that semiconductor nanocrystals interact with ‘‘their world,’’ as soluble species in an organic solution, glasses, biological media and so forth. Controlling inorganic and organic surface chemistry [32, 33] is the key to control the physical and chemical properties that make NCs QDs unique compared to their epitaxial QD counterparts. Moreover, nanoparticles could be formed with different shapes and this parameter can sometimes be controlled. The most successful nano-QD preparations in terms of quality and monodispersity entail pyrolysis of metal–organic precursors at (120–350°C) [34]. In most synthesis techniques, size and size dispersion can be controlled during the reaction. In general, time is a key variable: longer reaction times yield a larger average particle size. Nucleation and growth temperatures play contrasting roles. Lower nucleation temperatures support lower monomer concentrations and can yield smaller-size nuclei, whereas higher growth temperatures can generate larger particles as the rate of monomer addition to existing particles is enhanced. Precursor concentrations can influence both the nucleation and the growth processes. Its effect is dependent on the surfactant/precursor concentration ratio and on the nature of the surfactants. All else being equal, higher precursor concentrations promote the formation of fewer, larger nuclei and, thus, larger QD particle size. Recently, the use of light from a lamp or a laser beam to form semiconductor nanoparticles became a promising method: this different kind of treatment may influence the growth process of the nanoparticles and consequently their optical properties.

I.1.5.3. Non-Linear optical properties of QDs

Semiconductor nanocrystals in solutions or in glasses have been shown to be very promising media for all-optical devices, as they exhibit useful third-order nonlinearities. The nonlinear

exaltation is usually ascribed to strong absorption cross-sections due to the intrinsic nature of semiconductors and also because of quantum confinement effects. Moreover, the tunability of these nonlinearities comes from the absorption threshold adjustment with QD size. Under sufficiently high light power density, induced or saturated excitation may be possible due to the abundance of incoming photons, leading to nonlinear absorption. The absorption of the material α is then intensity-dependent: $\alpha = \alpha_0 + \beta I$ where β is the nonlinear absorption coefficient, α_0 the linear absorption coefficient. When an amorphous material is placed in such a strong electromagnetic field, a change in the refractive index also occurs: $n = n_0 + n_2 I$ where n_2 is the Kerr nonlinear refractive index and n_0 the linear refractive index. There have been many experiments to study the nonlinear optical properties of semiconductor nanocrystals [35-39]. Different techniques have been used to characterize their nonlinearities such as Third Harmonic Generation (THG), Degenerate Four Wave Mixing (DFWM) and Z-scan. But only a few reports [40, 41] concern the study of the dispersion of semiconductor nanocrystal nonlinearities. Theoretical works on the subject are also rather scarce. Assuming the light is a polarized plane wave, Cotter et al. [40] calculated the dispersion of third optical nonlinearity $\chi^{(3)}$ through a theoretical approach based on the sum-over-states formula and using a two-band effective-mass model in infinitely deep spherical quantum wells. Their calculation yielded the following expression:

$$\chi^{(3)} = \frac{2N\hbar(e/m)^4}{3V\varepsilon_0(\hbar\omega)^4} \sum_{vabc} p_{va}\, p_{ab}\, p_{bc}\, p_{cv} \left[\frac{1}{(\Omega_{av}-\omega)(\Omega_{bv}-\omega)(\Omega_{cv}-\omega)} + (\text{five similar terms}) \right] \qquad \textbf{Eq.(I.6)}$$

Here p is the momentum matrix element, N is the number of microcrystallines in volume V, ε_0 is the free space permittivity, $\hbar\omega$ is the photon energy, e and m are the electronic charge and rest mass, respectively. Figure I.6 shows their plot of $\chi^{(3)}$ versus the normalized photon energy $\hbar\omega/E_g$. The calculated dispersion of $\chi^{(3)}$ for different semiconductor nanocrystals (Cd(S, Se, Te) was taken using Z-scan technique. They have shown that the Im $\chi^{(3)}$ is positive for $\hbar\omega/Eg < 1$ and the $Re\ \chi^{(3)}$ is always negative and generally increases in magnitude with increasing $\hbar\omega$, i.e. when approaching absorption threshold.

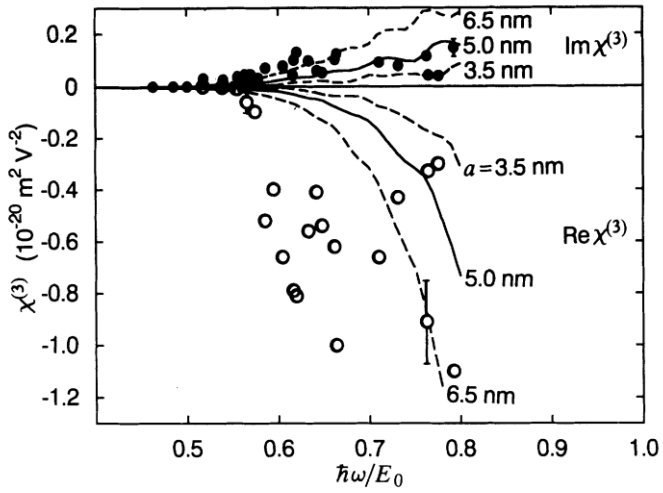

Figure I. 6 *Dispersion of the real (open circles) and imaginary (closed circles) components of third-order susceptibility for spherical nanocrystals after Cotter [40].*

Studying the nonlinear optical properties of CdS and CdTe semiconductors, Banfi et *al* [41] have checked the effect of confinement by comparing the values of the two-photon absorption susceptibility $\mathrm{Im}\chi^{(3)}$ obtained with nanocrystals of the same chemical composition, but with different sizes, to that of the bulk. Figure I.7 presents a plot of $\mathrm{Im}\chi^{(3)}$ as function of the crystallite radius for both semiconductors. Surprisingly, the data show no significant size dependence of $\mathrm{Im}\chi^{(3)}$.

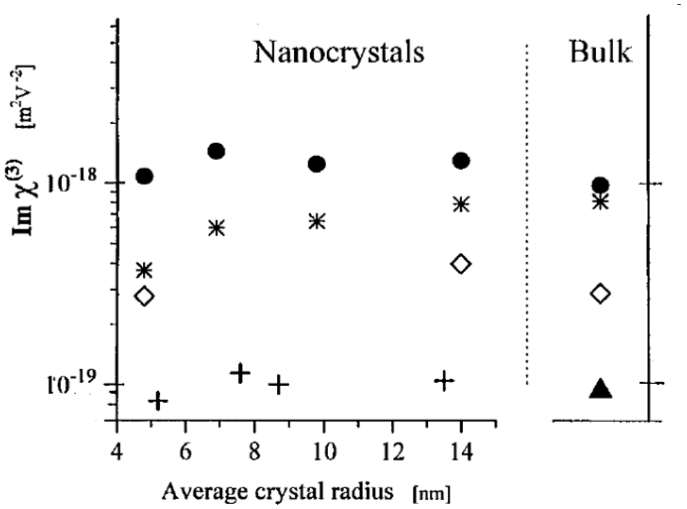

Figure I. 7 *$\mathrm{Im}\chi^{(3)}$ against the nanocrystal radius. At the right hand end, the $\mathrm{Im}\chi^{(3)}$values of bulk are shown. For CdTe nanocrystals and CdTe bulk at 1.2µm (●), 1.4µm (*) and 1.58 µm (◊), and for CdS nanocrystal (+) and bulk CdS (▲) at 0.79µm [41].*

The obtained values are also quite close to those of the bulk samples. Furthermore, one should note a small decrease in $\mathrm{Im}\chi^{(3)}$ when the radius tends to a few nanometers because of the

quantum confinement effect. As already seen above, Im $\chi^{(3)}$ depends on the bang gap, which is slightly enlarged as the radius is decreased. Even if nonlinear absorption effects in bulk semiconductors are as strong as in their nanosized counterparts, the nanoparticle form allows to tune the band-gap and to locally dope optical glasses.

I.2. Metallic nanoparticles

Metal particles are particularly interesting nano-scale systems because of the ease with which they can be synthesized and chemically modified. From the standpoint of understanding their optical and electronic effects, metal nanoparticles also offer an advantage over other systems because their optical (or dielectric) constants resemble those of the bulk metal to exceedingly small dimensions. Perhaps the most intriguing observation is that noble metal particles often exhibit strong plasmon resonance extinction bands in the visible spectrum [42], the position of which depends on the nature of the metal (Ag, Au, Cu), resulting in deep colours reminiscent of molecular dyes. For instance, the intense colour of colloidal noble metal particles in stained glass windows [43] and Lycurgus cup [44], as illustrated in Figure I.8, is caused by the surface plasmon resonance.

Figure I. 8 *Left: a picture of the Rose Window of the Notre Dame Cathedral in Paris. The bright red and purple colors are due to gold nanoparticles. Right: Lycurgus cup. It appears green in reflected light, but appears red when light is shone from inside and is transmitted through the glass.*

The surface plasmon resonance can be thought of as the coherent motion of the conduction-band electrons caused by interaction with an electromagnetic field [45-47]. In a classical description, the electric field of an incoming light wave induces a polarization of the electrons with respect to the much heavier ionic core of a spherical nanoparticle. A net charge difference is only felt at the nanoparticle surface, which in turn acts as a restoring force. This creates, in the simplest

case, a dipolar oscillation of all the electrons with the same phase. When the frequency of the electromagnetic field becomes resonant with the coherent electron motion, a strong absorption in the spectrum is seen, which is at the origin of the observed color.

The frequency and width of the surface plasmon absorption depend on the size and shape of the metal nanoparticles, as well as on the dielectric constant of the metal itself and of the medium surrounding it [45, 48]. The plasmon resonance is strong and placed into the visible part of the electromagnetic spectrum for the noble metals, which is the reason why the noble metals have historically fascinated scientists at the time of Faraday [49].

I.2.1. Linear Optical properties of Metallic nanoparticles

First studies of the optical properties of metal particles date back to Faraday in 1857 [49] who associated the brilliant colours exhibited by very thin gold films to their discontinuous nature. The extraordinary spectral response arises from the excitation of plasmon polaritons (resonant coupling of the incident field with quanta of collective conduction electron plasma oscillations) with resonant energies across the UV-visible spectrum. The excitation of surface plasmons on metal nanoparticles can be qualitatively understood by considering the particles as a simple oscillator. An external electric field is able to displace the free electrons in metal nanoparticles with respect to the fixed ionic core. This displacement sets up a restoring force, leading to coherent, resonant oscillations of charge density (Figure I.9).

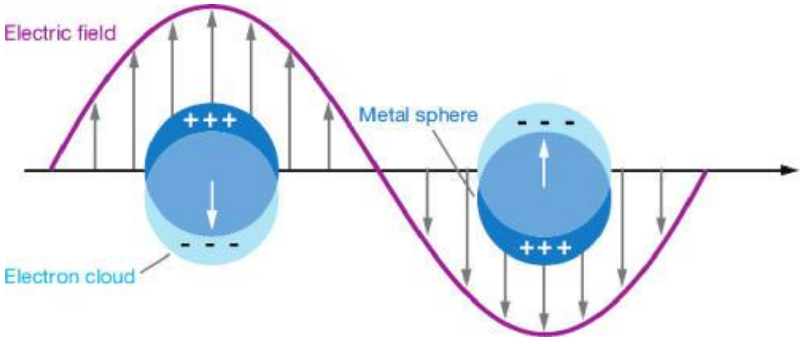

Figure I. 9 *Representation of the interaction of an oscillating electric field with the electron clouds of metal nanoparticles [50].*

Once excited, localized surface plasmons (LSP) decay either radiatively or non-radiatively. Radiative decay results in re-emission of photons, i.e. scattering. Non-radiative decay processes are due to energetic relaxation, resulting in absorption of incident photons and heating of the nanoparticle. Relaxation primarily occurs through creation of electron-hole pairs, either through intraband or interband transitions [51].

Excitation of the LSP gives rise to intense scattering and/or absorption of light, which in turn results in a decrease in optical transmission (Figure I.10). This decrease is known as extinction, which is the sum of absorption and scattering. The strength of scattering and absorption of light by a particle varies strongly with wavelength. In the case of the metal particles, these effects are primarily due to excitation and relaxation of LSP.

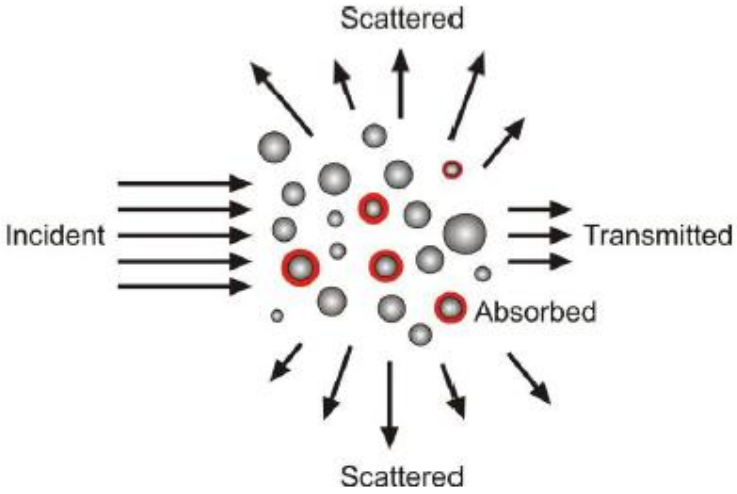

Figure I. 10 *Representation of scattering and absorption of lights by an ensemble of particles [52].*

The extinction peak correlates with the LSP peak, which is a strong function of the particle geometry, composition, and of the surrounding dielectric environment. Essentially, altering these properties changes the resonant condition of oscillation, and hence the magnitude and spectral position of the LSP. Excitation of the LSPs also results in strong confinement of incident photons, corresponding to enhancements of the local field intensity, which are particularly related to particle shape.

The interaction of light with metal nanoparticles is a complex process, highly sensitive to a number of geometric and material considerations. To maximize the usefulness of metal nanoparticles, analytical or numerical models are required to predict their optical properties taking into account parameters that affect the magnitude and the position of the SPR, such as shape and surrounding medium.

I.2.2. Theories of optical response for spherical metallic nanoparticles

The linear optical properties like extinction and scattering of small spherical metal particles accounting for the surface plasmon resonance were explained theoretically by the

groundbreaking work of Mie in 1908 [53]. Mie solved Maxwell's equation for an electromagnetic light wave interacting with a small sphere having the same macroscopic, frequency-dependent dielectric constant as the bulk metal. With the appropriate boundary conditions for a spherical object, his electrodynamic calculations gave a series of multipole oscillations (dipole, quadrupole, etc.) for the extinction and scattering cross section of the particles as a function of the particle radius. The sphere and matrix materials are described via their dielectric constants, $\varepsilon = \varepsilon_1 + i\varepsilon_2$ and ε_m, respectively. If the sphere is much smaller than the optical wavelength λ, keeping the lowest order terms in R/λ (dipolar approximation), the expressions of the absorption and scattering cross-sections reduce to [45, 54]:

$$\sigma_a(s) = \frac{18\pi V \varepsilon_m^{3/2}}{\lambda} \frac{\varepsilon_2}{\left|\varepsilon + 2\varepsilon_m\right|^2} \qquad \textbf{Eq.(I.7)}$$

$$\sigma_s(s) = \frac{24\pi^3 V^2 \varepsilon_m^2}{\lambda^4} \left|\frac{\varepsilon - \varepsilon_m}{\varepsilon + 2\varepsilon_m}\right|^2 \qquad \textbf{Eq.(I.8)}$$

with V the particle volume. The same results are obtained in the quasi-static approximation [54]. In this small size approximation, the extinction and absorption cross-sections are identical, and much larger than the scattering cross section. As it is well known, confinement of the electromagnetic field leads to resonant enhancement of the nanosphere absorption (and scattering) close to the wavelength λ_R. This wavelength is obtained by minimizing the denominator $|\varepsilon + 2\varepsilon_m|$, which is the condition for the surface Plasmon resonance (SPR). The SPR wavelength λ_R is determined by the particle properties, through ε, and by its local environment, through ε_m. For a small value of ε_2 or if it is weakly dispersed in the SPR spectral region, λ_R is determined by the simple condition [45]:

$$\varepsilon_1(\lambda_R) + 2\varepsilon_m = 0 \qquad \textbf{Eq.(I.9)}$$

A second, less important, phenomenon in metal NCs is due to quantum confinement. The dielectric function, ε, describing the metal response, is modified by electron confinement in reduced dimensionality systems. In a metal, ε can be separated into a bound and quasi-free electron contribution:

$$\varepsilon(\omega) = \varepsilon_b - \frac{\omega_p^2}{\omega(\omega - i\gamma)} \qquad \textbf{Eq.(I.10)}$$

with ω_p the bulk Plasmon frequency ($\omega_p^2 = \frac{n_e e^2}{\varepsilon_0 m}$), ω the photon frequency, ε_b the background polarization of metal cores, n_e and m the conduction electron density and effective mass, respectively and γ the conduction band electron scattering rate. The response of quasi-free electrons is modified in a nanocrystal due to their interaction with the interface and the concomitant breakdown of the system periodicity. However, for metal particles larger than a few nanometres, this effect is weak and can be introduced as a correction using [45, 55].

$$\gamma(\omega) = \gamma'(\omega) + 2gV_F / D \qquad \textbf{Eq.(I.11)}$$

The first term, γ' takes into account bulk-like electron scattering altered by confinement in the particle [56-58]. The second term is proportional to the Fermi velocity V_F with a proportionality factor g of the order of 1 [45]. Actually, to first order, the electron–electron and electron–phonon scattering rates [57, 58] exhibit a *1/D* dependence. γ' is thus also expected to vary as *1/D*, a dependence that can be lumped into the second surface effect term.

The optical response of an ensemble of metallic nanoparticles is given by the Maxwell Garnett (MG) theory [59].The Maxwell-Garnett model is based on the dipole approximation of the metal nanoparticles and takes into account their electrostatic interaction in the dielectric medium via the Clausius–Mossotti equation. In that sense, it is a special case of the effective medium approximation (EMA) [60]. The dielectric function in the Maxwell-Garnett (MG) model is given by:

$$\varepsilon_{EMA} = n_m^2 \frac{\varepsilon(1+2f) + 2n_m^2(1-f)}{\varepsilon(1-f) + n_m^2(2+f)} \qquad \textbf{Eq.(I.12)}$$

with *f* the filling fraction of metal nanoparticles inside the non-absorbing medium of refractive index n_m, and ε the dielectric function of the metal nanoparticles. In the limit of weak concentrations, the MG approach gives the same absorption cross-section as obtained with the Mie theory [53], expressed by Eq.(I.7) for very small sizes.

A much simpler formulation has been given by several authors in the framework of the free-electron theory. Both Doyle [61] and Kreibig [62] have shown that the bulk optical properties of the metal must be modified when the electron mean free path is less than the particle radius. In

this approach, the dc conductivity σ_{dc} and the bandwidth at half-maximum of the SPR absorption peak, $\Delta\omega_{1/2}$, are related through the following equation:

$$\sigma_{dc} = \frac{N_0 e^2}{m\,\Delta\omega_{1/2}} \qquad \textbf{Eq.(I.13)}$$

with N_0 the free-electron concentration (bulk Au atomic density), m and e the electron mass and charge, respectively. In the free-electron theory, however, it can also be written:

$$\sigma_{dc} = \frac{N_0 e^2 \tau}{m} \qquad \textbf{Eq.(I.14)}$$

$$\tau = \frac{l}{V_F} \qquad \textbf{Eq.(I.15)}$$

with τ the elastic scattering time, l the mean free path, and V_F the Fermi velocity. For particles having radii less than the mean free path, the particle diameter d, can be substituted for l and one finally obtain

$$d = \frac{V_F}{\Delta\omega_{1/2}} \qquad \textbf{Eq.(I.16)}$$

This simple equation has been used a lot [63-67] to calculate the nanoparticle size inside glass dielectric matrices. The Fermi velocities of the noble metals (Ag, Cu and Au) and their SPR position in Vacuum medium are presented in Table I.1 [68, 69].

Nobel metal	Fermi velocity (10^8 cm.s^{-1})	Vacuum SPR position (nm)
Au	**1.39**	**520**
Cu	**1.57**	**565**
Ag	**1.39**	**355**

Table I. 1 *The Fermi velocity values of noble metals calculated using the free electron gas model and the SPR maximum wavelength as calculated using the Mie theory.*

I.2.3. Parameters that affect the optical response of metallic nanoparticles

As in semiconductors, the main parameters that affect the optical response of metallic nanoparticles are shape, size and surrounding medium, all depending on the preparation

conditions such as concentration of precursors, heating temperature, laser irradiation, ,etc… Influences of these parameters have been widely studied [42, 70-73].

For small enough particles, ε_m begins to diverge from its bulk (or thin film) value, resulting in a particle size dependence of the energy and width of the SPR: this called the finite size effect. This divergence is anticipated since the dielectric function is a solid state macroscopic parameter in the metal, whereas small metal particles can be regarded as a transition state, the properties of which must eventually converge with the atomic response as the number of atoms in the particle decreases to one. Experimentally, the effect of the finite size of the particles on ε_m may result in a shift and a broadening of the SPR, following a *1/R* dependence. Figure I.11 illustrates the calculated size effect of small gold particles on their optical absorption response [70]. When the radius *R* increases beyond 10 nm, the absorption peak broadens and shifts to longer wavelengths. On the contrary the SPR undergoes a narrowing with increasing the particle diameter for all particles with radii between 2.6 and 10 nm, without any change in the peak position near 520 nm. On the other hand, the particle shape is found to be very important in the case of noble metal particles. The absorption spectra from non spherical gold particles are shown in Figure I.12. They exhibit two SPR positions which could be referred to several typical lengths in the particles.

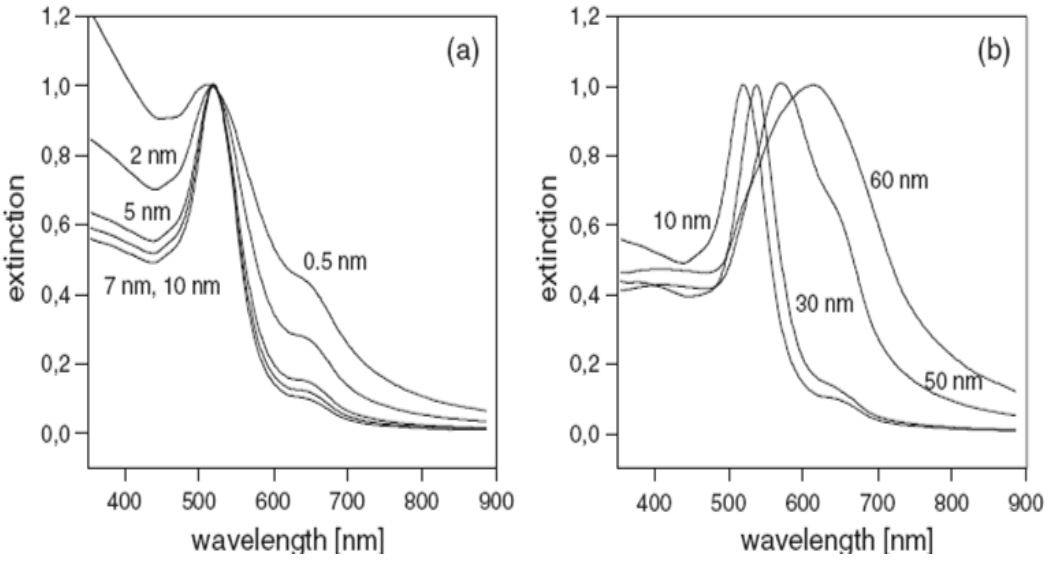

Figure I. 11 *Optical absorption spectra for small gold particles; (a) R <10 nm and (b) R > 10 nm [70].*

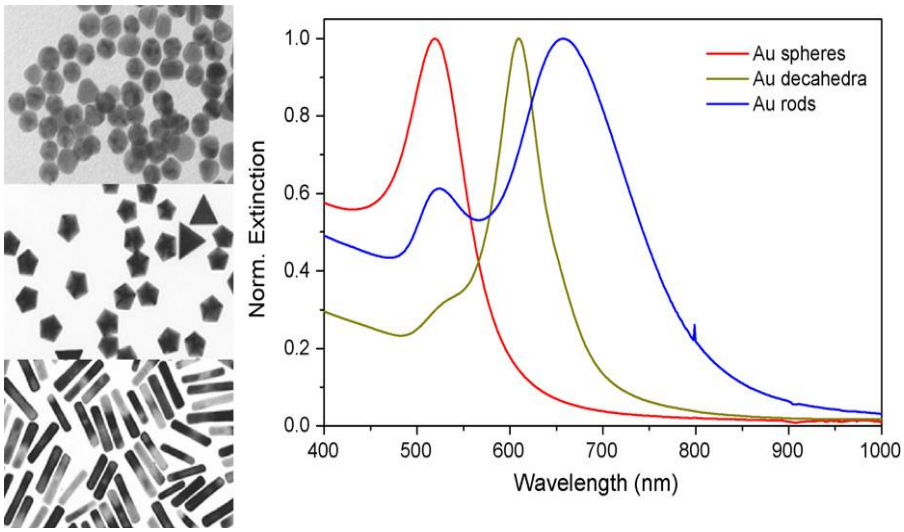

Figure I. 12 *Transmission electron micrographs and UV—Vis spectra of gold nanoparticle colloids with various geometries, as indicated in [71].*

The important influence of the matrix refractive index is illustrated in Figure I.13. As the local index is increased, the SPR peak generally undergoes a very regular and reproducible red-shift. However, the amount of this red-shift also depends on the shape of the nanoparticles.

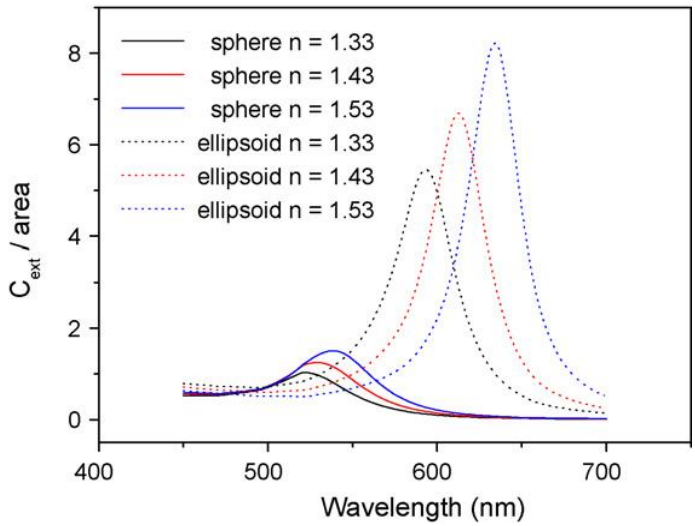

Figure I. 13 *Comparison of the red-shift of the SPR peak in the extinction cross-section of gold nanospheres and ellipsoids when the refractive index of the surrounding dielectric changes [71].*

Hence, by adjusting the metal nature and the nanoparticles morphology, as well as the refractive index of the dielectric medium around them, it is possible to tune the optical properties of metal-doped systems within the whole visible spectral range.

I.2.4. Non-Linear Optical properties of metallic nanoparticles

Optical nonlinearities of metallic nanoparticles were the subject of numbers of investigations during the past decade due to their wide interest in optical devices. The first study on this subject has been done by Hache et *al*. [55]. They proposed the only model in the literature to calculate the nonlinear susceptibility, based on the addition of different contributions: intraband electron transitions, interband electron transition and hot electrons generated by the laser impulsion.

$$\chi_m^{(3)} = \chi_{\text{int}\,ra}^{(3)} + \chi_{\text{int}\,er}^{(3)} + \chi_{he}^{(3)}$$

The contribution of intraband transitions is purely imaginary, negative and inversely proportional to cubic power of particle size (R < 15nm) near the SPR of the metallic nanoparticles [55]. This behaviour has been more or less experimentally observed in Cu nanoparticles, as shown in Figure I.14 [76]. The contribution of interband also gives a negative value, independent on the particle size except for those less than of 2.5 nm [74]. Addition of the most important hot electrons contribution makes the $\chi_m^{(3)}$ purely imaginary, positive and independent on the nanoparticle size [75]. Unfortunately, these calculations do not predict any resonant character of the nonlinear behaviour.

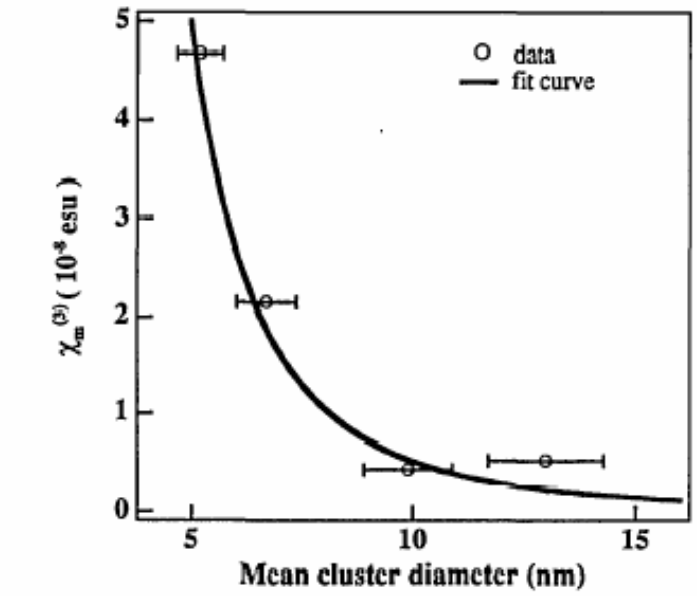

Figure I. 14 *Third-order susceptibility of the Cu clusters as a function of mean particle diameter. The solid line is the fit of l/R^3 [76].*

Conclusion

This bibliography shows the interest of these metallic and semiconductor nanoparticles in the domains of optics. The present work aims to fabricate and to study high concentrations of such nanoparticles, locally in transparent matrices or even in optical fibres for new applications based, for example, on nonlinear properties. To this purpose, post-doping techniques associated with laser-induced precipitation have been used to dope sol-gel-derived dielectric matrices with CdS, PbS, Au, Ag and Cu nanoparticles. In the next chapter, we present the sol-gel synthesis method, the doping methods and the characterization techniques used in this thesis.

References

1. AL.L. Efros, AL. Efros. Sov. Phy. Semiconduct+. **16,** 772 (1982).
2. V.I. Klimov. Semiconductor and Metal Nanocrystals: Synthesis and Electronic and Optical Properties. Marcel Dekker, New York: 2004.
3. D. Roy, J. Fendler. Adv. Mater. **16,** 479 (2004).
4. Y. Sun, Y. Xia. Analyst. **128,** 686 (2003).
5. H. Xu, M. kall. Sens. Actuators.B. **87,** 244 (2002).
6. G. Hodes, A. Albu-Yaron, F. Decker and P. Motisuke. Phy.Rev. B. **36,** 4215 (1987).
7. L.Z. Yao, C.H. Ye, C.M. Mo, W.L. Cai, L.D. Zhang, J. Crystal. Growth. **216,** 149 (2000).
8. P. Guyot-Sionnest. Infrared and visible electrochromic semiconductor colloid quantum dots. Nanoscale Materials. Springer, Berlin: 2003.
9. W.U. Huynh, J.J. Dittmer, A.P. Alivisatos. Science. **295,** 2425 (2002).
10. I. Gur, N.A. Fromer, M.L. Geier, A.P. Alivisatos. Science. **310,** 462 (2005).
11. B. Sun, N.C. Greenham. Phys. Chem. Chem. Phys. **8,** 3557 (2006).
12. A.N. Rogach, N. Gaponik, J.M. Lupton. Angew. Chem. Int. Edit. **47,** 6538 (2008).
13. A.L. Rogach, A. Eychmuller, S.G. Hickey, S.V. Kershaw. Small **3,** 536 (2007).
14. M.T. Harrison, S.V. Kershaw, M.G. Burt. Pure. App. Chem. **72,** 295 (2000).
15. G. Konstantatos, I. Howard, A. Fischer. Nature **442,** 180 (2006).
16. N. Cho, K. Roy Choudhury, R.B. Thapa. Adv. Mater. **19,** 232 (2007).
17. M.P. Bruchez, M. Morrone, P. Gin, S. Weiss, A.P. Alivisatos. Science **281,** 2013 (1998).
18. B. Zhang, G. Li, J. Zhang, Y. Zhang, L. Zhang. Nanotechnology **14,** 443 (2003).
19. M.J. Fernee, A. Watt, J. Warner, N. Heckenberg, H. Rubinsztein-Dunlop. Nanotechnology **15,** 1328 (2004).
20. L.E. Brus. J. Chem. Phys. **79,** 5566 (1983).
21. Y. Wang, A. Suna, W. Mahler, R. Kasowski. J. Chem. Phys. **87,** 7315 (1987).
22. P.E. Lippens, M. Lanno. Phys. Rev. B **39,** 10935 (1989).
23. Y. Wang, N. Herron. Phys. Rev. B **42,** 7253 (1990).
24. S. Glutsch. Excitons in Low-Dimensional Semiconductors. Springer, Berlin: 2004.
25. E.O. Kane. J. Phys. Chem. Solids **1,** 249 (1957).
26. G.Z. Jaeckel. Tech. Phys. **6,** 301 (1926).
27. S.V. Gaponenko. Optical Properties of Semiconductor Nanocrystals. Cambridge University Press, Cambridge: 1998.
28. M.G. Bawendi. M.L. Steigerwald. L.E. Brus. Annu. Rev. Phys. Chem. **41,** 477 (1990).

29. C.B. Murray, D.J. Norris, M.G. Bawendi. J. Am. Chem. Soc. **115,** 8706 (1993).
30. V.I. Klimov, D.W. McBranch, C.A. Leatherdale, M.G. Bawendi. Phys. Rev. B **60,** 13740 (1999).
31. G. Schmid. Nanoparticles: From Theory to Application. WILEY-VCH, Weinheim: 2004.
32. R.A.Sperling, W.J. Parak. Phil. Trans. R. Soc. A. **368,** 1333 (2010).
33. B. Gilbert, F. Huang, Z. Lin, C. Goodell, H. Zhang, J.F. Banfield. Nano Lett. **6,** 605 (2006).
34. N.N. Parvathy, A.V. Rao, G.M. Pajonk. J. Non-Cryst. Solids **241,** 79 (1998).
35. S.H. Park, M.P. Casey, J. Falk. J. Appl. Phys. **73,** 8041 (1993).
36. S.G. Lu, Y.J. Yu, C.L. Mak, K.H. Wong, L.Y. Zhang, X. Yao. Microelectro. Eng. **66,** 171 (2003).
37. F. Yoshino, A.A. Major, L. Levina, E.H. Sargent. OSA 2004, paper IWA23.
38. H.M. Gong, X.H. Wang, Y.M. Du. J. Chem. Phys. **125,** 024707 (2006).
39. D.J. Asunskis, I.L. Bolotin, L. Hanley. J. Phys. Chem. C **112,** 9555 (2008).
40. D. Cotter, M.G. Burt, R.J. Manning Phys. Rev. Lett. **68,** 1200 (1992).
41. G.P. Banfi, V. Degiorgio, D. Ricard. Adv. Phys. **47,** 447 (1998).
42. L.M. Liz-Marzan. Langmuir **22,** 32 (2006).
43. S. Link, M.A. El-Sayed. Annu. Rev. Phys. Chem. **54,** 331 (2003).
44. I. Fresstone, N. Meeks, M. Sax, C. Higgitt. Gold Bull. **40,** 270 (2007).
45. U. Kreibig, M. Vollmer. Optical Properties of Metal Clusters. Springer, Berlin: 1995.
46. M. Kerker. The Scattering of Light and Other Electromagnetic Radiation. Academic, New York: 1969.
47. C.F. Bohren, D.R. Huffman. Absorption and Scattering of Light by Small Particles. Wiley, New York: 1983.
48. G.C. Papavassiliou. Prog. Solid State Chem. **12,** 185 (1979).
49. M. Faraday Philos. Trans. **147,** 145 (1857).
50. K.L. Kelly, E. Coronado, L.L. Zhao, G.C. Schatz. J. Phy. Chem. B. **107,** 668 (2003).
51. M.L. Brongersma. Surface Plasmon Nanophotonics. Springer, Florida: 2007.
52. C.F. Bohren, D.R. Huffman Absorption and scattering of light by small particle. Willey, 2004.
53. G. Mie. Ann. Phys. **25,** 377 (1908).
54. C.F. Bohren, D.R. Huffman. Absorption and Scattering of Light by Small Particles. Wiley, New York: 1998.
55. F. Hache, D. Ricard, C.H. Flytzanis. J. Opt. Soc. Am. B **3,** 1647 (1986).
56. C. Voisin, N. Del Fatti, D. Christofilos, F. Vallee. J. Phys. Chem. B **105,** 2264 (2001).

57. C. Voisin, N. Del Fatti, D. Christofilos, F. Vallee. Phys. Rev. Lett. **85,** 2200 (2000).
58. A. Arbouet et *al* Phys. Rev. Lett. **90,** 177401 (2003).
59. J.C. Maxwell Garnett, Philos. Trans. R.Soc. Lond. **203**, 1904385.
60. V. Myroshnychenko, J. Rodriguez-Fernandez, I. Pastoriza-Santos, A. M. Funston, C. Novo, P. Mulvaney, L. M. Liz-Marzan, F. J. G. de Abajo, Chem. Soc. Rev. **37,** 1792 (2008).
61. W.T. Doyle, Phys. Rev. **111,** 1067 (1958).
62. U. Kreibig, C.V. Fragstein, Z. Phys. **224,** 307 (1969).
63. E.M. Vogel. J. Am. Ceram. Soc. **72**, 719 (1989).
64. U. Pal, H.A. Bautista, L. Rodriguez-Fernandez, J.C. Cheang-Wong. J. Non- Cryst. Solids. **275,** 65 (2000).
65. J. Sheng, J. Zhang, L. Qiao. J. Non-Cryst. Solids **352,** 2914 (2006).
66. D. Manikandan, S. Mohan, P. Magudapathy, K. Nair. Phys. B **325,** 86 2003).
67. P. Anlian et *al*. Appl. Surf. Sci. **205**, 323 (2003).
68. N. P. Singh, S. C. Gupta, B. R. Sood. Am. J. Phys. **70,** 845 (2002).
69. Mieplot Software version 4.2
70. L.B. Scaffardi, N. Pellegri, O. de Sanctis, J.O. Tocho1. Nanotechnology **16,** 158 (2005).
71. B. Sepúlveda, P.C. Angelomé L.M. Lechuga, L. M. Liz-Marzán. Nano Today **4,** 244 (2009).
72. G. De, S. K. Medda, S. De, S. Pal. Bull. Mater. Sci. **31**, 479 (2008).
73. C. Cao, S. Park, S.J. Sim. J. Coll. Inter. Sci. **322**, 152 (2008).
74. J. Venturini. Etude des propriétés optiques non-linéaires de matériaux nouveaux. Univeristé Paris VI, 1999.
75. F. Hache, D. Ricard, C. Flytzians, U. Kreibig. Appl. Phys. A **47,** 347 (1988).
76. L.Yang, K. Becker, F.M. Smith, R.H. Magruder, R.F. Haglund, L. Yang, R. Dorsinville, R.R. Alfan, R.A. Zuh. J. Opt. Soc. Am. B **11,** 457 (1994).

Chapter II: Nanoparticles-Doped Sol-gel Matrices: Synthesis and Characterisation

The materials we are interested in are mesoporous gels and dense glasses doped with semiconductor or metallic nanoparticles. Recently, the synthesis of the nanoparticles has become a very important research field. Several physical and chemical methods have been developed to yield better control over the particle size, distribution and morphology, with the aim to enhance the performance of the nanomaterials, displaying improved properties. One of the most often used methods for preparing host matrices is the sol-gel process that provides many advantages including low processing temperature, high purity, and molecular level homogeneity. This method also allows controlling the porosity of the synthesized materials [1]. Controlling the chemical parameters during the sol-gel process and adapting the heat-treatment yields materials with precisely tailored properties, such as mechanical strength, transparency, as well as pore size distribution and surface area of the porous network. The sol-gel-derived materials provide matrices for a variety of organic and inorganic compounds. One of the important features of doped sol-gel materials is their ability to preserve chemical and physical properties of the dopants and the possibility to yield glasses in different forms.

In this chapter, attention is mainly focused on the synthesis of porous silica matrices and on their characterisation. In the first section, detailed information on sol-gel process and on the derived materials are provided. Herein, the preparation of porous and dense silica by sol-gel route is discussed. Brief information about the methods that have been used to incorporate nanoparticles inside the dielectric matrices is shown in section 2. Also in this section, we will present a brief review on the fabrication of the semiconducting and metallic nanoparticles inside the dielectric matrices. Section 2 is also devoted to the different setups of laser irradiation that have been used in this thesis to generate nanoparticles inside our doped silica matrices. Section 3 presents first preparation of microstructured optical fibre (MOF) doped with nanoparticles. Firstly, the different methods used in the preparation of silica preforms will be described, distinguishing the importance of sol-gel methods. Then, generalities on MOF and on their method of elaboration will be provided. Also in this section, a state of art of optical fibres doped with semiconducting or metallic nanoparticles will be given. At the end, a general description of the technique used to characterise our samples is tabled in the last section.

II.1. Sol-gel process

The sol-gel method is a low-temperature technique for creating solid glass bulk samples or thin-films. This technique has been widely used in the preparation of transparent oxide glasses since Ebelmen reported the first synthesis of silica from silicon alkoxide in 1844 [2]. Using this method, coatings on glass, ceramic, metal or others solid substrates are easily fabricated. In addition, the relatively gentle synthetic conditions allow for the addition of dopants such as organic dyes or inorganic ions, which convert the resulting glass/dopant combination into an active material and thus may be used in optical or sensing applications. Sol-gel process is based on the hydrolysis and polycondensation reactions of metalorganic compounds such as silicon alkoxides. Commonly used silicon alkoxides include the family of tetra-alkoxysilanes, which have the general form $Si(OR)_4$, where R is an alkyl group, and therefore OR is an alkoxy group.

II.1.1. Sol-gel Steps

Sol-gel process involves several steps, namely: mixing, gelation, ageing, drying and sintering.

- **Mixing**

It is commonly asserted that the more attractive feature of sol-gel processing is the possibility of tailoring unique materials, especially, by polymerization of a metalorganic compound to a polymeric gel. Metal alkoxides, $M(OR)_n$, where M is the metal and R an alkyl radical, fulfills these requirements. The most used alkoxides, chosen in the preparation of silica-based gels, are tetramethoxysilane $Si(OCH_3)_4$ and tetraethoxysilane $Si(OC_2H_5)_4$, known as TMOS and TEOS, respectively. The liquid alkoxide precursor $Si(OR)_4$ reacts with water and undergoes hydrolysis and polycondensation reactions under the following scheme, in presence of a common solvent (normally alcohol):

1- Hydrolysis
   - $Si(OR)_4 + H_2O \rightarrow Si(OH)_x(OR)_{4-x} + xROH$
2- Polycondensation
   - $Si(OH)_x(OR)_{4-x} + Si(OH)(OR)_{4-x} \rightarrow (OR)_3Si–O–Si(OR)_3 + xH_2O$
   - $Si(OH)_x(OR)_{4-x} + Si(OR)_4 \rightarrow (OR)_3Si–O–Si(OR)_3 + xROH$

Both reactions occur simultaneously and are generally incomplete, but the attainable final oxide is anyway accomplished. Hydrolysis and polycondensation can be accelerated or slowed down by employing an appropriate acid or base catalyst.

- **Gelation**

The formation of a gel is usually called gelation. In the course of time, the polycondensation of the hydrolyzed precursors produces colloidal particles that link together to become a network containing both the solid phase and the liquid phase. In this process, the catalyst plays an important role due to the ionic charge of the silica particles, with a direct influence on the polycondensation rate. Thus, at low pH for example, the silica particles bear very little ionic charge and thus can collide and aggregate into chains forming a polymeric gel. On the opposite side, at high pH, where the rate of dissolution is higher, the particles grow in average size and diminish in number as the smaller ones dissolve.

- **Ageing**

After gelation, the solid network immersed in the pore liquor continues to evolve. This ageing process occurs via three steps: polymerisation, syneresis and coarsening. Polymerization of unreacted hydroxyl groups increases the connectivity of the gel network; this process runs in parallel with some shrinkage. Syneresis is the spontaneous and irreversible shrinkage of the gel network, resulting in expulsion of pore liquid. The driving forces of the flow liquid produce compressive stresses that draw the solid network into the liquid. Coarsening or ripening refers to a process of dissolution and reprecipitation driven by differences in solubility between surfaces with different radii of curvature. This process does not produce shrinkage of the network but influences the strengthening of the gel and depends on factors that affect the solubility, such as temperature, pH, concentration and type of solvent.

- **Drying**

The drying process of a porous material can be divided into several stages: At first, the body shrinks by an amount equal to the volume of liquid that evaporates and the liquid-vapor interface remains at the exterior surface of the body. The second stage begins when the body becomes too stiff to shrink, leaving air-filled pores near the surface. Even as air invades the pores, a continuous liquid film supports flow to the exterior, so evaporation continues to occur from the surface of the body. Eventually, the liquid becomes isolated into pockets and drying

can proceed only by evaporation of the liquid within the body and diffusion of the vapor to the outside.

- **Sintering**

This is the process of the network densification, which is driven by interfacial energy. Solid network moves by viscous flow or diffusion to eliminate porosity. In gels with high pore surface areas, the driving forces is great enough to produce sintering at exceptionally low temperatures, where the transport processes are relatively slow. Indeed, the kinetics of densification in gels is not simple because of the concurrent processes of dehydroxylation and structural relaxation. As an example, constant heating rate was used by Prassas et *al*. [3] to study the sintering process in aerogels (70-90% porosity, 0.1-0.5 $g \cdot cm^{-3}$ density) and they conclude that several mechanisms are involved in such sintering process. Below 700ºC, sintering is conducted by a diffusional process due to chemical reactions, while above 750ºC begins the viscous flow mechanism and the activation energy of this process is related to the hydroxyl content.

II.1.2. Sol-gel products

Different materials of high purity and homogeneity such as polymers, films, monoliths, fibres, etc… could be synthesized using the sol-gel process (Figure II.1).

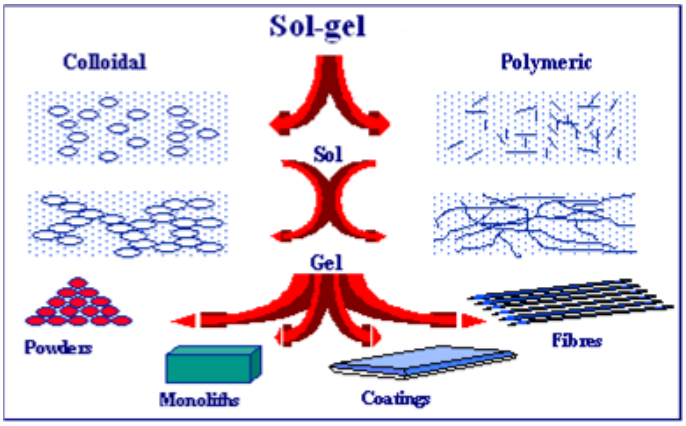

Figure II. 1 *Schema of sol-gel products*

One of the most famous sol-gel products is the thin film, which can be obtained on a piece of substrate by deposition techniques such as spin-coating, dip-coating, etc… Drying the gel at low temperature under ambient atmosphere makes it possible to obtain porous solid matrices known as xerogels. Densification at high temperature of the xerogel allows obtaining a dense matrix, which will be used in the fabrication of optical fibres. In this work, porous and dense silica were

used as matrices to incorporate nanoparticles. Hence, detailed information about the synthesis of these matrices is given in the next paragraphs.

II.1.2.1. Porous silica matrix (Xerogel)

Xerogel is a solid formed from a gel by drying it. Usually, it retains high porosity and high surface area, along with very small pore size. Our xerogels were obtained from gel monoliths that have been synthesized using tetramethyl orthosilicate (TMOS, Aldrich) under basic conditions (ammonia) in the presence of water and methanol. The molar ratio of TMOS, methanol, water was kept to 1:4:10, respectively. Firstly, the sol was vigorously stirred and poured into flasks for gelation. Afterward, the gels were aged at 50°C under atmospheric conditions. Stabilization of the xerogels was achieved by annealing the samples at 850°C for 1 h to eliminate organic residues. Glassy colourless and crack-free planar-like monoliths were obtained with a thickness of about 2 mm, having good optical transparency and mechanical strength with different shapes as shown in Figure II.2. Characterisation of these xerogels will be discussed at the end of this chapter.

Figure II. 2 *Silica xerogels obtained from sol-gel reactions with TMOS*

II.1.2.2. Dense silica glass

The synthesis of the pure silica glass matrix has been already described elsewhere [1] using TEOS as a precursor. The obtained sols were poured into cylindrical recipient and carefully covered. The tubes were then heated at 50°C to induce gel formation. The wet gels were dried for several days at 50°C, which generally led to opaque white ones with TEOS precursors. This temperature was chosen as a good compromise in order to optimize the syneresis rate and to

avoid cracks inside the wet gel structure. The cylindrically shaped samples were then slowly heated up to 180°C under vacuum and kept at this temperature for many days in order to evacuate most of the organic solvents and water. Thereafter, the dried gels were heated up to a temperature of 850°C, then maintained at this temperature for few hours. The obtained xerogels still show the opaque white colour, contrary to the case of the TMOS precursor as already shown in section II.1.2.1. After a doping step with the desired solution, as described in the next section, a further heat-treatment of the xerogels was performed in air atmosphere with a gradual increase of the temperature from the room temperature to 1200°C. At the end, transparent glassy cylindrical silica rods have been obtained.

II.2. Nanoparticles Doped dielectric matrices

II.2.1. Methods of doping inside sol-gel matrices

Noble metals (Ag, Au, Cu) or semiconductor compounds (CdS, PbS) can be added to the silica matrices as dopants. The methods used to dope the silica matrices are:

1- **Sol-doping method** in which the dopant is added to the sol. For example, Yang et *al*. [4] have shown that PbS nano-crystallites can be formed in bulk silica gels by adding the precursors ($Pb(CH_3COO)_2.H_2O$) and Na_2S to the sol before the formation of the porous gel, and then by heating the doped gel at a temperature of 50°C for 10h.

2- **Impregnation method** by which the dopant is added after the formation of the silica porous xerogel. In this method, the porous matrix is immersed for some hours into a solution composed of a solvent (e.g. water, alcohol, etc…) and of the precursors of the nanoparticles (e.g. cadmium acetate (Cd), thiourea (S)). Subsequently, the impregnated samples are taken out from the solutions, then dried to remove solvents and retain the precursors within the pores. This method obviously needs matrices presenting large interconnected pores.

3- **Mixed method** where dopants are added to the sol. The added dopant is usually the cation precursors. For example, Nogami et *al*. [5] have shown that II-VI crystallites can be formed in bulk silica gels by adding the precursors of cadmium acetate to the sol, and then by exposing the doped xerogel to H_2S gas.

All of these methods may lead to nanoparticles-doped silica matrices. In general, the precipitation of nanoparticles using the sol-doping methods is obtained by heating at low temperature. Hence, the obtained samples can not be stabilized at high temperature, due to the oxidation of the nanoparticles, especially for PbS, CdS and Ag. On the contrary, using the impregnation method, the porous silica matrix can be prepared and stabilized at high temperature before doping and thus before the nanoparticles formation. Consequently, this post-doping method has been used throughout this work.

From the nitrogen sorption measurements performed on both types of matrices (the technique will be described in the end of this chapter), the pore size diameter of the obtained xerogels was significant, with an important specific area, which motivated us to dope the pores of the obtained xerogel by impregnation with appropriate precursor solutions. Using this method, the nanoparticles can be formed after a heat-treatment as in the case of sol-doping method. But post-doping also gives the possibility to localise the nanoparticles formation under laser irradiation. The irradiation techniques are described in the next paragraph.

II.2.2. Laser irradiation techniques

We have used different irradiation techniques which depend on the laser source. Three different lasers have been used in order to localise the formation of the metallic and semiconductor nanoparticles: Ti:Sapphire femtosecond pulsed laser, UV excimer nanosecond pulsed laser and visible continuous laser.

II.2.2.1. Ti:Sapphire femtosecond laser

A Tsunami Ti:Sapphire oscillator (Spectra-Physics), followed by a regenerative amplifier, produces 40 fs, 120 fs or 40 ps pulses at 800 nm with a 1 kHz repetition rate. In this thesis, all the experiments have been performed using 120 fs pulses. Figure II.3 shows the experimental setup where the incident laser beam, with an average power of 2 W, was focused into the doped silica samples through a 10× microscope objective with a numerical aperture of 0.3.

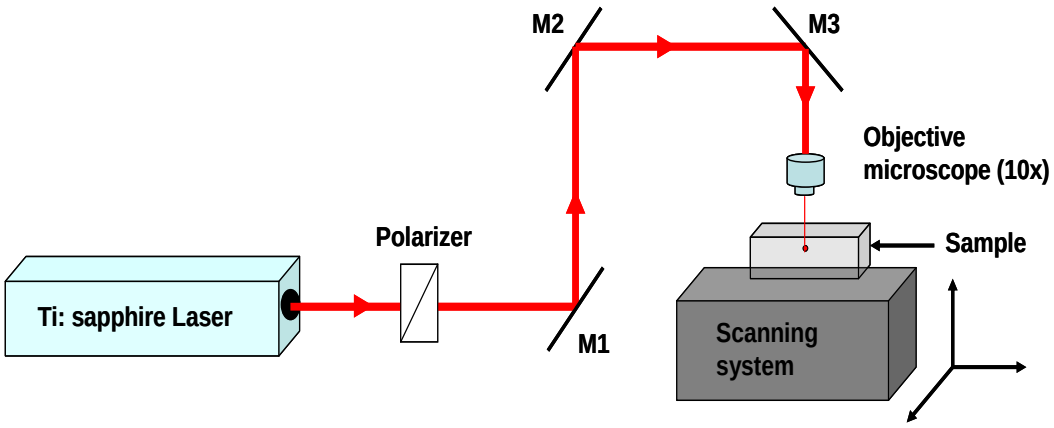

Figure II. 3 *Setup of Ti:Sapphire femtosecond pulsed laser irradiation*

An automated scanning system allowed the irradiation in three dimensions. The incident spot diameter on the microscope objective was of 7 mm and the focalised spot on the sample was of a diameter estimated to 2 μm. The laser power could be controlled using a polarizer.

II.2.2.2. Excimer laser

The ultraviolet laser uses a mixture of noble gas argon (Ar) and of the reactive gas fluorine. The ArF laser operates at 193 nm with a 10 Hz repetition rate. Figure II.4 presents, the simple setup of the experiment that has been used to localise the precipitation of the metallic nanoparticles inside silica dense matrices.

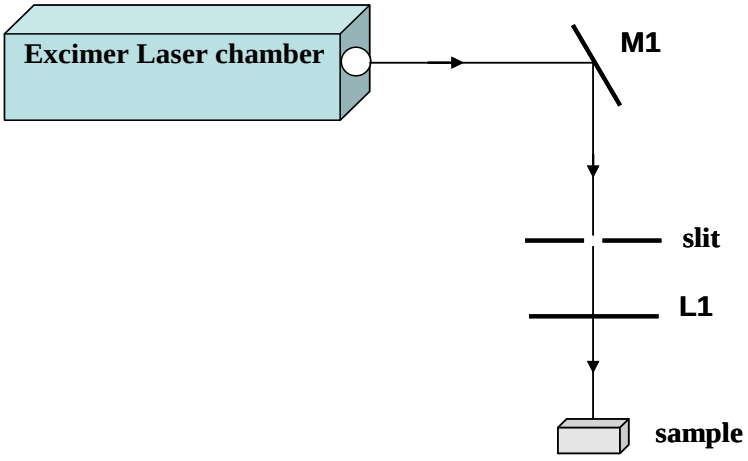

Figure II. 4 *Setup of ArF excimer pulsed laser irradiation*

The incident laser beam, with an energy per pulse of 60 mJ, passes through a slit in order to obtain a rectangular shape and is then focalized by a lens (f = 30 cm) onto the doped silica samples. The so-focused laser spot was 1.4 cm long and 300 µm wide. The energy density has been estimated to 1.4 J.cm^{-2}.

II.2.2.3. Visible continuous-wave laser

The argon laser is a continuous wave laser emitting a blue or green visible light. In this thesis, the visible irradiation was performed using the micro-Raman set-up of a T64000 Jobin-Yvon spectrometer. Figure II.5 presents the schematic setup where the 514.5 nm radiation of an argon laser was focused on the surface of the matrix via a 10× microscope objective, with a numerical aperture of 0.25.

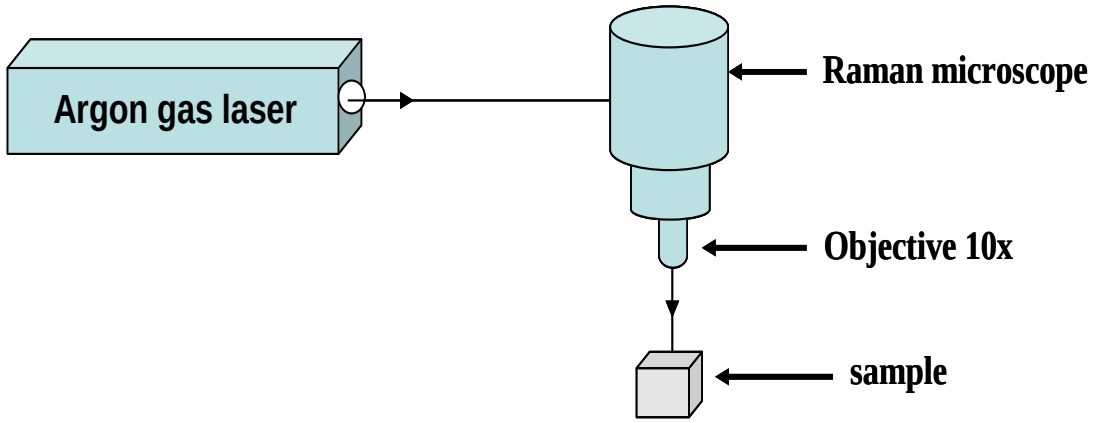

Figure II. 5 *Setup of Ar^+ visible continuous laser irradiation*

The laser power could be increased up to 2 W, which corresponds, after all optical components in the microscope, to 140 mW at the focal point. The laser spot, of diameter 10 μm, was moved laterally with a scanning speed of 1 mm s^{-1} to obtain a sufficient surface for the characterizations. The separation distance between the irradiated lines was adjusted in order to avoid the re-irradiation of the same area. This distance depended on the laser power, as well as on the dopant concentration.

II.2.3. Embedding semiconductor and metal nanoparticles inside dielectric matrices: a state of the art

In order to take advantage of the optical properties of these semiconductor and metal nanoparticles in a stable and reproducible way, the NCs should grow or should be inserted inside a matrix. Dielectric matrices and particularly glasses are well-suited in order to employ these nanoparticles in technological devices, like planar waveguides, lasers or optical fibres. In this section, we review, from the literature, the fabrication methods for generating semiconducting and metallic nanoparticles inside dielectric matrices. Most of the previous works have concerned the NC growth by thermal treatment of the matrices.

II.2.3.1. Precipitation of semiconductor nanoparticles in dielectric matrices

Semiconductor nanoparticles have been precipitated inside different dielectric matrices such as TiO_2 [6], ZrO_2 [7] or silica matrices [8-11], etc… For instance, CdS and PbS semiconductors nanoparticles of various sizes inside porous xerogel silica matrices were prepared by Parvathy et *al*. [8, 9]. In the first step of their samples preparation, the Pb^{2+} or Cd^{2+} ions were inserted in a silica xerogels prepared through hydrolysis and condensation of TMOS precursor, methanol as a diluting agent, ammonium hydroxide (NH_4OH) as a catalyst water and a methanolic lead nitrate $Pb(NO_3)_2$ solution. Then, PbS crystallites are formed by passing H_2S gas at temperatures between 50 and 350°C over the Pb^{2+}, Cd^{2+} ions incorporated in silica xerogels. Influences of the heating temperature and of the concentration have been reported. For example, Figure II.6 presents the absorption spectra of PbS nanoparticles embedded inside silica xerogels as a function of the molar ratio between PbS and TMOS. As shown in the figure, the absorption threshold shifted from higher to lower wavelength with decreasing PbS/TMOS molar ratio, reflecting an increase in the band gap energies and thus a decrease of the PbS nanoparticles sizes.

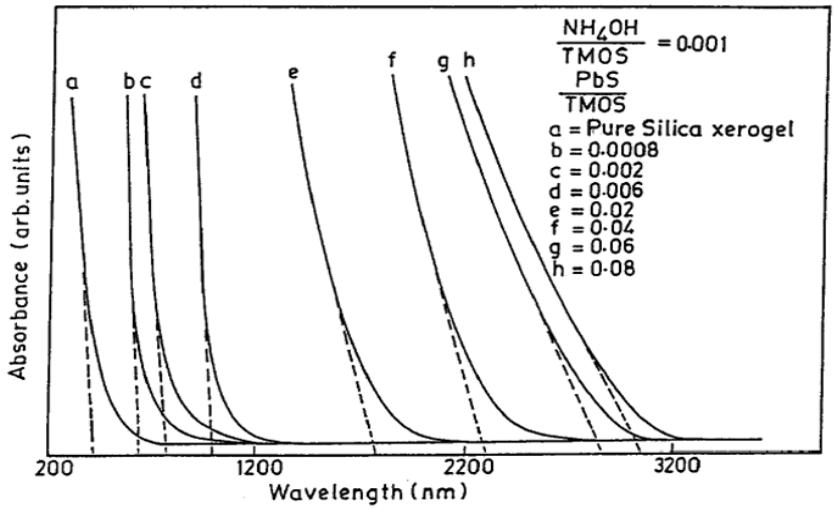

Figure II. 6 *Absorption spectra of PbS nanoparticles embedded inside silica xerogel [11].*

Semiconductor nanocrystals embedded inside silicate matrices have been prepared by various techniques [12-16]. For example, in the melting method, nanocrystals are precipitated by annealing the melting glass close to the glassy transition temperature. Figure II.7 presents the influence of the heating time on the absorption and photoluminescence responses of PbS quantum dots grown inside a silicate glass. Figure II.7 (a) shows that, when increasing the treatment time or the temperature, the absorption peak is shifted toward longer wavelength,

which indicates an increase in the nanoparticle size. As the size of PbS QDs is increased, the maximum of the PL band also shifted from 1166 to 1680 nm, as shown in Figure II.7 (b). A Stokes-shift of approximately 100 meV, when compared to the absorption edge position, has been noticed.

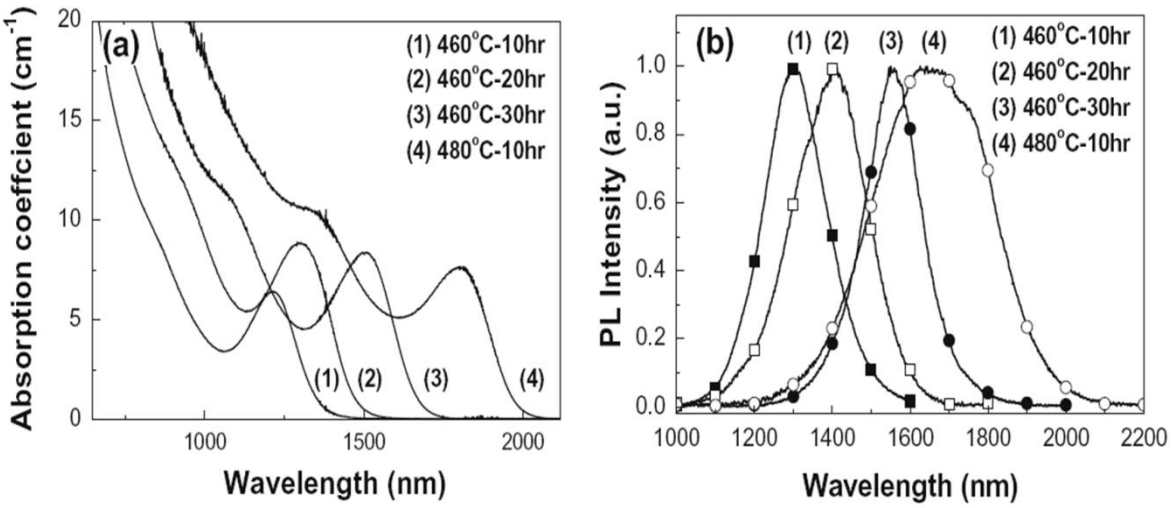

Figure II. 7 *PbS quantum dot embedded inside silica based glass matrices: (a) absorption spectra and (b) photoluminescence spectra [16].*

In all of these cases, the nanoparticles are precipitated by heat-treatment without space localization. Until recently, few works have been reported on the space selective growth of semiconducting nanoparticles inside dielectric matrices. Local precipitation of these nanoparticles could be achieved using continuous infrared laser irradiation [17] or pulsed laser irradiation followed with heat-treatment after the irradiation [18-21].

In a previous report [17], an infrared continuous laser was used to precipitate CdS nanoparticles inside silica aerogels. However, this method needs many restrictive steps to keep the hydrogel at low temperature in order to avoid the spontaneous formation of CdS nanoparticles. Lithographed features with a diameter of about 40 µm, which extended inside a monolith up to 4 mm, were obtained by these authors. On the other hand, the silica aerogels are known to be non transparent materials, as compared to silica xerogels, which are more compatible with optoelectronics applications. The technique of laser irradiation can be applied to thin film. A precipitation of CdS nanoparticles under a femtosecond laser beam inside a ZrO_2 matrix deposited onto glass substrate using femtosecond laser has been reported recently in our team [18]. The samples were first heated for 30 min at 200°C and a photoinitiator has been added in the sol in order to create CdS nanoparticles by a two-photon absorption process. Raulin et *al*.

[19] have also localised the formation of CdS nanoparticles embedded inside bulk silica xerogel matrices using a 193 nm pulsed ArF excimer laser. In this case, however, it was necessary to heat the samples at a temperature ranging between 50 and 100°C during the irradiation process. Figure II.8 (left) shows Raman spectra of the irradiated zones with different laser pulse number.

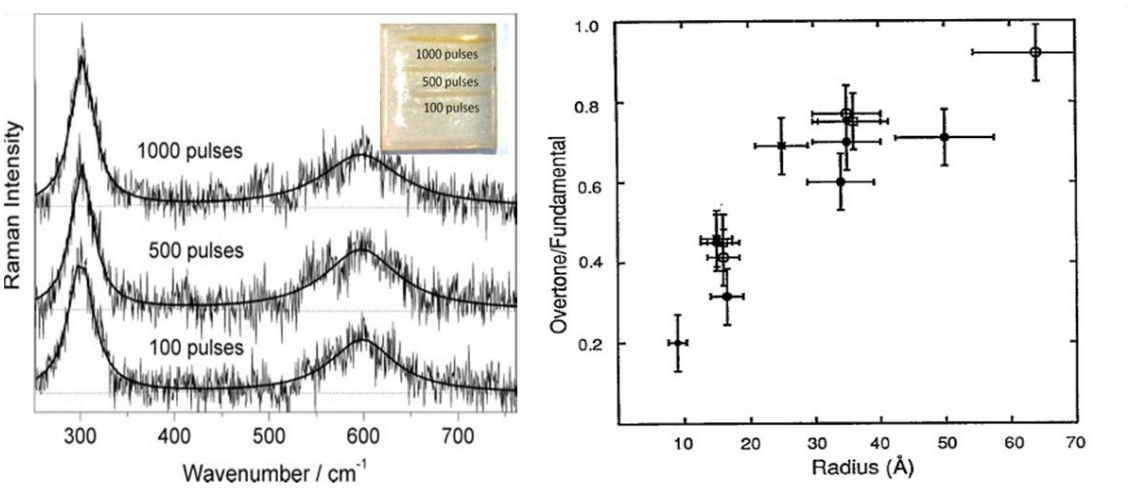

Figure II. 8 *Left: UV Raman spectra (λ_{ex} = 325 nm) of a silica xerogel doped with Cd^{2+} and S^{2+} precursors as a function of pulse number. Inset image shows the yellow lines attributed to CdS nanoparticles [19].Right: Size dependence of the ratio of the overtone to the fundamental [23].*

The observed bands at 300 and 600 cm^{-1} are assigned to the longitudinal optical phonon bands (1LO and its first overtone 2LO), respectively. These features attest to the creation of CdS nanoparticles [22]. The intensity ratio between 2LO and 1LO allowed to estimate the CdS particle size using Figure II.8 (right), as already describe elsewhere [23].

Moreover, space-controlled formation of PbS nanoparticles inside melting glass using femtosecond laser irradiation has been reported [20-21]. Nobuhito et *al*. [20] reported the local precipitation of PbS inside melting glass without annealing using a pulsed femtosecond laser irradiation at high repetition rate (800 nm, 250 KHz, 200 fs). They have succeeded in fabricating a periodic structure with a difference in the relative refractive index of 20 % between the irradiated area and the non-irradiated areas. However, no clear evidence of the presence of PbS nanoparticles is given. Chao et *al*. [21] also used pulsed femtosecond laser irradiation (800 nm, 1 KHz, 184 fs) followed by a heat-treatment at 450 °C to precipitate PbS nanoparticles inside irradiated areas of a melted glass. They have studied the influence of the laser power on the optical response of the PbS nanoparticles. Figure II.9 shows the PL spectra recorded from the glass irradiated with different pulse energies. Shifts toward the longer wavelengths have been

observed as increasing of the laser power which indicates that the size PbS QDs formed in the irradiated region become bigger with increasing of laser power.

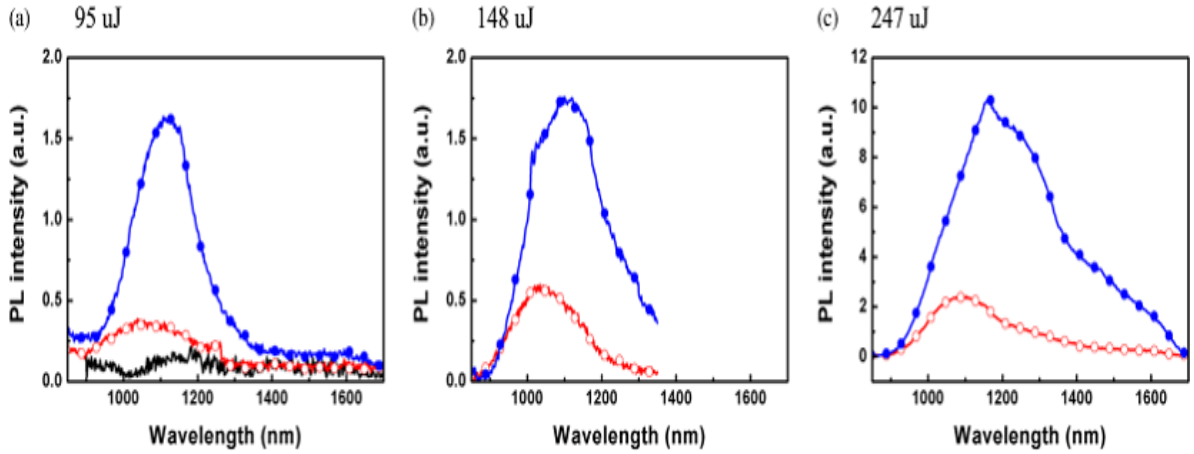

Figure II. 9 *Photoluminescence (PL) spectra recorded from the irradiated area (blue lines) and from the non-irradiated area (red lines) after femtosecond irradiation at different energies and after heat-treatment. The black solid line in (a) was recorded from the irradiated zone before heat-treatment [21].*

II.2.3.2. Precipitation of metallic nanoparticles inside dielectric matrices

A lot of studies have reported the precipitation of noble metal nanoparticles inside dielectric matrices such as TiO_2 [24, 25], ZrO_2 [26, 27] and silica [28-34]. However, the most widely used dielectric matrices are porous and dense silica matrices. Such glasses doped with metallic nanoparticles can be prepared via different methods such as electrochemical, melting quenching, sol-gel process, etc…

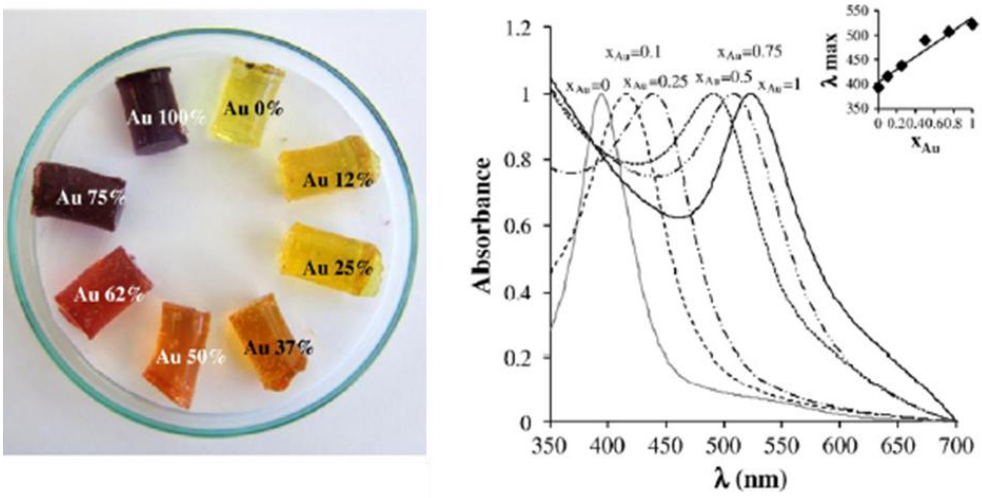

Figure II. 10 *Silica gels produced from colloidal alloy solutions (Ag-Au) by varying the concentration of gold; Left: photograph images. Right: absorption spectra [34].*

Variously coloured silica glasses doped with nanoalloy of gold-silver were prepared using the sol-gel route [34]. Firstly, the nanoparticles were prepared using Turkevich method [35] and then incorporated to the TMOS-derived sol. Figure II.10 shows such coloured silica gels for varying gold concentrations and the corresponding optical absorption spectra. As it can be seen, the colours of the gels vary continuously from yellow to deep red with the increasing gold concentration, reflecting a red-shift of the SPR position. Such a red-shift is ascribed to an increase in the mean particle size.

Copper nanoparticles growth in silica matrix can also be obtained by annealing a sol–gel prepared porous matrix impregnated with copper nitrate as reported by Yeshchenko et *al* [31]. Their porous silica matrices were produced by the conventional sol–gel technique based on hydrolysis of tetraethoxysilane (TEOS). Then, the samples were soaked in an alcoholic solution of copper nitrate, before being densified at 1200°C under air, air and hydrogen or hydrogen atmospheres. These densifications lead to the formation of copper nanoparticles.

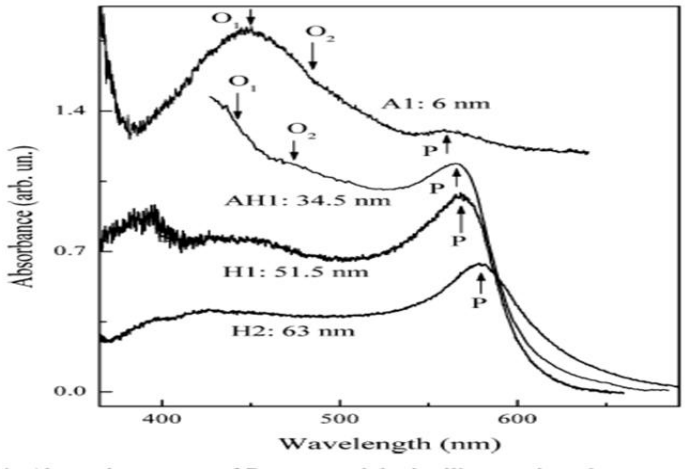

Figure II. 11 *Absorption spectra of Cu nanoparticles in silica matrices, demonstrating the blue shift of the surface plasmon peak with decrease of the particle size. P marks the absorption band of the surface plasmon in Cu nanoparticles, O_1 and O_2 are the absorption bands of Cu_2O [31].*

Figure II.11 presents the optical absorption of copper nanoparticles embedded inside the resulting silica glasses heated under different conditions. A small blue shift of SPR peak with the decrease of the Cu nanoparticle size is observed in the absorption spectra. Moreover, the authors showed that the annealing under air conditions leads to the formation of copper oxide (Cu_2O), the absorption of which is labelled O_1 and O_2 in the figure. On the contrary, the annealing under hydrogen atmosphere leads to the formation of only copper nanoparticles inside the silica glass matrix.

Recently, there have been intensive researches focused on the precipitation of the metallic nanoparticles inside silica glass matrices with space selective growth. For example, Qiu et *al.* [36-38] reported the space-selective precipitation of silver and gold nanoparticles inside melted silicate glasses using femtosecond laser irradiation and subsequent annealing at high temperatures. Furthermore, infrared nanosecond laser irradiations have been used to localise the precipitation of copper nanoparticles doped inside commercial melted glass [39]. Figure II.12 shows the absorption spectra of the doped melted glass before and after the pulsed infrared irradiation.

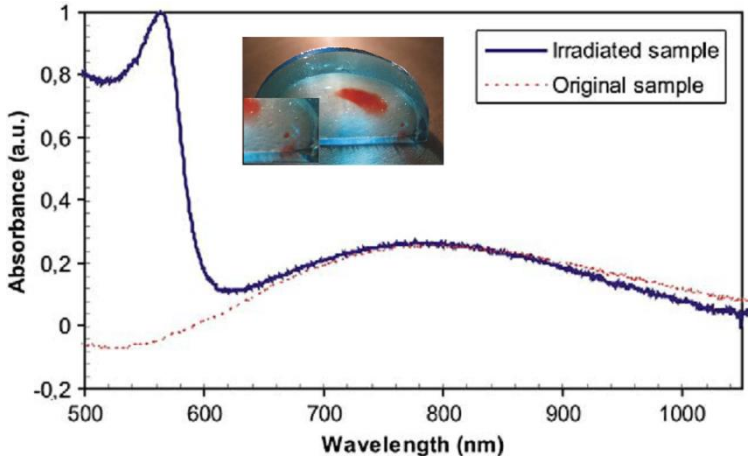

Figure II. 12 *Absorption spectra of a doped glass sample before and after ns laser irradiation with further annealing at 700°C for 1 h [39].*

The colour of the sample was blue after doping with the copper ions, as shown in the inset image. The absorption spectra of the unirradiated area shows a wide absorption band centred around 800 nm, which corresponds to the existence of Cu^{2+}. The irradiation at 1064 nm by infrared laser allowed the reduction of the copper ions to the copper atoms in the irradiated area. Then, the annealing at 700°C led to the aggregation of the copper nanoparticles (red colour) with a clear SPR peak centred at 560 nm.

The most interesting property of these dense silicate matrices doped with metallic nanoparticles is their ability to keep and protect the nanoparticles at high temperature. Hence, these matrices can be hopefully used to draw optical fibers, as it will be shown in the next paragraph.

II.3. Incorporation of nanoparticles inside Microstructured Optical Fibre (MOF)

II.3.1. Silica preform preparation

The most usual method to prepare fibre preforms is the modified chemical vapor deposition (MCVD). Figure II.13 shows the schematic setup of this process. A mixture of ultra-pure gases (usually $SiCl_4$ and O_2) flows through a commercial silica tube while a high temperature is applied from the outside.

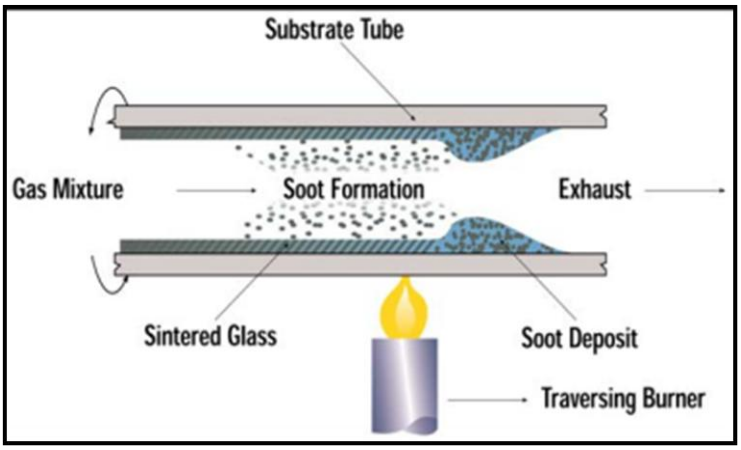

Figure II. 13 *Scheme of MCVD process [40].*

The heat source converts the gases into silica "soot". As the burner is translated along the tube, the fine soot particles are deposited on the inner wall of the tube. This process is continued, layer by layer, to construct the complex core structure of the optical fibre. Once the soot is deposited, the tube is collapsed into a solid rod called a preform by applying several high-temperatures backwards and forwards of the heater. This process must be carefully controlled to assure that there are no defects such as a "center dip" or a "center-line spike" in the index profile.

In the case of the sol-gel process, the preparation of the silica performs is based on the hydrolysis and condensation of the alkoxides, as already explained in section II.1.2.2. As compared to the MCVD process, this process provides many advantages, which include simplicity in the handling of the doped silica preform, low cost of the precursors, low temperature processing and the subsequently possibility to preserve the dopants after drawing of the optical fibre. For these reasons, we used the sol-gel process to prepare our silica preforms doped with metallic nanoparticles.

II.3.2. General properties and fabrication method of a MOF

Typically, the conventional communication optical fibres are made from two different layers of silica glass: an inner core that is doped, for example by adding small amounts of germanium, and an outer cladding of pure silica. The germanium doping raises the refractive index of the core relative to the cladding region. This difference in refractive index confines light to the core via total internal reflection. Light is then guided in the core of the fibre. In recent years, two new types of optical fibres, having the potential to revolutionize the communication and sensing industry, have been developed, bringing with them a wide range of novel optical properties. These new fibres, known collectively as microstructured fibres, can be made entirely from one type of glass, as they do not rely on dopants for guidance. Instead, the cladding region is peppered with many small air holes that run the entire fibre length.

The MOFs are constructed using one of two basic design types, containing either a solid or a hollow core. The former is typically made of silica (see Figure II.4 (left)) which, as for most conventional fibres, relies on total internal reflection. The latter typically contains air (see Figure II.4 (right)) and the light propagation in these fibres relies on a photonic band gap that restricts the guidance to the core.

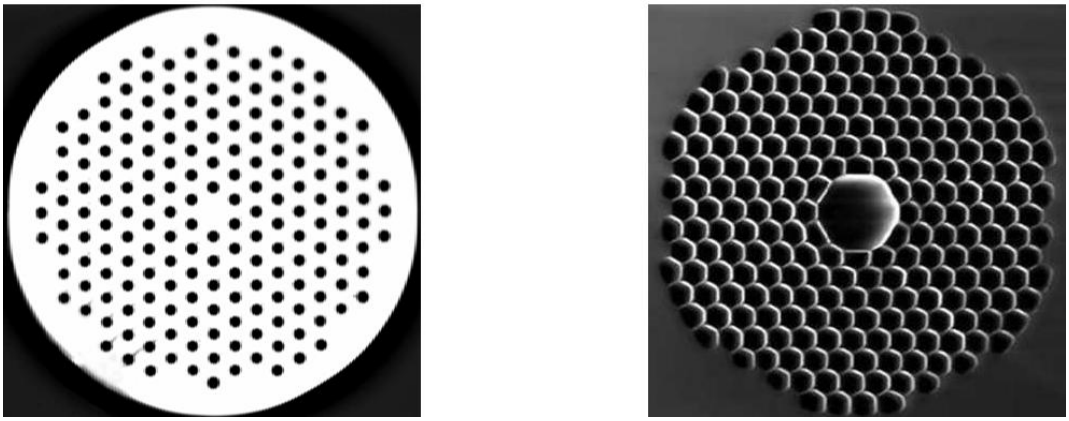

Figure II. 14 *(Left) Solid-core and (Right) hollow-core fibre cross-sections [41].*

Fabrication of MOF, like in conventional fibre fabrication, starts with a fibre preform. Conventional preforms are formed using either modified chemical vapour deposition or vapour axial deposition process. Microstructured preforms are formed by stacking a number of capillary silica tubes and rods to form the desired air/silica structure, fusing the stack into a preform, and then pulling the preform to a fibre at a sufficiently high temperature (~2000°C) (Figure II.5).

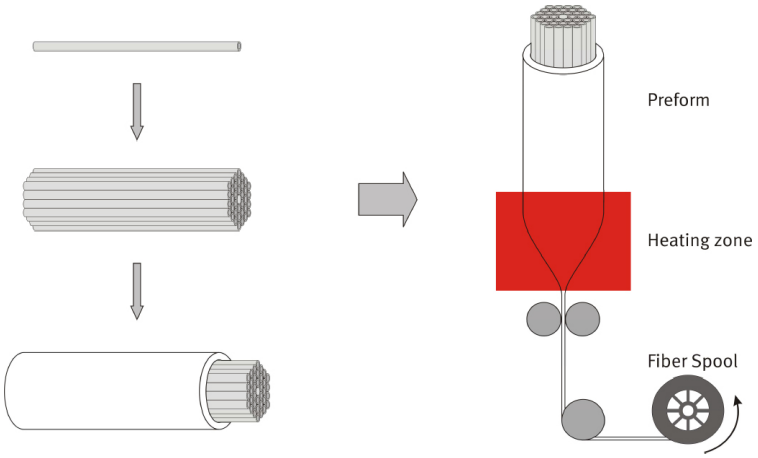

Figure II. 15 *Stack and draw process and the drawing of the MOF [41].*

II.3.3. State of the arts of metal and semiconductor nanoparticles-doped optical fibers

The achievement of glasses doped with metal or semiconductor nanoparticles is mainly limited to thin films or bulk materials, and there are few reports on the insertion of such nano-objects in the core of an optical fiber. Recently however, the doping of optical fibers with nanostructures has caused significant scientific interest in different application fields. Various doping techniques have been carried out, such as the insertion of PbS QDs inside the random holes of a MOF by colloidal impregnation [42]. The same kind of study has been performed by Chillcce et *al.* [43] who spread PbS nanoparticles on the core surface of a silica MOF. In this case, the PbS nanoparticles solution has been injected into fiber's holes under pressure. Then, to remove the remaining solution, just keeping a nano-thick QD layer, a N_2 pressure was applied to the fibre until gas bubbles appeared at the free end of the MOF. Although this technique has the great interest of avoiding heat-treatment of the NCs, the resulting doped fibre device presents a limited lifetime, due to the probable oxidation of the chalcogenide QD surrounded by air.

Our strategy will be rather centred on a solid fibre core doping technique, even if it implies a finer control of the constituting material. For this kind of technique, it is worthy to note that previous attempts are actually scarce and that most of the results found in the literature are open to doubt. For example, the linear and nonlinear optical properties of a germano-silicate optical fibre doped with PbSe nanocrystals have been described by Watekar et *al*. [44]. The fibre preform was fabricated using MCVD method and the core of the fibre was doubly doped using a solution-doping technique with an acidic solution containing Pb and Se. The same team [45] has also reported the incorporation of PbTe QDs in a germano-silicate fibre using the atomization

techniques. However, in these papers, no clear proof of the presence of these chalcogenide nanocrystals has been given in the final fibre.

Concerning metal nanoparticles, the glassy core doping process is made easier by a better stability under heat-treatment. Correa et *al*. [46] have reported the incorporation of silver nanoparticles within a MOF by high pressure chemical deposition. Dhawan et *al*. [47] have shown the efficient but quite localized gold metallic nanoparticles doping of an optical fibre using an approach based on the coating of the fibre end and the splicing to a second fibre. On the contrary, Ju et *al*. [48] have applied their solution-doping technique using a gold precursor on a conventional MCVD fibre preform, similarly to what is done to achieve rare-earth doped fibre. However, the spectral position of the SPR peak in the final fibre is not really convincing. Looking in details, it appears that most of the efficient reported methods can only lead to short doped pieces of fibres, thus limiting their applications.

II.4. Characterisation techniques

Different techniques have been used in routine to characterise our samples. Theses techniques are: Nitrogen adsorption-desorption isotherm, Raman spectroscopy, Photoluminescence spectroscopy, X-ray Diffraction (XRD) and Transmission Electron Microscopy (TEM).

II.4.1. Nitrogen adsorption-desorption isotherm

Specific surface area and porosity are important parameters that influence the quality and utility of many materials. In physical gas adsorption, an inert gas, mostly nitrogen, is adsorbed on the surface of a solid material. This occurs on the outer surface and, in the case of porous materials, also on the surface of pores. The Brunauer-Emmett-Teller (BET) [49] gas adsorption method has become the most widely used standard procedure for the determination of the specific surface area of finely divided and porous materials, in spite of the oversimplification of the model on which the calculation is based. The BET surface area measurement is crucial in understanding the behaviour of a porous material: as a material reacts with its surroundings via its surface, a higher surface area material is more likely to react faster, dissolve faster and adsorb more fluid than a similar material with a lower surface area.

Typical analysis would include:

- **Specific surface area:** BET surface area analysis using Nitrogen for low surface area materials

- **Pore size analysis:** Mesopore analysis using traditional Kelvin equation models such as the model of Barrett, Joyner and Halenda (BJH) (pore size distribution, pore diameter, pore volume and pore surface area).

Clean solid surfaces adsorb surrounding gas molecules, and BET theory provides a mathematical model for the process of gas sorption. This physical adsorption of a gas over the entire exposed surface of a material and the filling of pores is called physisorption.

The determination of the specific area, as well as the characterisation of the porous volume and of the pore diameter, is obtained from the nitrogen adsorption-desorption isotherm. Prior to the recording of an adsorption isotherm, the physisorbed species must be removed from the surface of the adsorbent. This may be achieved by out-gassing, i.e. by exposure of the surface to a high vacuum usually at elevated temperature. The outgassing conditions required to attain reproducible isotherms (temperature program and change in pressure over the adsorbent) must be controlled within limits which are dependent on the adsorption system.

Pore size range is divided in three domains: micropores (< 2nm), mesopores (≈ 2-50nm) and macropores (> 50nm).

It is customary to apply the BET equation in the linear form

$$\frac{P}{n^a.(P^0 - P)} = \frac{1}{n_m^a.C} + \frac{(C-1)}{n_m^a.C}.\frac{P}{P^0} \qquad \textbf{Eq.(II.1)}$$

where n^a is the amount of nitrogen adsorbed at the relative pressure P/P^0 and n_m^a is the monolayer capacity. According to the BET theory, C is related to the enthalpy (heat) of adsorption in the first adsorbed layer. Hence, the BET equation requires a linear relation between $\frac{P}{n^a.(P^0 - P)}$ and P/P^0 (i.e. the BET Plot). From this straight line of type $y = ax + b$ with $a = \frac{(C-1)}{n_m^a.C}$ and $b = \frac{1}{n_m^a.C}$, we can calculate the total and specific surface area using the following equations:

$$A_S(BET) = n_m^a.N_A.a_m \qquad \textbf{Eq.(II.2)}$$

$$a_S(BET) = \frac{A_S(BET)}{m} \qquad \textbf{Eq.(II.3)}$$

where a_m is the molecular cross section area, N_A is the Avogadro number, m is the adsorbent mass, $A_s(BET)$ and $a_s(BET)$ are the total and specific surface area of the adsorbent, respectively.

The most used method to estimate the distribution of the mesopore size is the method of BJH [50]. This method is based on the Kelvin equation relating the pore radius r_p and the pressure p for a known gas and solid.

$$r_p = \frac{C_1}{\ln\left(\frac{P}{P^0}\right)} + t \qquad \textbf{Eq.(II.4)}$$

with t the multilayer thickness and C_1 a constant characteristic of the absorbed layer. In the calculation of the mesopore size distribution from physisorption isotherms, it is generally assumed that:

- The pores are rigid and have regular shape (e.g. cylindrical capillaries or parallel sided slits),
- The micropores are absent
- The size distribution does not extend continuously from the mesopore to the macropore range.

Furthermore, to obtain the pore size distribution, which is usually expressed in the graphical form $\Delta V/\Delta r$ vs. r_p, allowance must be made for the effect of multilayer adsorption in progressively reducing the dimensions of the free pore space available for capillary condensation. More information about this technique is given elsewhere [49, 50]. In this work, we have used the Quantachrome porosimeter Autsorb-1. Prior to the experiments, our samples were outgassed at 150°C for several hours under a secondary vacuum with a pressure less than 10^{-6} Torr.

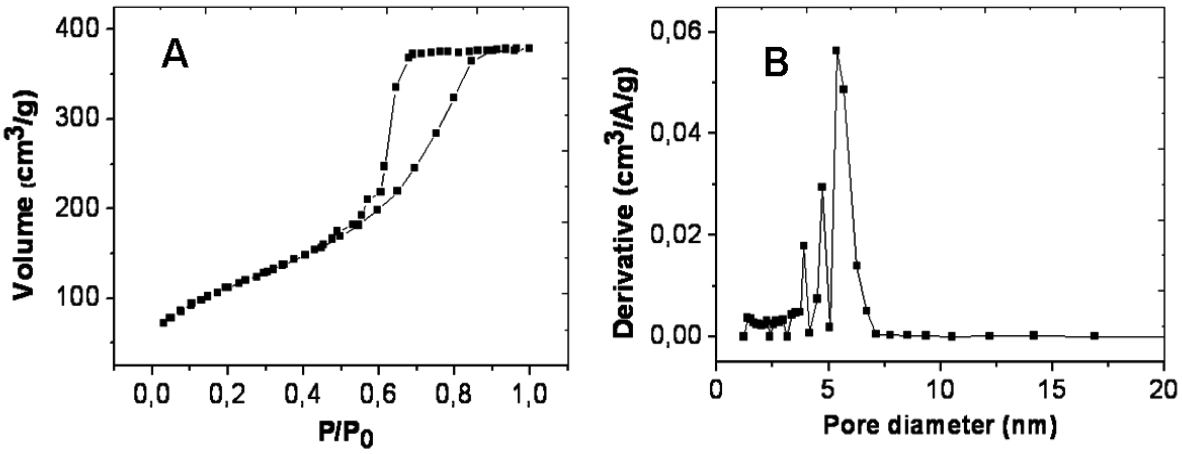

Figure II. 16 *A: N2-adsorption–desorption isotherm and B: pore size (diameter) distribution (calculated by the BJH method) of a silica xerogel stabilized at 850 ◦C in air.*

Figure II.16 presents the isotherm profile and the total pore size distribution of a typical silica xerogel, interpreted by using the BET and BJH models. The isotherm profile shown in Figure II.16 (A) corresponds to a type IV curve, which reveals a mesoporous structure according to the classification of Brunauer [49]. The hysteresis loop has an H2 character, which matches with filling and emptying of mesopores through capillary condensation in mesoporous solids with pore interconnectivity, according to the IUPAC classification [51]. The pore size distribution, obtained by the BJH method (Figure II.16 (B)), is centred on 5.4 nm. The BET surface area and the total pore volume were estimated to 360 $m^2 .g^{-1}$ and 0.49 $cm^3.g^{-1}$ respectively.

II.4.2. Raman spectroscopy

Raman spectroscopy is a technique based on inelastic scattering of monochromatic light, usually from a laser source. In the Raman effect, photons of the laser light are scattered from the sample and reemitted at a frequency shifted up or down in comparison with laser line. This shift provides information about vibrational, rotational and other low-frequency transitions in molecules. Raman spectroscopy can be used to study solid, liquid and gaseous samples. The Raman effect is based on molecular deformations in electric field E determined by molecular polarizability α. The laser beam can be considered as an oscillating electromagnetic wave with electrical vector (E). Upon interaction with the vitreous sample, it induces electric dipole momentum $\mathbf{P} = \alpha\mathbf{E}$ which deforms molecules. Because of periodic deformation, molecules start vibrating with a characteristic frequency υ_m.

Amplitude of vibration is called nuclear displacement. In other words, monochromatic laser light with frequency υ_0 excites molecules and transforms them into oscillating dipoles. Such oscillating dipoles emit light of three different frequencies (Figure II.17) when:

1. A molecule with no Raman-active modes absorbs a photon with the frequency υ_0, the excited molecule returns back to the same basic vibrational state and emits light with the same frequency υ_0 as the excitation source. This type of interaction is called elastic Rayleigh scattering.

2. A photon with frequency υ_0 is absorbed by Raman-active molecule which, at the time of interaction is in the basic vibrational state. Part of the photon's energy is transferred to the Raman-active mode with frequency υ_m and the resulting frequency of scattered light is reduced to $\upsilon_0 - \upsilon_m$. This Raman frequency is called Stokes frequency.

3. A photon with frequency υ_0 is absorbed by a Raman-active molecule, which, at the time of interaction, is already in the excited vibrational state. Exceeding energy of excited Raman active mode is released and the molecule returns to the basic vibrational state: the resulting frequency of scattered light goes up to $\upsilon_0 + \upsilon_m$. This Raman frequency is called Anti-Stokes frequency.

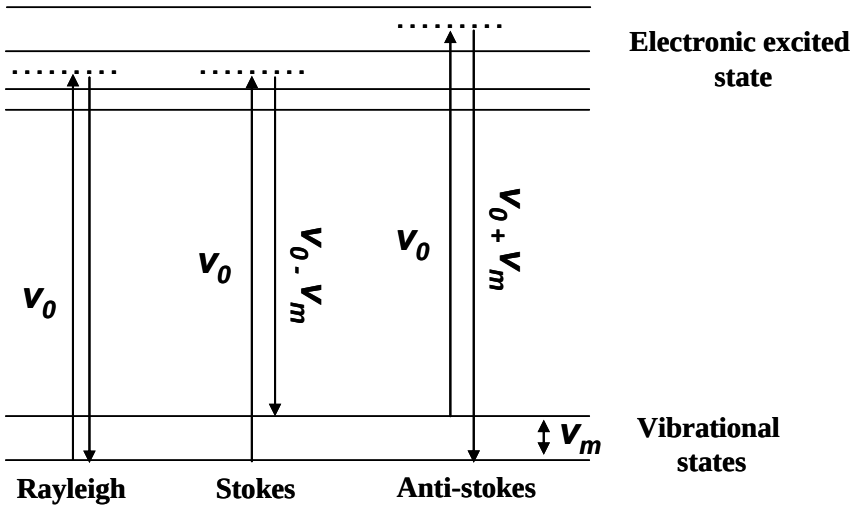

Figure II. 17 *Scheme of Raman principle*

A Raman system typically consists of four major components:

1. Excitation source (Laser).
2. Sample illumination system and light collection optics.
3. Wavelength selector (Spectrometer).
4. Detector (Photodiode array, CCD or PMT).

In our studies, Raman spectra were measured at room temperature using two spectrometers, both coupled with a nitrogen-cooled CCD camera: a Jobin-Yvon T64000 and a HR-visible Horiba Jobin Yvon. They have been used for studying the structural evolutions of our silica matrices. Raman spectrometry has also been used to confirm the existence and to estimate the size of CdS nanoparticles formed inside the silica matrices. The samples were illuminated with two laser sources operating in the visible range: an Argon ion laser (488 and 514.5 nm) and a Diode laser (475 and 532 nm). The Scattered light was collected with a lens and sent to a 3-gratings system in subtractive configuration.

II.4.3. Photoluminescence (PL)

Photoluminescence in solids is another process in which luminescence is stimulated by the interaction of photons with a material. Luminescence is defined as a phenomenon in which the

electronic state of a substance is excited by some kind of external energy (physical or chemical) and the de-excitation energy is given back as light [52]. It can be divided into two types, phosphorescence and fluorescence. Phosphorescence is a luminescence process whereby the light emission from a substance continues for a few seconds, minutes or hours after the exciting radiation has ceased, while fluorescence is a process in which emission decays with a much shorter life time (a few milliseconds or less). PL analysis is a non-destructive technique. The technique requires very few sample manipulations or environmental control. When light of sufficient energy illuminates a material, photons are absorbed and (electronic) excitations are created. These excitations relax and emit photons. The PL can be collected and analyzed to provide information about the photo-excited states. The PL spectrum reveals transition energies and the PL intensity gives a measurement of the relative rates of radiative and non-radiative recombinations. Variation of the PL intensity upon change of external parameters, e.g., temperature, excitation energy, power of excitation, can be used to further characterize electronic states and bands. In this study, we used the Micro PL spectroscopy to study the optical properties of the semiconductors NPs, such as CdS and PbS NPs, embedded inside dielectric matrices. The typical PL experimental set-up is illustrated in Figure II.18.

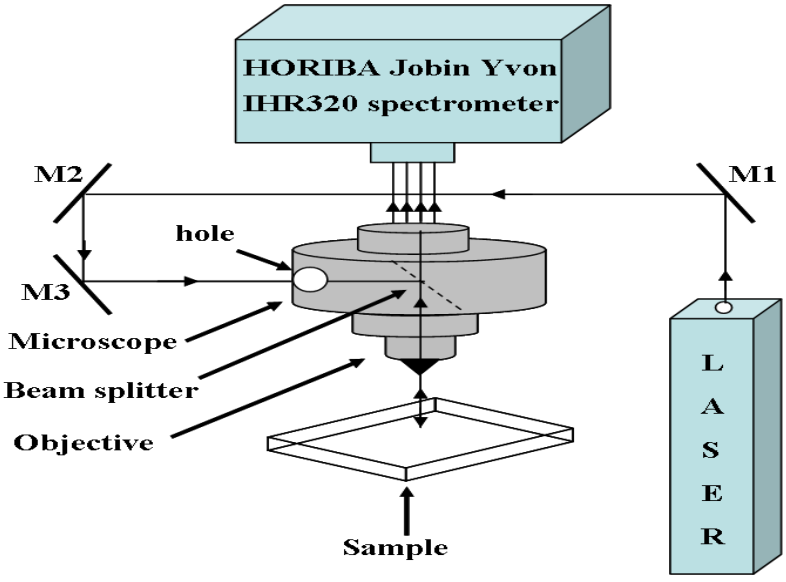

Figure II. 18 *Experimental setup of Micro PL spectroscopy (Photoluminescence) at ambient temperature: M1, M2 and M3 are mirrors.*

The samples were excited using an Argon or a Helium-Neon continuous-wave laser. Micro-photoluminescence measurements have been performed using a HORIBA Jobin Yvon IHR320 spectrometer coupled with a microscope at room temperature.

II.4.4. XRD and TEM measurements

X-ray diffraction (XRD) is a tool for the investigation of the fine structure of matter. By using x-rays of known wavelength λ and measuring the angle of diffraction θ, the spacing d of various planes in a crystal can be identifying. Transmission electron microscopy (TEM) is a tool that allows determining the elemental composition of a sample, its crystallography, the size and shape of NCs in a matrix with high spatial resolution. TEM images are formed using transmitted electrons, which can produce magnification up to 700,000 with a resolution better than 0.2 nm. The images can be resolved over a fluorescent screen, a photographic film or a high resolution CCD camera. Furthermore, the elemental analysis is possible by determining the energy of the X-rays produced by the interaction between the accelerated electrons with the sample. An electron gun, at the top of the microscope, emits the accelerated electrons that travel through vacuum in the column of the microscope. Instead of glass lenses focusing the light in an optical microscope, the TEM uses electromagnetic lenses to focus the electrons into a very thin beam which travels through the specimen to be analysed. Depending on the density of the material, some of the electrons are scattered, diffracted, absorbed and disappear from the beam. At the bottom of the microscope the unscattered electrons hit a fluorescent screen, which gives rise to a "shadow image" of the specimen with its different parts displayed in varied darkness according to their density. The image can be studied directly by the operator or photographed with a camera. Diffracted electrons can also be observed by changing the focusing plane. More details about these techniques are given elsewhere [53, 54].

In this thesis, the XRD and TEM have been used to characterise the semiconductor and metallic nanoparticles precipitated inside silica matrix prepared by the sol-gel route. The XRD patterns have been recorded on a Philips X'Pert diffractometer equipped with a monochromator, using Cu Kα radiation. The TEM analysis has been performed using three Microscopes: TOPCON EM002B operating at 200 KV, FEI Tecnai G2-20 twin with a 200 kV acceleration voltage, or Philips CM30 with a 300 kV voltage. Samples preparation for TEM analysis was achieved in two different ways. The first way consists of grinding the nanoparticle-doped silica into a powder and then depositing it onto a copper grid previously coated with a thin carbon membrane. In the second method, the sample had to be polished to a 25 µm thickness and then further thinned by using an ion-milling machine in order to get some nanometer-thick areas. After that, the thinned sample deposited onto a copper grid or a molybdenum grid. In both methods, the prepared samples were finally metallized with a vaporized carbon layer.

References

1. H. El Hamzaoui, L. Courthéoux, V.N. Nguyen, E. Berrier, A. Favre, L. Bigot, M. Bouazaoui, B. Capoen. Materials Chemistry and Physics. **121,** 83 (2010).
2. J.J. Ebelmen, C. R. Acad. Sci. **19,** 398 (1844).
3. M. Prassas, J. Phalippou and J. Zarzycki. Science of Ceramic Chemical Processing eds Wiley, 1986.
4. P. Yang, C.F. Song, M.K. Lu, X. Yin, G.J. Zhou, D. Xu, D.R. Yaun. Chem. Phys. Lett. **345,** 429 (2001).
5. M. Nogami, K. Nagasaka, and M. Takata. J. Non-Cryst. Solids. **122,** 101 (1990).
6. G.S. Li, D.Q. Zhang, J.C .Y u. Environ. Sci. Technol. **43,** 7079 (2009).
7. G. Ehrhart, B. Capoen, O. Robbe, Ph. Boy, S. Turrell, M. Bouazaoui. Thin Solid Films. **496,** 227 (2006).
8. N.N. Parvathy, G.M. Pajonkb and A. Venkateswa Rao. NanoStruc. Mater. **8**, 929 (1997).
9. N.N. Parvathy, A.V. Rao. Mater. Chem. Phys. **68**, 260 (2001).
10. N.N. Parvathy, G.M. Pajonk, A.V. Rao. J. Non-Cryst. Solids **241,** 79 (1998).
11. N.N. Parvathy, G.M. Pajonk, A.V. Rao. Mater. Res. Bull. **32,** 397 (1997).
12. B. Capoen, T. Gacoin, J.M. Nedelec, S. Turelle, M. Bouazaoui. J. Mater. Sci. **36,** 2565 (2001).
13. P.Y. Meng, Y. Xin, J.Z. Guang, X. Dong, R.Y. Duo. Chem. Phys. Lett. **354,** 429 (2001).
14. S. Besson, T. Gacoin, C. Ricolleau, C. Jacquiod, J-P. Boilot. Nano Lett. **2**, 409 (2002).
15. E. Rysiakiewicz-Pasek, M. Zalewska, J. Polanska. Opt. Mater. **30,** 777 (2008).
16. L. Chao, K.K. Yong, H. Jong. J. Non-Cryst. Solids. **355,** 1880 (2009).
17. M.F. Bertino, R.R. Gadipalli, J.G. Story and C.G. Williams. Phys. Lett. **85,** 6007 (2004).
18. K. Raulin, O. Cristini-Robbe, P. Baldeck, O. Stephan, C. Kinowski, S. Turrell, B. Capoen, M. Bouazaoui. J. Nanopart. Res. **12,** 1459 (2010).
19. K. Raulin, S. Turrell, B. Capoen, C. Kinowski, V. Tran, M. Bouazaoui. O. Cristini-Robbe. J. Raman Spectrosc. **42,** 1366 (2011).
20. T. Nobuhito, K. Yutaka, N. Yoshihiro, T. Shuhei. Opt. Expr. **12,** 4019 (2004).
21. L. Chao, K. Yong, H. Jong. J. Am. Ceram. Soc. **93,** 1221 (2010).
22. N. Romcevic, R. Kostic, M. Romevic. Phys. Status Solidi C **3,** 1295 (2006).
23. J. J. Shiang, S. H. Risbud, A. P. Alivisatos. J. Chern. Phys. **98,** 8432 (1993).
24. L. Bois, F. Chassagneux, Y. Battie, F. Bessueille, L. Mollet, S. Parola, N. Destouches, N. Toulhoat, N. Moncoffre. Langmuir. **26,** 1199 (2010).

25. A. Ashkarran, S. Aghigh, M. kavianipour, N.Farahani. Curr. Appl. Phys. **11** 1048 (2011).
26. Z. Konstantinović, M.G. Del Muro, M. Varela, X. Batlle A. Labarta. Nanotechnology **17,** 4106 (2006).
27. A.S. Nair, V. Suryanarayanan, T. Pradeep, J. Thomas, M. Anija, R. Philip. Mater. Sci. Eng. B **117,** 173 (2005).
28. L. Xiong, C. Weiping, B. Huijuan. J. Mater. Res. **17,** 5 (2002).
29. P. Anlian et *al*. Appl. Surf. Sci. **205,** 323 (2003).
30. V.S. Gurin, A.A. Alexeenko, S.A. Zolotovskaya, K.V. Yumashev. Mat. Sci. Eng. C. **26**, 952 (2006).
31. A.O. Yeshchenko, I.M. Dmitruk, A.M. Dmytrukb, A.A. Alexeenko. Mater. Sci. Eng. B. **137,** 247 (2007).
32. A.O. Yeshchenko, I.M. Dmitruk, A.M. Dmytrukb, A.A. Alexeenko, M.Y. Losytskyy, A.V.kotko and A.O. Pinchuk. Phy. Rev .B.**79,** 235438 (2009).
33. R. Sayah, L. Nadar, F. Vocanson, Y. Battie, S. Reynaud, R. Vera, A. Boukenter, N. Destouches. J. Non-Cryst. Solids **357,** 1342 (2011).
34. M.G. Ventura, A.J. Parola, A. Pires de Matos. J. Non-Cryst. Solids **357,** 1342 (2011).
35. J. Kimling, M. Maier, B. Okenve, V. Kotaidis, H. Ballot, A. Plech, J. Phys. Chem. B. **110,** 15700 (2006).
36. X. Hu, Q. Zhao, X. Jiang, C. Zhu, J. Qiu. Solid State Commun. **138,** 43 (2006).
37. S. Qu, Y. Zhang, H. Li, J. Qiu, C. Zhu. Opt. Mater. **28,** 259 (2006).
38. H. Zeng, J. Qiu, S.Yuan, Y.Yang, G. Chen. Ceram. Int. **34,** 605 (2008).
39. C.S. João, M.P. Coelho, A.Ruivo, A. Pires de Matos. Mater. Lett. **64,**705 (2010)
40. D. Mazzares. Manufacturing Multimode Fiber: Precise Control of Production and Testing Ensures High Performance. Fitel USA: 2003.
41. R. Ramsay. Photonic-crystal fiber characteristics benefit numerous applications. SPIE 2008.
42. B. Alfeeli, G, Pickrell. IEEE Phot. Tech. Lett. **21,** 1719 (2009).
43. E.F. Chillcce, R.E. Ramos-Gonzales, C.M.B. Cordeiro, L. Gutierrez-Rivera, H.L. Fragnito, C.H. de Brito-Cruz, A.C. Bordonalli, H.E. Hernández-Figueroa, R.L. Braga, L.C. Barbosa. J. Non Cryst. Solids **356,** 2397 (2010).
44. P.R. Watekar, S. Ju, A. Lin, M.J. Kim, B.H. Lee, W. Han. J. Non-Cryst. Solids **356,** 2384 (2010).
45. S. Ju, P.R. Watekar, C.J. Kim, W. Han J. Non-Cryst. Solids **356,** 2273 (2010).
46. A.A. Correa, J. yang, C.E. Finlayson, A.C. Peacock, J. R. Hayes, P.J. Sazio, J.J. Baumberg S.M. Howdle. Adv. Funct. Mater. **17,** 2024 (2007).

47. A. Dhawan and J. Muth. Nanotechnology **17,** 2504 (2006).
48. S. Ju, V. Nguyen, P. Watekar, B. Kim, C. Jeong, S. Boo, C. Kim, W. Han. J. Nanosc. Nanotechnol.**6,** 3555 (2006).
49. S. Brunauer, P.H. Emmett and E. Teller. J.Am. Chem. Soc.**60,** 309 (1938).
50. E.P. Barrett, L.G. Joyner and P.P. Halenda. J. Am. Chem. Soc. **73,** 373 (1951).
51. K.S. Sing, D.H. Everett, R.W. Haul, L. Moscou, R.A. Pierotti, J. Rouquerol and T. Siemieniewska. Pure Appl. Chem.**57,** 603 (1985).
52. S. Shionoya, W.M.Yen. Phosphor Handbook, Phosphor Research Society. CRC press, 1999.
53. B. D. Cullity. Elements of X-Ray Diffraction. Addison-Wesley Publishing Company, 1978.
54. S. Amelinckx, D.V. Dyck, J.V. Landuyt, G.V. Tendeloo. Electron Microscopy: Principles and Fundamentals. Wiley, 1997.

Chapter III: Growth of CdS and PbS Nanoparticles inside Silica Xerogels

The porous silica matrix not only acts as a mechanical skeleton of a composite material, but also renders an essential influence on the fundamental properties of incorporated substances. Therefore, the matrix has to satisfy several requirements: high transparency, chemical inertia, mechanical strength, porosity with a well-defined pore size distribution, presence of active centers ensuring the effective immobilization of doping components and substantially influencing their physico-chemical properties [1]. So the aim of this porous matrix is to confine active elements within the pores by impregnation with appropriate solutions. Sulphide semiconductors CdS and PbS are inorganic compounds with bulk band gap energies of 2.42 eV (a_B = 5.8 nm) [2, 3] and 0.41 eV (a_B =18 nm) [3], respectively.

In this chapter, we report on two methods for the fabrication of CdS and PbS nanoparticles inside the silica xerogels. The first method is based on the laser irradiation and allows to localize the growth of CdS or PbS nanoparticles inside a transparent porous sol-gel-derived silica matrix. The localization of the nanoparticles inside the volume of the matrices has been achieved using the pulsed femtosecond laser. On the other hand, a space-selective growth of CdS nanoparticles on the surface of the silica xerogel has been achieved using the visible continuous laser. The second method, based on a heat-treatment, has been carried out in order to compare and to understand the mechanism of formation of CdS and PbS nanoparticles. In the first section of this chapter, we present the synthesis and characterization of CdS nanoparticles precipitated in the matrix by different methods. Herein, the influences of the laser power, concentration and heating temperature on the optical response of the CdS nanoparticles are also presented. Similarly, the precipitation of the PbS nanoparticles inside the silica xerogel is presented in section 2.

III.1. Growth of CdS nanoparticles inside a porous silica matrix

III.1.1. Experimental preparation

Porous silica samples with a thickness of 2 mm, prepared as described in chapter II, were soaked for 4 hours in one of the aqueous solutions of various concentrations, denoted S1, S2, S3 and S4. The post-doping solutions were composed of cadmium acetate (Aldrich) as a precursor of cadmium, thiourea (Aldrich) as a precursor of sulphur and a mixture of water and ethanol as a solvent. The molar concentrations of the solutions (S1 to S4) were respectively 0.56, 0.37, 0.28 and 0.06 mol.L^{-1}. The molar ratio between thiourea and cadmium acetate was kept to 1. Then, the samples were taken out from the solutions and dried at 50°C for 1 hour to eliminate solvents, the precursors being retained within the pores.

The irradiations of the doped samples were performed using two lasers: pulsed femtosecond and visible continuous lasers. The average powers of the femtosecond laser that have been used to irradiate the samples were: 60, 40 and 25 mW. It is interesting to calculate the relevant parameters corresponding to these average powers, so the peak power density (I_D), the peak energy density (E_D) and the deposited energy density (E) have been calculated for each irradiation power using Eq.(III.1), Eq.(III.2) and Eq.(III.3):

$$I_D = \frac{P_m}{f * S * t} \qquad \textbf{Eq.(III.1)}$$

$$E_D = I_D * t \qquad \textbf{Eq.(III.2)}$$

where P_m is the incident average power, f is the pulse repetition rate (1 KHz), t is the pulse duration (120 fs) and S is the surface area of the laser spot at the focus point. The deposited energy density is estimated to:

$$E = \frac{P_m}{d * v} \qquad \textbf{Eq.(III.3)}$$

where d is the diameter of focus laser beam and v is the scanning speed. The obtained spot, of a diameter estimated to 2 μm, was located inside the volume of the silica matrix and scanned laterally at a rate of 1 mm/s. Table III.1 shows the estimated peak power densities, peak energy densities and the deposited energy densities from the above equations.

Average power (mW)	Peak power density ($W.cm^{-2}$)	Peak energy density ($J.cm^{-2}$)	Deposited energy density ($J.cm^{-2}$)
10	**2.6×10^{15}**	**318**	**500**
25	**6.6×10^{15}**	**792**	**1250**
40	**10.6×10^{15}**	**1272**	**2000**
60	**15.9×10^{15}**	**1908**	**3000**

Table III. 1 *Calculated values of the peak power density, the energy density and the deposited energy density at each femtosecond irradiation power.*

A tight network of parallel irradiated lines has been performed inside the volume of the silica matrix, with a spacing of 20 μm, in order to cover a wide zone with photo-precipitated materials, able to be observed with the eye and to be characterized.

The visible irradiation was achieved using the Argon laser line 514.5 nm on the surface of the doped silica xerogels. The average powers used to irradiate the doped samples were 35, 50, 70, 105 and 140 mW. Table III.2 shows the estimated power densities ($I_D = {P_m}/{S}$ $P_D = {P_m}/{S}$) and the deposited energy densities ($E = {P_m}/{d * v}$ $E_c = {P_m}/{d * v}$) for each visible irradiation power. (Note: Herein we have d = 10µm and v = 1 mm/s).

Average power (mW)	Power density ($W.cm^{-2}$)	Deposited energy density ($J.cm^{-2}$)
35	**4.4×10^4**	**350**
50	**6.3×10^4**	**500**
70	**8.8×10^4**	**700**
105	**13.2×10^4**	**1050**
140	**17.6×10^4**	**1400**

Table III. 2 *Calculated values of the power density and the deposited energy density for each visible irradiation power.*

In parallel, doped silica xerogels were submitted to heat-treatments at different temperatures. The threshold temperature to precipitate the CdS nanoparticles is about 100°C.

III.1.2. Growth of CdS nanoparticles by pulsed femtosecond irradiation

Xerogels doped with CdS precursors present no optical absorption at a wavelength of 800 nm because the excitation energy is much smaller than the band gap of silica, so that no linear absorption occurs when the matrix is irradiated. Consequently, the laser beam is allowed to penetrate deeply inside the material. However, at this wavelength and for sufficient laser peak power, a multi-photon absorption occurs. As a result, the impact area is highly localized within the volume of the focal area. Visually, the undoped silica xerogel, taken as the blank, remains unchanged and transparent when exposed to a pulsed femtosecond irradiation. On the other hand, the doped xerogels with CdS precursors become yellow in the irradiated area, as can be seen in Figure III.1. This sample doped with a CdS precursor solution concentrated at 0.56 mol.L^{-1} has been irradiated with an incident beam of diameter 2 μm and average power 60 mW. (Note: the yellow color becomes deeper with increasing the laser power).

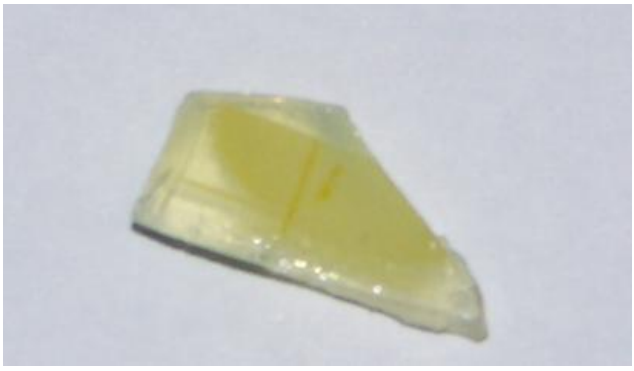

Figure III. 1 *Yellow color observed in the irradiated area (60 mW of pulsed femtosecond laser)*

To confirm the formation of CdS nanoparticles, Raman micro-spectrometry has been performed on the irradiated area, on the non-irradiated area and on the pure silica xerogel. The Raman spectra were obtained under the following conditions: 473 nm as excitation wavelength, laser power of 7 mW at the focus point (the incident power was kept low enough to avoid any further precipitation of CdS nanoparticles) and acquisition time of 3 seconds. In effect, the 473 nm excitation wavelength makes it possible to observe the Raman spectra of the CdS nanoparticles under resonance conditions. Typical spectra are shown in Figure III.2.

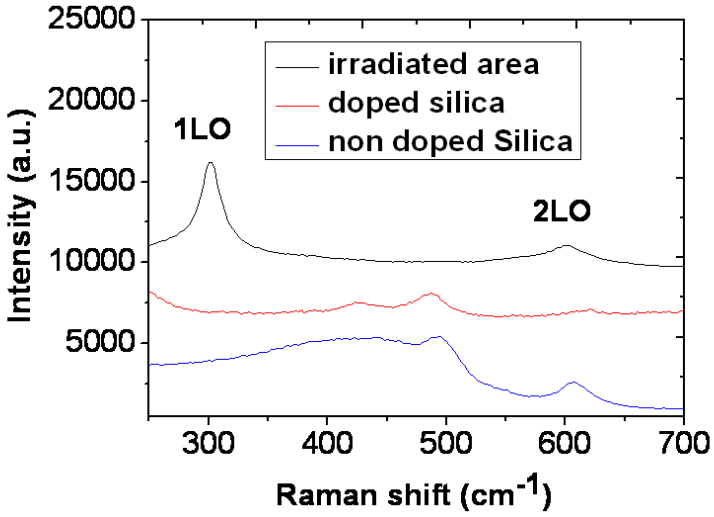

Figure III. 2 *Raman spectra of a CdS precursor-doped silica matrix: (black) femtosecond irradiated area at 60 mW, (red) non-irradiated area and (blue) pure porous silica.*

In the irradiated zone of the doped sample, the spectrum of silica is replaced by two strong bands around 300 and 600 cm^{-1}, which can be attributed to the fundamental longitudinal optical phonon (1LO) and its first overtone (2LO) in CdS crystals [4]. The ratio of the Raman bands maxima intensities I_{2LO}/I_{1LO} is around 0.25 and, according to Shiang *et al* [4], the corresponding nanocrystal diameter can be estimated to 2-3 nm.

III.1.2.1. Influence of the femtosecond laser power on the size of CdS nanoparticles

Three different laser average powers have been used: 25, 40 and 60 mW to irradiate silica xerogels doped with a solution S1 of CdS precursor concentration 0.56 $mol.L^{-1}$. After each of these treatments, Raman measurements were performed in the irradiated areas using two excitation wavelengths: 532 nm and 473 nm. During the Raman experiments, the laser power was kept to 7 mW for both excitation wavelengths and the acquisition time was 3 second. Figure III.3 shows the comparison of the Raman spectra recorded, using both excitation wavelengths, on the sample irradiated with incident average power of 40 mW.

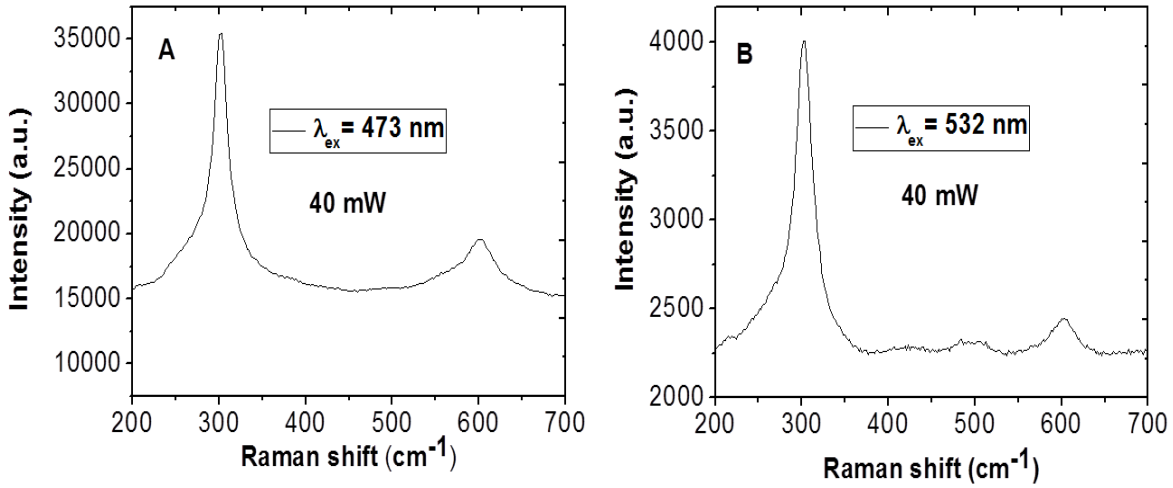

Figure III. 3 *Raman spectra of the irradiated area at 40 mW: A, excitation wavelength is 473nm. B, excitation wavelength is 532nm.*

The obtained signal under excitation at 473 nm is more intense than under excitation at 532 nm, due to the relative vicinity of the absorption edge and thus to the resonance conditions. The ratio of the Raman bands maxima intensities I_{2LO}/I_{1LO} has been calculated for each irradiation power, and is summarised in Table III.3. The ratio I_{2LO}/I_{1LO} is found to be around 0.2 for excitation at 473 nm, corresponding to a particle diameter of 2 or 3 nm regardless of the femtosecond power used (see Chapter II, Figure II.18). On the other hand, this ratio is equal to only 0.12 for excitation at 532 nm, corresponding to a particle size of around 1 nm.

Average power (mW)	**I_{2LO}/I_{1LO} (λ_{ex}= 473 nm)**	**I_{2LO}/I_{1LO} (λ_{ex}= 532 nm)**
25	**0.21**	**0.11**
40	**0.19**	**0.12**
60	**0.20**	**0.12**

Table III. 3 *Intensity ratio of 2LO and 1LO at different excitation wavelengths versus concentration ratio.*

This latter result cannot be explained by the resonance Raman excitation, nor by a wavelength size-selection. However, the values estimated from the excitation at 473 nm are more accurate because this wavelength is close to the Raman resonance conditions. Thus, using Raman spectroscopy, the effect of the irradiation power on the CdS nanoparticles diameter is still unclear and different characterisation techniques should be performed to study this influence.

Optical UV-visible absorption and photoluminescence measurements have been recorded from the irradiated areas. Figure III.4 reports the absorbance spectra of the samples irradiated with incident average powers of 25, 40 and 60 mW.

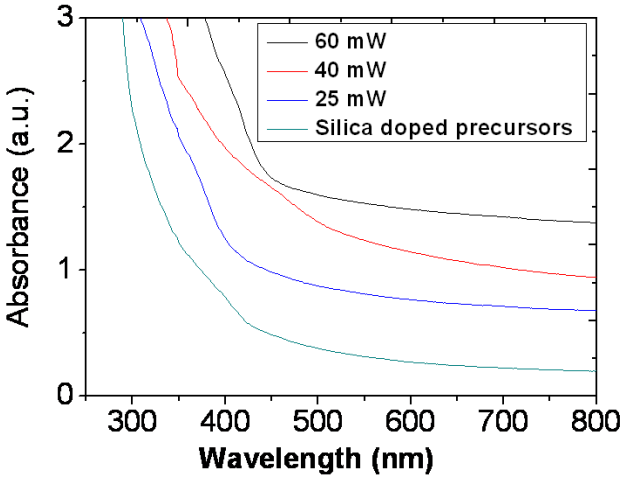

Figure III. 4 *Optical absorbance spectra of CdS-doped silica matrices (solution S1) irradiated with different incident powers of the femtosecond laser.*

After irradiation, the absorption spectra of the irradiated areas are red-shifted with respect to the absorption spectrum of the non-irradiated zone and the absorbance values in the irradiated areas are higher than the one in the non-irradiated zone. Both phenomena could be attributed to the formation of CdS nanoparticles: the red-shift of the absorption edge corresponds to the particle growth under increasing laser power, while the apparent absorbance baseline increase is mainly due to light scattering from silica defects induced by laser irradiations. The absence of clear excitonic absorption structures for the irradiated samples may be explained by the large size distribution of the nanocrystallites. To extract the direct band gap energy E_g from these absorption data, the curves in Figure III.5 have been extrapolated using the Mott equation [5]:

$$A.h\upsilon = K.(h\upsilon - Eg)^{1/2} \qquad \textbf{Eq.(III.4)}$$

where A is the absorbance, $h\upsilon$ is the photon energy and K is a constant. The band gap energies are estimated to 3.2, 2.75 and 2.62 eV for incident powers 25, 40 and 60 mW respectively. These values are slightly higher than the bulk band gap of CdS (2.43 eV), which means that the quantum confinement regime is intermediate.

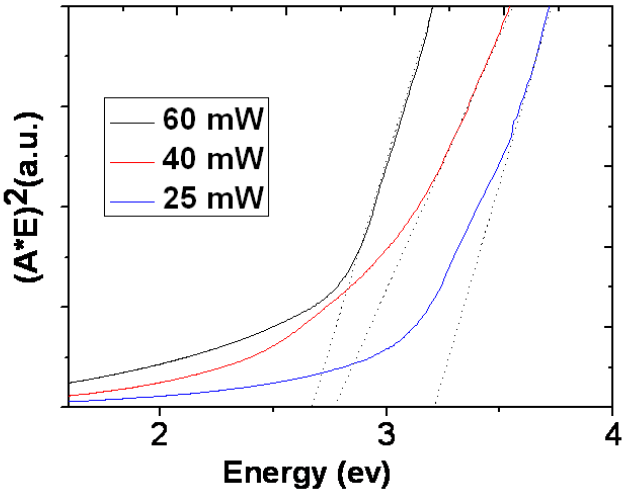

Figure III. 5 *Fitted absorption data by using Mott equation as a function of the femtosecond laser power*

Using the tight-binding model [6] presented in chapter I, the diameter size of the CdS nanoparticles was estimated to 2, 4 and 5 nm for the incident powers 25, 40 and 60 mW respectively. Therefore, the diameter size of the formed CdS increased as expected with the incident laser power. To confirm the obtained results, PL spectra were recorded in the same irradiated areas. Figure III.6 shows the emission spectra of the same samples under excitation wavelength 364 nm.

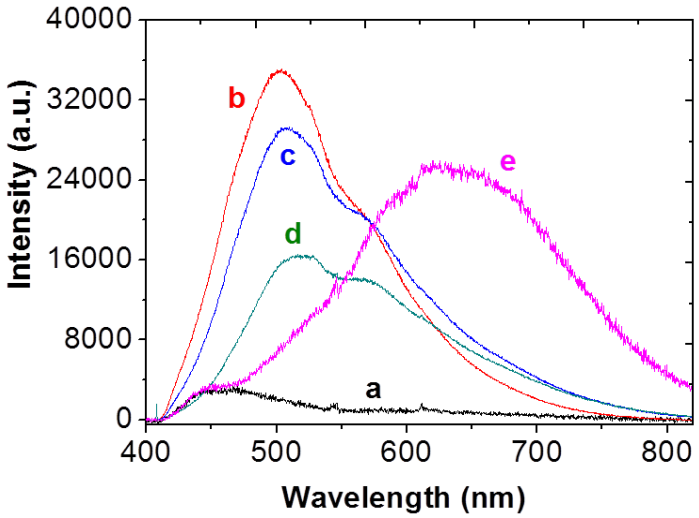

Figure III. 6 *Emission spectra of: (a) non-doped silica xerogel, (b)xerogel doped with CdS precursors, (c) irradiated area with 25 mW, (d)40 mW and (e)60 mW.*

The PL spectrum of pure silica xerogel shows an emission bands with weak intensity centered around 450 nm, and it was plotted in Figure III.6 for comparison. The doping with CdS precursors leads to the appearance of two emission bands centered around 500 nm and 565 nm,

which are similar to those obtained from the irradiated areas with 25 and 40 mW. This could be explained by the weak concentration of the formed CdS nanoparticles as compared to the high concentration of CdS precursors remaining in the silica network after the femtosecond irradiation. The irradiation with 60 mW leads to a strong decrease in the emission bands attributed to the CdS precursors, together with the appearance of large emission bands centred around 650 nm. This strong broad emission in the range 450-800 nm is attributed to recombination of trapped charge carriers at surface defects. The surface states in CdS could be due either to sulphur vacancies or cadmium vacancies depending on the availability of the cations or anions. The passivation or encapsulation of CdS naoparticles could lead to an enhancement of these nanoparticles emission [7-9].

III.1.2.2. Formation mechanism of CdS nanoparticles under femtosecond laser irradiation

In the literature, the mechanisms of CdS nanoparticles formation inside a porous silica matrix have been explained by pyrolysis and decomposition of the CdS precursors under heat-treatment [10]. In our case, the nano-crystallization of CdS inside the porous silica occurred in the region of the laser irradiation without any further annealing because of two main processes. Firstly, the multi-photon absorption of the porous silica matrix and of the CdS precursors at 800 nm [11] leads to the decomposition of these precursors, thus enriching the irradiated zone with cadmium and sulfur ions. In the same time, the temperature elevation during the laser pulse could be sufficient to aggregate the molecular CdS into nanoparticles [12, 13].

In order to know whether or not thermal effects can play a role in the formation of the nanoparticles, a rough calculation allows evaluating the temperature rise in the irradiated zone of the impregnated samples during the irradiation. First of all, the material is essentially made of porous silica with a density of ρ = 1.06 g.cm^{-3}. This value has been calculated from the following Eq.(III.5):

$$\rho = \frac{\rho_{SiO_2}}{(1+\rho_{SiO_2} * V_p)} \qquad \textbf{Eq.(III.5)}$$

Where ρ_{SiO_2} is the density of the dense vitreous silica, equal to 2.2, and V_p (0.49 cm^3/g) is the porous volume of the considered sample.

The typical time required for thermal conduction effects to become significant and for the generated heat to be dissipated in the sample, is defined [14] as:

$$t_c = \frac{w_0^2 \rho C_p}{4\kappa} \qquad \textbf{Eq.(III.6)}$$

where w_0 (1µm) is the beam waist radius, C_p (0.703 J/g.K) and κ (0.6 W/m.K) are respectively the specific heat and thermal conductivity of silica. This time t_c, estimated to be 310 ns in our samples, is much less than the duration between two pulses (1 ms), so that no cumulative thermal effect is assumed to occur.

On the other hand, the local and instantaneous temperature rise, produced by a laser pulse of different incident energy, has been evaluated by considering only the weak linear absorption due to the matrix and to the precursor. An effective volume of the beam waist has been determined around 11.9 µm^3 through the equation:

$$V_e = \frac{2\pi w_0^2 z_0 \rho}{\rho_{SiO_2}} \qquad \textbf{Eq.(III.7)}$$

where z_0 is the Rayleigh range, namely the distance along the propagation direction of a beam from the waist to the place where the area cross-section is doubled. For a Gaussian beam, the Rayleigh length is given by:

$z_0 = \frac{\pi w_0^2}{\lambda}$	**Eq.(III.8)**

The instantaneous temperature rise is roughly given by:

$$\Delta T = \frac{E_{abs}}{C_V V_e} \qquad \textbf{Eq.(III.9)}$$

with (C_V =1.547 J/cm^3.K) the volumetric heat capacity of silica and E_{abs} the absorbed energy in the volume V_e, given as:

$$E_{abs} = E_{w_0}(1 - e^{-2\alpha z_0}) \qquad \textbf{Eq.(III.10)}$$

where $E_{w_0} = E_{pulse} e^{-\alpha L/2}$ is the pulse energy arriving at the waist, α the linear absorption coefficient and L (2 mm) the thickness of the sample. The absorption coefficient was 2.3 cm^{-1} before any irradiation. Table III.4 shows the estimated energy and the temperature rise from the above equations. These temperatures are considered as instantaneous, the excessive heat being

evacuated in a few microseconds. They are probably underestimated due to nonlinear absorption effects not taken into account. Anyway, such high temperatures are fully sufficient to create locally the CdS nanoparticles inside the porous silica xerogels.

Power (mW)	Ew_0 (µJ)	E_{abs} (nJ)	ΔT (k)
60	**47**	**86**	**4675**
40	**31**	**56**	**3044**
25	**19.86**	**35**	**1902**
10	**7.9**	**14**	**761**

Table III. 4 *Temperature rise calculated using Eq.(III.9) as a function of the incident power of the laser femtosecond.*

III.1.3. Growth of CdS nanoparticles by visible continuous irradiation

Transparent silica matrices, previously impregnated with a CdS precursors solution of concentrations C varying between 0.06 and 0.56 mol.L^{-1} , have been irradiated by a visible continuous beam at 514.5 nm, with incident powers P_m varying from 50 to 140 mW. For example with C = 0.56 mol.L^{-1} and P_m = 70 mW, this leads to the formation of a yellow area under and on the surface of the sample (Figure III.7). The power threshold for the appearance of this colouring was determined around 20 mW corresponding to a deposited energy 200 J.cm^{-2}, irrespective of the concentration of the loading solution.

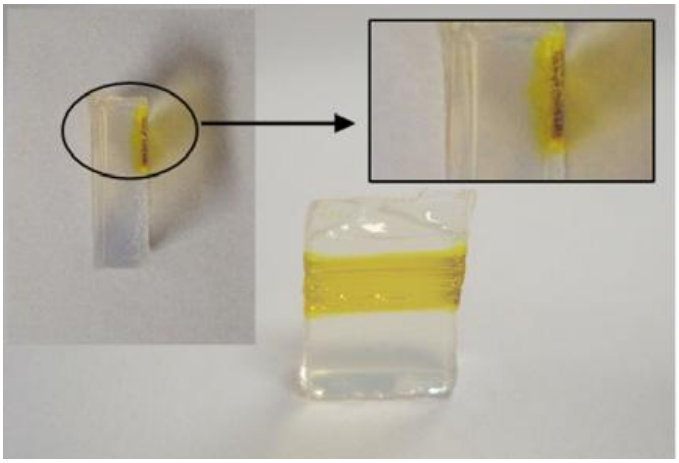

Figure III. 7 *Photograph image of a xerogel doped with CdS after irradiation at 514.5 nm.*

To confirm that the appearing yellow colour corresponds to the CdS nanoparticles growth, high resolution transmission electron microscopy analysis (HR-TEM) was performed on the irradiated sample. To that purpose, the yellow areas have been scratched, grinded into powders and deposited onto copper grids covered by a thin carbon membrane. Figure III.8 presents a HR-TEM image of a single particle exhibiting a fringe spacing of 0.312 nm, which is in good agreement with the distance between the (101) lattice planes of hexagonal CdS [15].

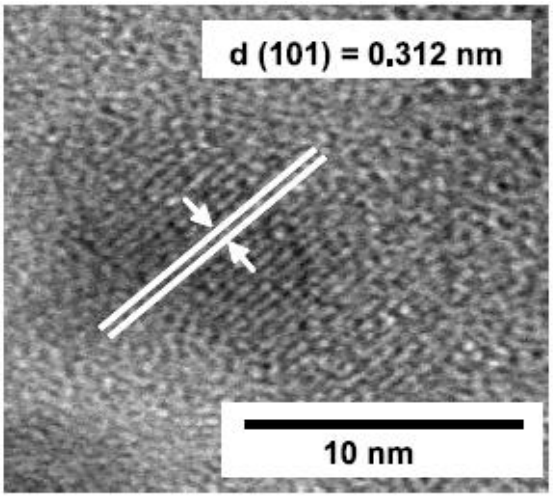

Figure III. 8 *HR-TEM image of a CdS precursor-doped silica sample (0.56 mol.L^{-1}) after a continuous laser irradiation with P_m = 70 mW.*

III.1.3.1. Influence of the concentration on the size of CdS nanoparticles

Silica xerogel samples were immersed into 4 solutions with different concentrations (0.56, 0.37, 0.28 and 0.06 mol.L^{-1}) before being irradiated with an incident power of 70 mW. Micro-Raman measurements were subsequently performed in the irradiated areas using an excitation wavelength of 514.5 nm (Figure III.9). The laser power at the focus point was kept below the power threshold necessary to form nanoparticles. The acquisition time was kept to 300 seconds. The spectra all exhibit two narrow bands peaking at 300 and 600 cm^{-1}, respectively ascribed to the first longitudinal optical mode (1LO) and its overtone (2LO). The ratio of the Raman bands maxima intensities I_{2LO}/I_{1LO} remains around 0.25 for all the irradiated samples. According to Shiang *et al* [4], the corresponding nanocrystal diameter can be estimated around 1 or 2 nm. This would mean that there is no influence of the concentration on the size of the CdS nanocrystal.

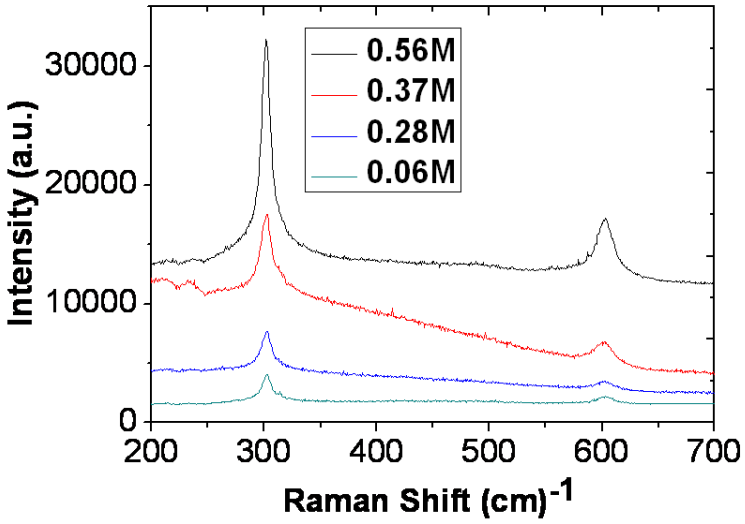

Figure III. 9 *Raman spectra of the irradiated areas as a function of the solution concentration.*

Conversely, the characterisations using optical absorption and XRD show a size dependence on the impregnated concentrations. Figure III.10 shows the optical absorption spectra of the irradiated areas samples doped with different concentrations of CdS precursors.

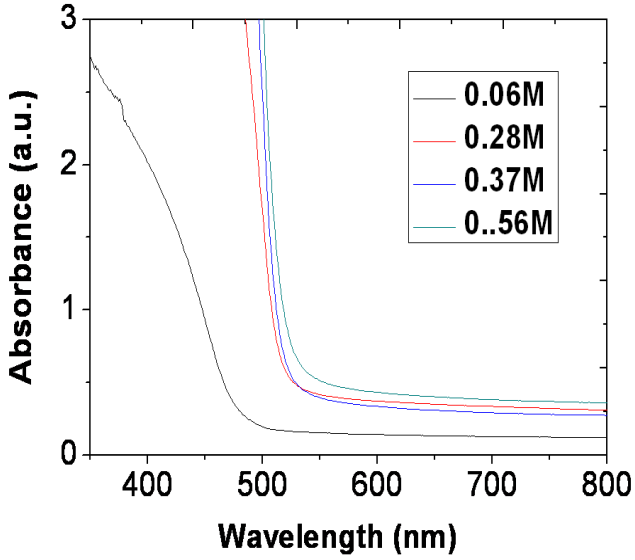

Figure III. 10 *Optical absorbance spectra of CdS precursor-doped silica matrices irradiated by the 514.5 nm continuous laser for a mean power of 70mW and for different solution concentrations.*

As a result of the growth of bigger particles, the absorption threshold shifts towards higher wavelengths with increasing concentration from 0.06 mol.L^{-1} to 0.56 mol.L^{-1}. For the concentrations greater than 0.28 mol.L^{-1}, this red-shift of the absorption edge, associated with the quantum confinement, is weaker, which could be explained by the presence of CdS

nanoparticles with diameters larger than 5 nm.The band gap energies of CdS nanoparticles, estimated using equation (III.4), are summarized in Table III.5. The mean diameters of the CdS nanoparticles, deduced from these gap energies using a tight-binding model correlation curve [6] (Chapter I, section I.1.4), were listed also in Table III.5. Table III.5 reports the increase of the so-estimated sizes of CdS nanoparticles as a function of the solution concentration.

Concentration (mol.L^{-1})	**Band gap energy (eV)**	**Diameter of CdS (nm) ±1 nm**
0.56	**2.50**	**6**
0.37	**2.52**	**6**
0.28	**2.60**	**4.5**
0.06	**2.80**	**3**

Table III. 5 *Estimated sizes of CdS nanoparticles created by a continuous visible laser irradiation at 70 mW as a function of the impregnation solution concentration.*

XRD measurements have been also carried out in order to have a better idea of the crystal structure and of the particle size (Figure III.11).

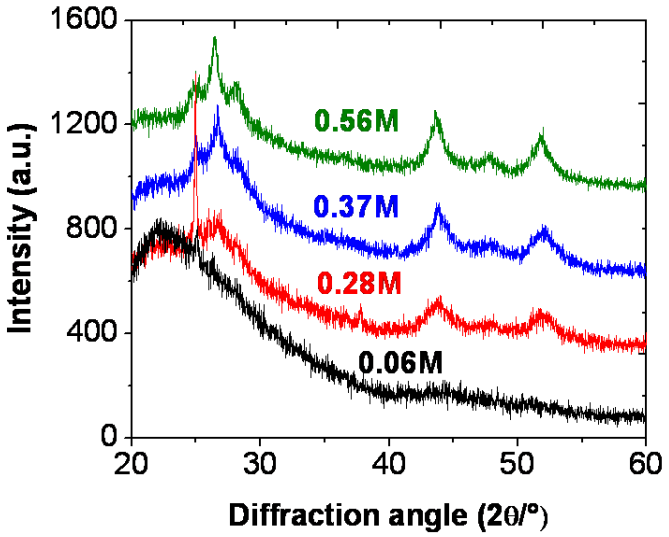

Figure III. 11 *XRD patterns of the CdS nanoparticles created by continuous laser irradiation (514.5 nm and 70 mW) as a function of 4 different concentrations: 0.56 mol.L^{-1}, 0.37 mol.L^{-1}, 0.28 mol.L^{-1} and 0.06 mol.L^{-1}.*

The peaks at 25°, 26.4°, 28.3°, 43.6°, 47.8° and 51.8° observed in the XRD pattern of the irradiated area are attributed to reflexions on crystal planes families (100), (002), (101), (110), (103) and (200), respectively. All of theses reflexes correspond to the hexagonal phase of CdS

[17], which is in a good agreement with the TEM measurements. Furthermore, there is an increase in intensity and a decrease in the width of the peaks with increasing the concentration ratio.The mean nanocrystal diameters *d* have been determined from the line-widths (110) of the XRD patterns using the well-known Scherrer formula [18].

Eq.(III.11)

$$d = (0.94\lambda)/(B\cos\theta_B)$$

where λ is the x-ray wavelength, B is the full width at half maximum of the diffraction reflex (in radian), and θ_B is the half-angle position of the diffraction reflex on the 2θ scale. The calculated diameters of the CdS nanoparticle are shown in Table III.6.

Concentration (mol.L^{-1})	**Diameter (nm) ±1 nm**
0.56	**8**
0.37	**6**
0.28	**4**

Table III. 6 *CdS NPs diameters calculated from XRD measurements for different impregnation concentrations.*

It is clear that the tendency of size increase with the concentration confirms the results obtained from the optical absorption. The difference in the values of the calculated diameters determined using absorption and XRD could be attributed to the absence of an exciton peak in the absorption spectra, so that the position of the absorption edge was performed with a weak precision. Other error sources are the models used to link the size to the band gap energy in absorption experiments and to the reflex peak width in XRD measurements.

III.3.2. Influence of continuous laser power on the size of CdS nanoparticles

Silica xerogels loaded with the solution concentrated at 0.56 mol.L^{-1} have been irradiated at different incident powers: 50, 70, 105 and 140 mW. Figure III.12 shows the optical absorption spectra recorded in the irradiated areas. As the incident power is decreased from 140 to 50 mW, the observed slight blue-shift means that the nanocrystals become smaller.

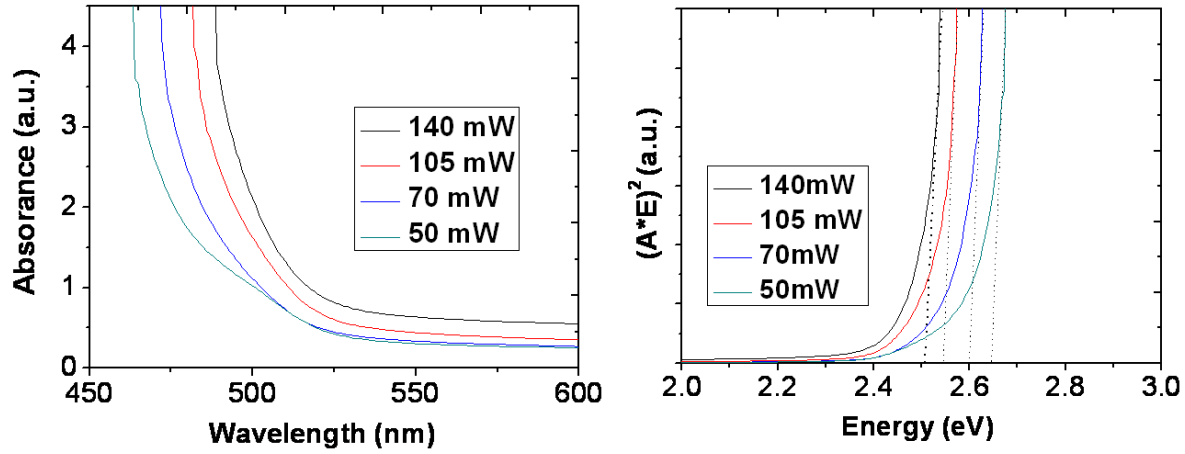

Figure III. 12 *Left: optical absorption of silica matrices impregnated with CdS precursors solution (0.37 mol.L^{-1}) and then irradiated with different incident powers: 140 mW, 105 mW, 70 mW and 50 mW. Right: Fitted absorption data using Mott equation as a function of the visible laser power*

Table III.7 shows the values of the band gap energies estimated using Eq. (III.4) (Figure III.12 (right)) and of the CdS particle diameters estimated using tight-binding model. As shown in Table III.7, the diameters increase with increasing the incident laser power. This corresponds to an increasing temperature generated by the continuous laser irradiation. Indeed, in the case of a continuous laser irradiation, a direct photo-thermal mechanism is likely at the origin of the laser-induced crystallization of CdS in hexagonal phase.

Average power (mW)	**Band gap energy (eV)**	**Diameter of CdS (nm) ±1 nm**
140	**2.50**	**6**
105	**2.55**	**5**
70	**2.60**	**4.5**
50	**2.65**	**4**

Table III. 7 *Calculated values of the nanoparticle sizes estimated from absorption measurements as a function of laser incident power.*

Trying to make clear the mechanism of formation of these nanoparticles and to compare it with a classical temperature-induced crystal growth, the next section reports the heat-treatment performed on samples doped by CdS precursors in the same conditions.

III.1.4. Growth of CdS nanoparticles by heat-treatment

A xerogel doped by impregnation with a solution of concentration 0.56 mol.L^{-1} was annealed at 120°C. The color of the sample changed from transparent to deep yellow after 92 hours, as shown in Figure III.13 (a).

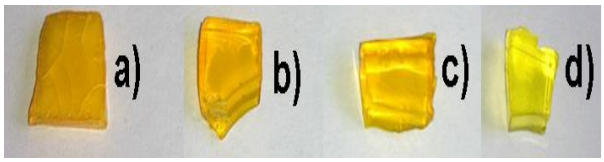

Figure III. 13 *Photograph images of CdS nanoparticles-doped silica xerogels heated at 120°C for 92h after impregnation with different concentrations (a) 0.56 mol.L^{-1}, (b) 0.37 mol.L^{-1}, (c) 0.28 mol.$L^{-1}$and (d) 0.06 mol.L^{-1}.*

To confirm that the yellow color corresponds to the presence of CdS particles, HR-TEM analyses have been performed on the most concentrated sample (Figure III.14). The inter-planar distance was estimated around 0.20 nm, which is attributed to the (220) lattice planes of the cubic CdS phase [19].

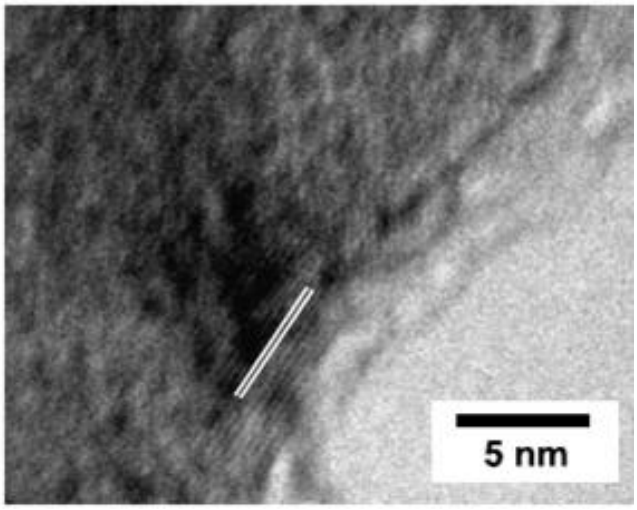

Figure III. 14 *HR-TEM image of a CdS precursor-doped silica matrix (0.56 mol.L^{-1}) after a heat treatment at 120°C for 92 h.*

The mechanism of formation of CdS nanoparticles is easily explained by the pyrolysis and decomposition of the cadmium acetate and of the thiourea molecule at 120°C that liberate Cd^{2+} and S^{2-} ions, respectively, in the matrix. These ions can move through the pores of the matrix and quickly recombine each other to form CdS molecules. The structural cubic phase of CdS has been explained by Bandaranayake *et al.* [17] as a result of the low temperature growth process (less than 300°C). Hexagonal wurtzite structure is usually considered as the equilibrium phase

of CdS, which contradicts the present result. It is sometimes considered that the metastable cubic phase is caused by a rapid nucleation and growth. However, this theory must be ruled out since in the present case, the growth kinetics is more rapid in the case of laser irradiation, for which hexagonal structure has been clearly identified. Hence, it is believed that the cubic structure is the equilibrium phase for CdS very small particles with a free surface [17, 20, 21]. Hence, such a cubic phase reveals the formation of particles of diameter less than 15 nm in the pores of the xerogel. On the contrary, when irradiated with a laser beam, the reaction mechanisms are so rapid that the CdS particles remain in the silica, or are at least intimately linked to the matrix, thus having different surface effects.

III.1.4.1. Influence of precursors concentration on the size of CdS nanoparticles

Four samples with different concentrations (0.56, 0.37, 0.28 and 0.06 mol.L^{-1}) were put simultaneously inside a furnace at 120°C for 92h. As already shown in Figure III.13, the colors of the samples become deeper from yellow to orange as the impregnation concentration increases. This suggests the formation of bigger particles with the increase in concentration. Optical absorption measurements have been performed on the heated samples as shown in Figure III.15.

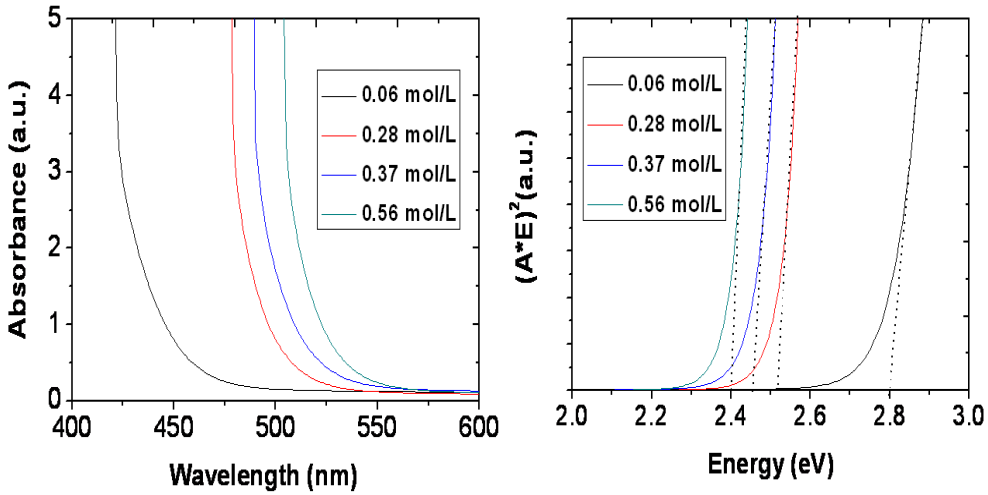

Figure III. 15 *Left: optical absorbance spectra of CdS precursor-doped silica matrices heated at 120°C for 92h.Right: Fitted absorption data using Mott equation as a function of different concentrations.*

Blue-shifts, assigned to confinement effect in smaller particles, have been observed with decreasing the concentration. The size of the CdS nanoparticles at different concentrations have

been calculated using Eq. (III.4) and the tight-binding model after representing $(A^*E)^2$ versus $h\nu$. The results are shown in Table III.8.

Concentration ($mol.L^{-1}$)	Band gap energy (eV)	Diameter of CdS (nm) ±1 nm
0.56	**2.45**	**6**
0.37	**2.55**	**5.5**
0.28	**2.60**	**4.5**
0.06	**2.90**	**3**

Table III. 8 *Band gap energy, absorption threshold wavelength and diameters of CdS NPs created by heat-treatment at 120°C for 92h and for different impregnation concentrations.*

Despite the different crystal structures, the nanoparticle diameter behaviour with concentration is similar to the one observed under continuous laser irradiation.

Micro-PL emission spectra have been recorded on the same samples, as shown in Figure III.16. The excitation incident laser beam had a wavelength of 364 nm and a mean power of 7 mW.

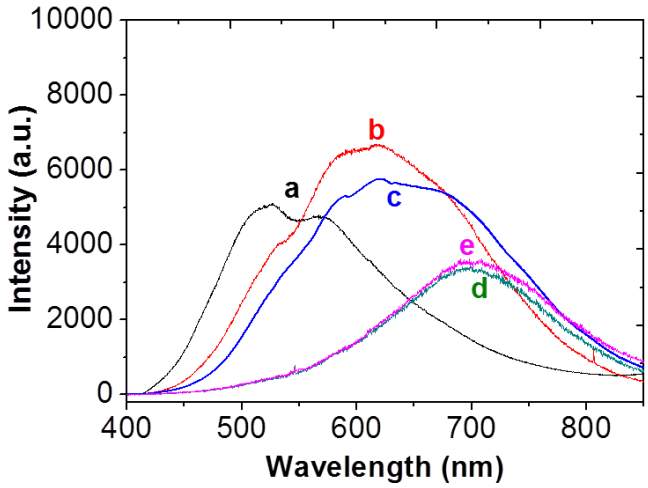

Figure III. 16 *Emission spectra of the CdS doped silica xerogels heated at 120°C 92h: (a) non-heated sample, (b) 0.06 mol.L-1, (c) 0.28 $mol.L^{-1}$, (d) 0.37 $mol.L^{-1}$ and (e) 0.56 $mol.L^{-1}$.*

One can note that the emission spectra of all heated samples are red-shifted with respect to the non-heated one. Furthermore, the emission spectra are red shifted as the precursors

concentration is increased, thus confirming the formation of larger particles, as already shown in Table III.8.

III.1.4.2. Influence of the heating temperature

To study this influence, four identical xerogel samples loaded with precursors in a solution of concentration 0.06 mol.L^{-1}, have been heated at 200, 300, 400 and 500°C for 30 min. The samples turned to yellow after heating at 200°C and became even more deeply coloured after a 300°C treatment. However, they began to turn light yellow at 400°C and completely transparent after heating at 500°C, as shown in Figure III.17.

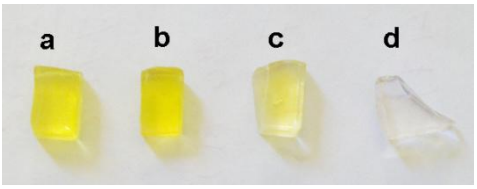

Figure III. 17 *Photograph image of silica xerogels loaded with a CdS solution at 0.06 mol.L^{-1}, then heated at different temperatures for 30 min: (a) 200°C, (b) 300°C, (c) 400°C and (d) 500°C.*

Optical absorption measurements allow following quantitatively the thermal evolution of the sample as shown in Figure III.18.

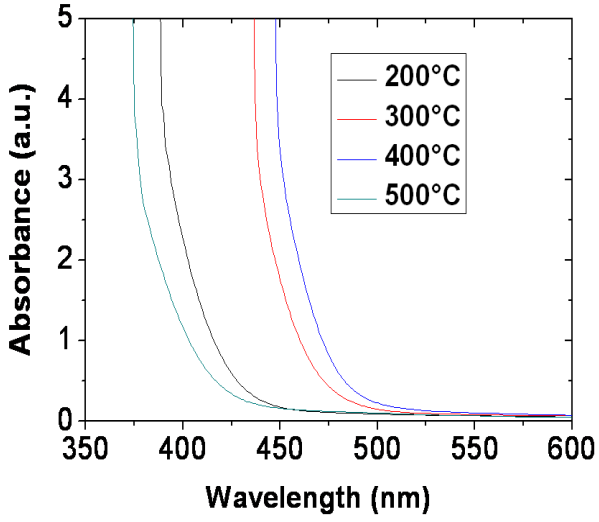

Figure III. 18 *Optical absorption spectra of CdS nanoparticles-doped silica xerogels with a solution concentrated at 0.06 M as function of heating temperatures*

The absorption spectra are red-shifted with increasing the temperature up to 400°C. It means that, in spite of an apparent decreasing optical density, this sample contains larger particles, but

in a smaller concentration. Thus, such a temperature is prone to favour the growth of the biggest particles while the other ones quickly disappear under heat-treatment. Then, the absorption spectrum of the sample heated at 500°C is shifted toward the shorter wavelengths due to the probable oxidation of CdS nanoparticles, the matrix being a porous diffusive medium for oxygen.

The diameter of the CdS particles has been calculated using tight binding model [6] after fitting the absorption data by Eq (III.4) to extract the band gap energies. The derived sizes are approximately 2, 3 and 4 nm for heat-treatment at 200, 300 and 400°C respectively.

The thermal stability of the CdS nanoparticles inside the silica xerogels has also been studied by micro-PL measurements. Figure III.19 shows the emission spectra recorded under excitation at 364 nm with a laser power of 7 mW.

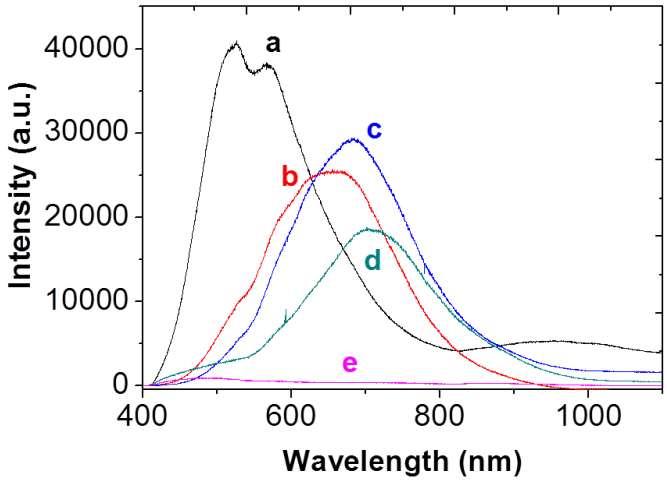

Figure III. 19 *Emission spectra of the CdS doped silica xerogel with 0.06 mol.L^{-1}, (a) non-heated sample (b) 200°C, (c) 300°C, (d) 400°C and (e) 500°C.*

The emission spectra of the samples heated at 200, 300 and 400°C are red-shifted as compared to the non-heated sample emission peak centred around 500 nm (the 2nd peak centered at 1000nm for the non heated sample is attributed to the 2nd order diffraction on the grating of spectrometer). This shift is explained by the emergence of strong band, attributed to the formation of the CdS particles upon heating, while the "matrix" band becomes masked. Moreover, the emission spectra are red-shifted due to the formation of bigger particles as the heating temperature is increased. The heating at 500°C confirms the oxidation of the CdS. In this case, only the response of the silica has been observed at 450 nm due to the degradation at high temperature of both: cadmium and sulfur [22].

III.2. Growth of PbS nanoparticles inside a porous silica matrix

III.2.1. Experimental preparation

Five aqueous solutions S1, S2, S3, S4 and S5 composed of the lead acetate as a precursor of lead, and of thiourea as a sulfur source were prepared. The molar concentration C of the five solutions (S1 to S5) was respectively 0.56, 0.37, 0.28, 0.18 and 0.06 $mol.L^{-1}$. However, the solution S1 was not stable: we had observed a precipitation of the solution during the impregnation and a surface deposition onto the sample instead of a homogeneous doping. Porous silica samples exhibiting interconnected pores of mean diameter 6 nm, a specific surface area of 372 m^2g^{-1} and a pore volume of 0.56 $cm^3.g^{-1}$ were soaked for 4 hours in the S2, S3, S4 and S5 aqueous solutions. The molar ratio between thiourea and lead acetate was kept to 1. Then, the samples were taken out from the solutions and dried at 50°C for 1 hour to remove solvents and retain the precursors within the pores.

To localize the growth of the PbS nanoparticles inside the xerogel, we have also used both a pulsed femtosecond laser and a visible continuous laser. The incident laser power for the infra red irradiation were 10, 25 and 40 mW, while the incident laser power for the visible irradiation were 35, 70, 105 and 140 mW. The relevant parameters (deposited energy density and power density) corresponding to these average powers have been already shown in section III.1.1. (Table III.1 and Table III.2.). In addition, doped silica xerogels have been submitted to heat-treatments in order to compare and to understand the formation mechanism of the PbS nanoparticles.

III.2.2. Growth of PbS nanoparticles by pulsed femtosecond irradiation

Depending on the average power of the laser beam, the irradiated zone showed brown or black color easily visible to the necked eye. A photograph image of the PbS nanoparticles induced by the direct writing of femtosecond laser inside the volume of the PbS-doped xerogel is shown in Figure III.20. This sample doped with a precursor solution concentrated at 0.37 $mol.L^{-1}$ has been irradiated with an incident beam of diameter 2 μm and average power 10 mW. This beam was scanned with a speed of 1 mm/s, producing lines separated by a step of 20 μm.

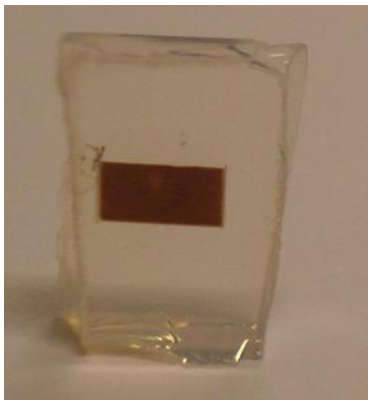

Figure III. 20 *Picture of a transparent PbS precursor-doped silica matrix (0.37 mol.L^{-1}), the femtosecond laser-irradiated area shows a brown color.*

TEM analysis has been performed to evidence the formation of PbS nanoparticles (Figure III.21).

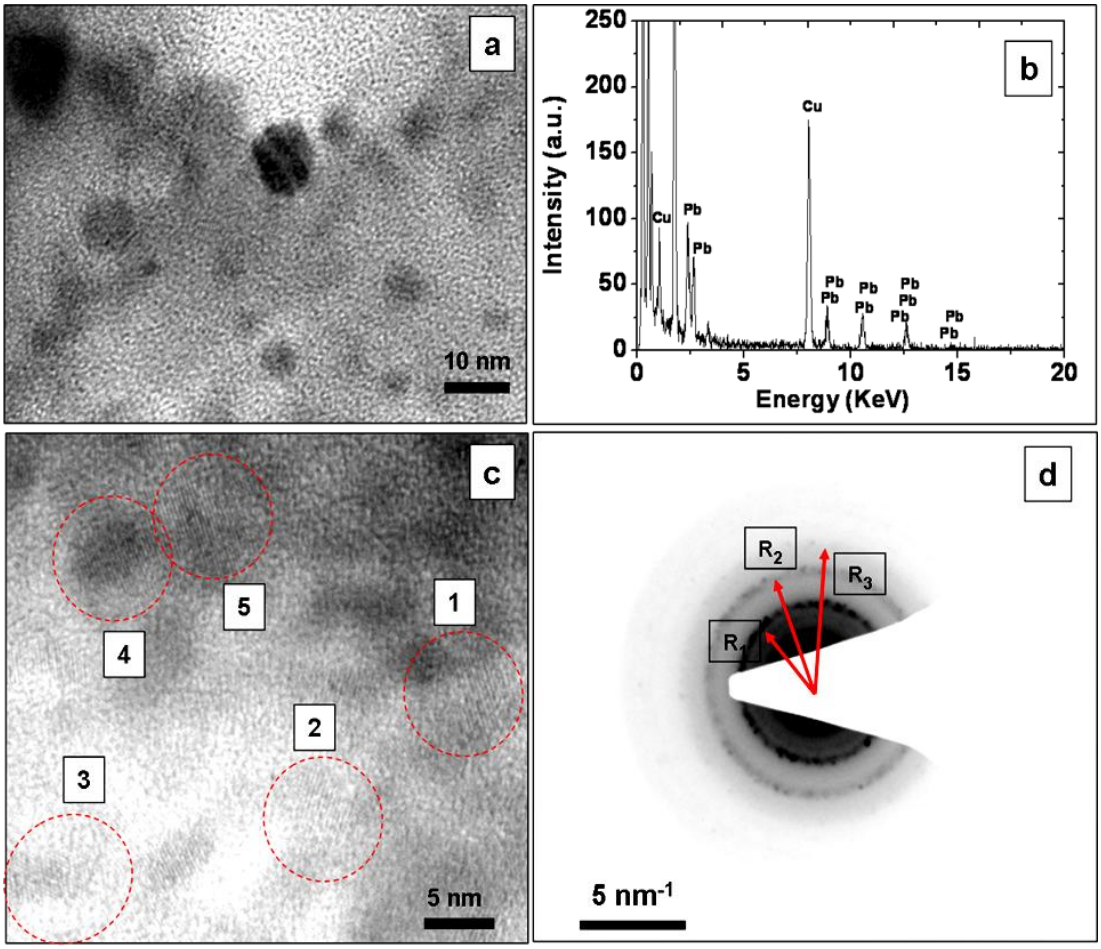

Figure III. 21 *(a) TEM image taken in the irradiated area with 40mW, (b) Energy dispersive X-ray (EDX) spectrum obtained from an ensemble of PbS nanocrystals, (c) HR-TEM image of several PbS nanoparticles, (c) Electron diffraction image taken from a zone filled with nanoparticles.*

Figure III.21 (a) shows a TEM image taken in the brown area of a sample at 40 mW. Quasi-spherical nanoparticles, with a size distribution ranging between 5 and 12 nm have been observed. Figure III.21 (b) shows the EDX analysis recorded on the same area as in Figure III. 21 (a), confirming that the obtained nanoparticles contained Pb atoms. The Cu peaks at ~ 1 and 8 keV came from the TEM grid. Moreover, Figure III.21 (c) presents the HR-TEM of different nanoparticles. The calculation of the atomic interplanar distances has been performed on 5 zones labeled by circles. The zones 1, 2 and 3 exhibit fringe distances around 0.34 nm, which are attributed to the (111) lattice planes of cubic PbS (d_{111} = 0.343 nm, JCPDS card, reference code 03-065-0692), while the fringes spacing for the zones 4 and 5 were of about 0.3 nm, which corresponds to the (200) lattice planes of PbS (d_{200} = 0.297 nm, JCPDS card, reference code 03-065-0692). In addition, Figure III.21 (d) presents an electron diffraction pattern taken in a zone filled with nanoparticles. The estimated diffraction radii R_1, R_2 and R_3 correspond well to the PbS lattice planes (200), (220) and (222) respectively.

The nano-crystallization of PbS inside porous silica occurred in the region of the laser irradiation without any further annealing because of two main processes. Firstly, the multi-photon absorption of the porous silica matrix and of the PbS precursors at 800 nm leads to the decomposition of these precursors, thus enriching the irradiated zone with lead and sulfur ions. In the same time, the temperature elevation during the laser pulse could be sufficient to aggregate the molecular PbS into nanoparticles (see Table III.4).

III.2.2.1. Linear optical properties of PbS nanoparticles created using irradiation by femtosecond laser

Absorption spectra have been recorded in the irradiated and in the non-irradiated areas, as shown in Figure III.22 (A). The absorption spectrum of the zone irradiated with a mean power of 40 mW is red-shifted as compared to the absorption spectra of the non-irradiated zone. Moreover, one can note that the absorbance baseline in the irradiated area is much higher than those of the non-irradiated zone. Such a strong absorption level has been attributed to the formation of PbS nanoparticles in high concentration.

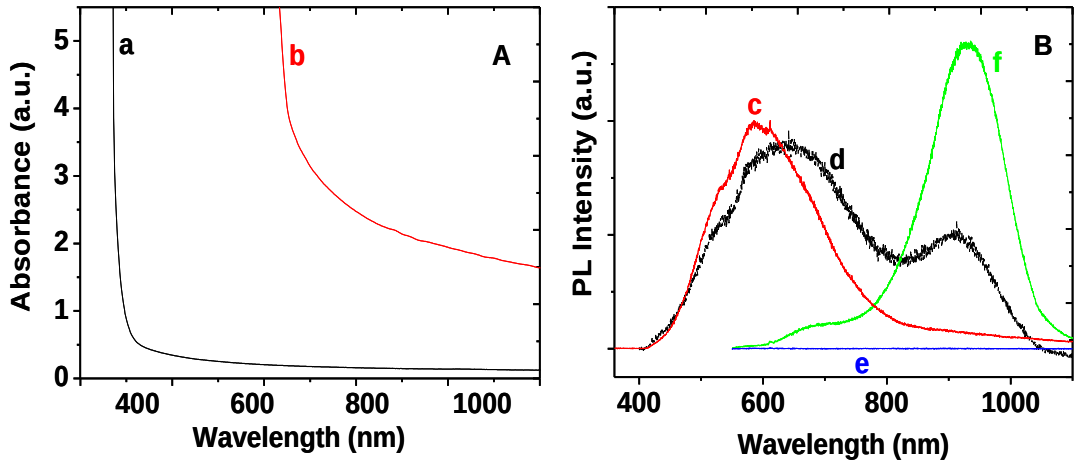

Figure III. 22 *A: Optical absorbance spectra of S-doped silica matrix: (a) non-irradiated area, (b) femtosecond laser irradiated area with 40mW. B: (c) PL spectrum of a non-irradiated area under excitation at 351nm, (d) PL spectrum of the irradiated area under excitation at 351nm, (e) PL spectrum of a non-irradiated area under excitation at 514.5nm and (f) PL spectrum of the irradiated area under excitation at 514.5 nm.*

The corresponding photoluminescence spectra recorded using two different excitation wavelengths are shown in Figure III.22 (B). Under excitation with the 351 nm laser line, the non-irradiated area emits light in a large band centred on 600 nm, while the irradiated area exhibits two emission bands centred around 650 nm and 910 nm. Consequently, the bands peaking at 600 nm and 650 nm could be attributed to the luminescence of PbS precursors and of SiO_2 host matrix, since the S2-doped silica absorption at 350 nm is still strong. On the other hand, the PL band centred at 910 nm is probably due to the PbS nanoparticles. To confirm our assumption, the same PL spectra were recorded under excitation at 514.5 nm. At this wavelength, the S2-loaded matrix absorbs less and as a result, no emission could be observed in the non-irradiated area. However, in the irradiated area, both emission bands are present, although red-shifted by 20 nm. As far as the PbS nanoparticles are concerned, the red-shift of the 910 nm emission band can be interpreted through a resonant size-selection by the excitation wavelength, as already observed with CdS particles [10]. The same kind of selection process in the electronic level population may be assumed for the “matrix band” at 650 nm. Meanwhile, the intensity ratio between these two emission bands is inverted when switching from UV to visible excitation. This can be easily understood as the result of a drastic decreasing number of absorbing entities in the non-irradiated zone between 351 and 514 nm wavelengths.

III.2.2.2. Influence of the femtosecond laser power on the size of PbS nanoparticles

Three samples impregnated with the same solution (0.37 mol.L^{-1}) were irradiated with three different incident average powers 10, 25 and 40 mW. Figure III.23 reports the corresponding absorbance spectra, showing that the band edge is blue-shifted with decreasing the power.

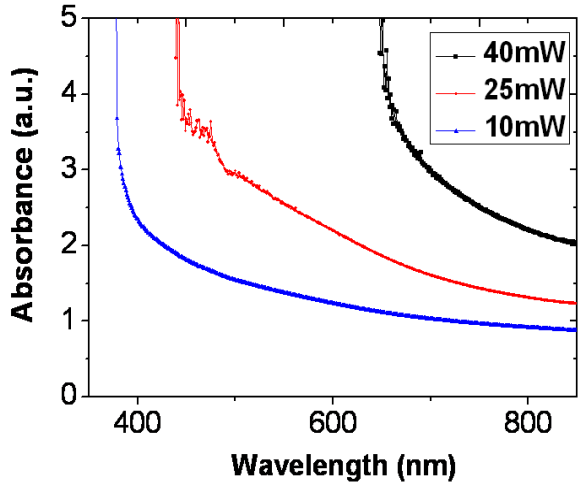

Figure III. 23 *Optical absorbance spectra of PbS precursor-doped silica (0.37 mol.L^{-1}) matrices irradiated with different powers.*

The band gap energies, estimated using equation (III.4), are 1.56, 1.8 and 2.45 eV for the sample irradiated with 40, 25 and 10 mW respectively. The mean diameters of the PbS nanoparticles, deduced from these gap energies using a cluster model correlation curve given by Wang *et al.* [23] (section I.1.4), were of about 4, 3 and 2 nm respectively.

In order to corroborate these data, XRD measurements have been performed on the same irradiated samples as shown in Figure III.24.

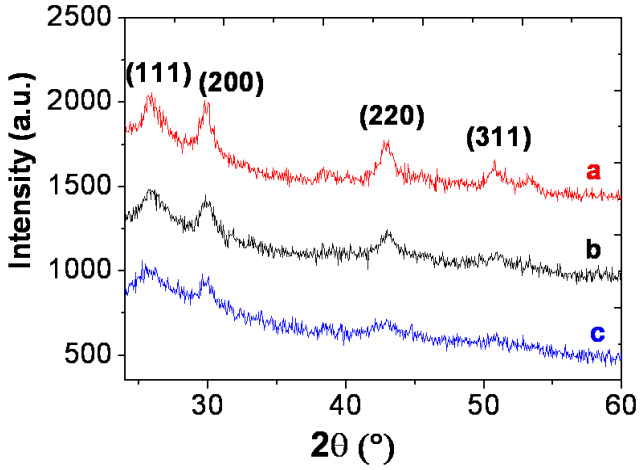

Figure III. 24 *XRD patterns of S2-doped silica matrices recorded in the irradiated area with different laser powers: (a) 40mW, (b) 25mW and (c) 10mW.*

In this figure, reflexes at 2θ equal to 26.06°, 29.9°, 42.9° and 50.85° correspond to the (111), (200), (220) and (311) diffraction planes of PbS cubic structure. It was found that there was an increase in intensity and a decrease in the peak width with an increasing laser power. The mean nanocrystal diameters *d* have been determined from the line-widths (220) of the XRD patterns using Scherrer formula. The diameter of the PbS nanoparticles were 4, 7 and 8 nm for samples irradiated with a laser power of 10, 25 and 40 mW respectively.

Both calculation from absorption and XRD shows the dependence of the diameter size of PbS nanoparticles on the power of the femtosecond laser. The size of PbS nanoparticles increases as a function of the incident power. However, the systematic underestimation of the QDs diameter calculated from the absorption spectra can be attributed to the weak precision of the estimated band gap energy.

III.2.3. Growth of PbS nanoparticles by visible continuous irradiation

The visible irradiations lead to the formation of black colored areas (Figure III.25) on the surface of the doped xerogel, independently from the concentration of the PbS precursors. The power threshold for the eye-visible appearance of this color change was evaluated to about 7 mW. It is well known that the absorption edge of PbS nanoparticles ranges between the visible and the IR domains.

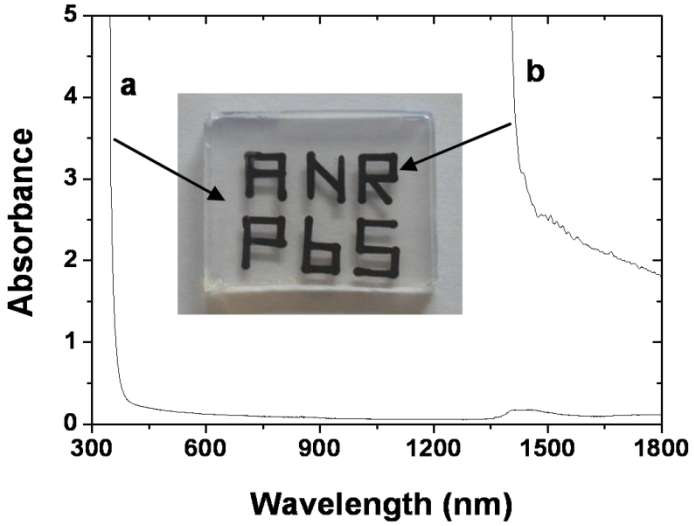

Figure III. 25 *Photograph image and optical absorbance spectra of a PbS precursor doped silica matrix (C = 0.37 mol.L^{-1}): (a) non irradiated area, (b) visible continuous laser irradiated area.*

Figure III.25 presents the absorption spectra of a precursors-loaded matrix (C = 0.37 mol.L^{-1}) before and after irradiation with an incident power of 140 mW. The red-shift of the absorption

threshold wavelength from 347 nm to 1278 nm is noticeable after the laser irradiation. This is naturally to be related to the black coloration, which can be attributed to the formation of PbS nanoparticles inside the irradiated area.

TEM analysis has been performed after grinding the irradiated area into a powder. Quasi-spherical nanoparticles, with a size distribution have been observed as shown in Figure III.26 (a, b and c). Figure III.26 (d) presents the HR-TEM image of a single nanoparticle, it exhibits a fringe spacing of 0.297 nm, in good agreement with the spacing distance d_{hkl} between the (200) lattice planes of cubic PbS (JCPDS card, reference code 03-065-0692). The size of the nanoparticle shown in the Figure III.26 (d) is about 13 nm.

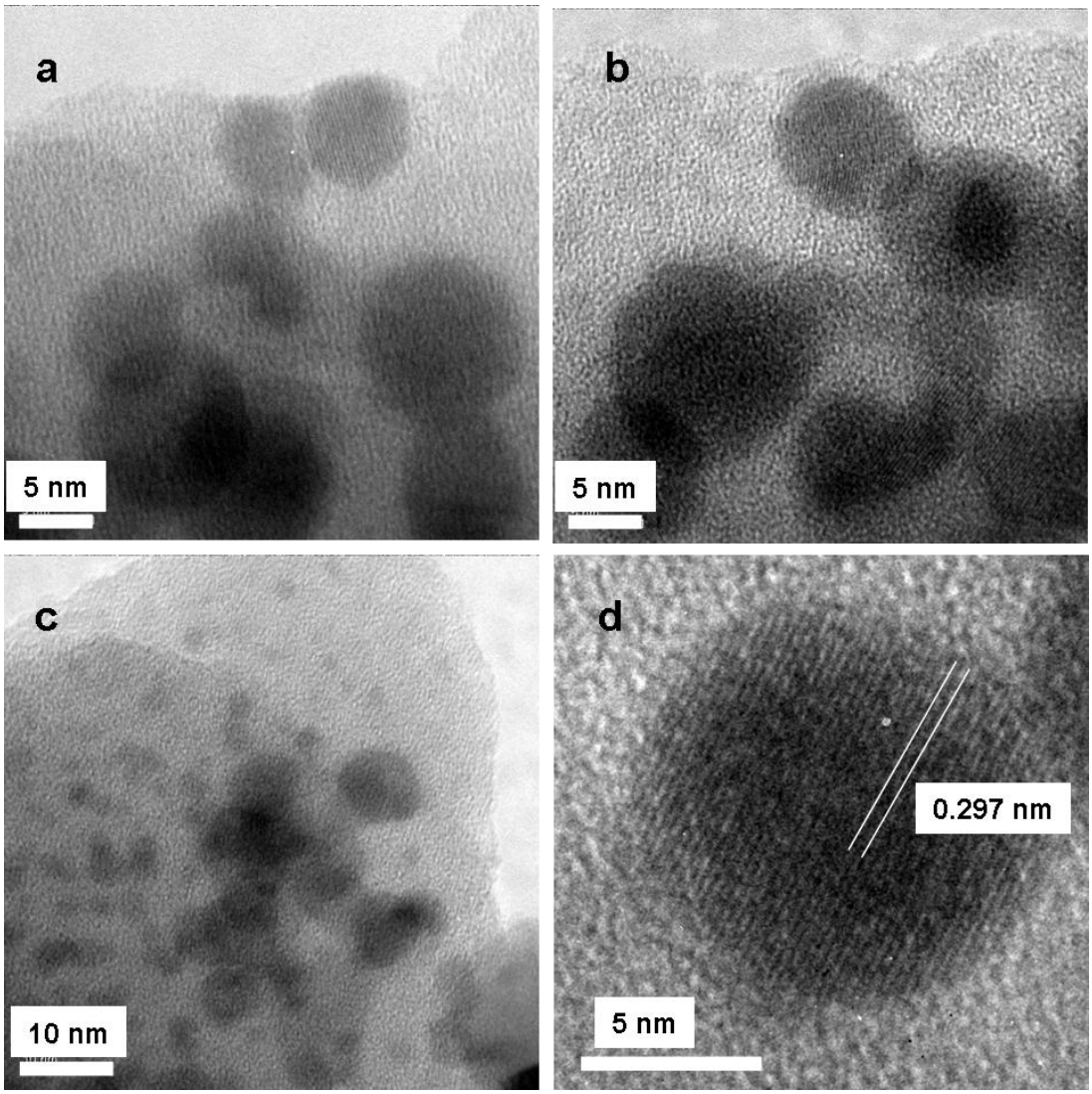

Figure III. 26 *(a, b and c) micrograph TEM images taken in the irradiated area of the highly doped sample (C = 0.37 mol.L^{-1}) (b) HR-TEM of a single nanoparticle.*

III.2.3.1. Influence of the precursor concentration on the size of PbS nanoparticles created by 514.5 nm irradiation

Four samples impregnated with different concentrations (0.37, 0.28, 0.18, 0.06 mol.L^{-1}) have been irradiated with the same incident power of 140 mW. In the absence of any excitonic structure in the absorption spectra, the band gap energy has been estimated using equation (III.4) from the absorption edge blue-shift in the Tauc's plots shown in Figure III.27 (left). The band gap energies were estimated to be 0.85 eV, 0.91 eV, 1.06 eV and 1.5 eV for concentrations 0.37, 0.28, 0.18 and 0.06 mol.L^{-1}, respectively.

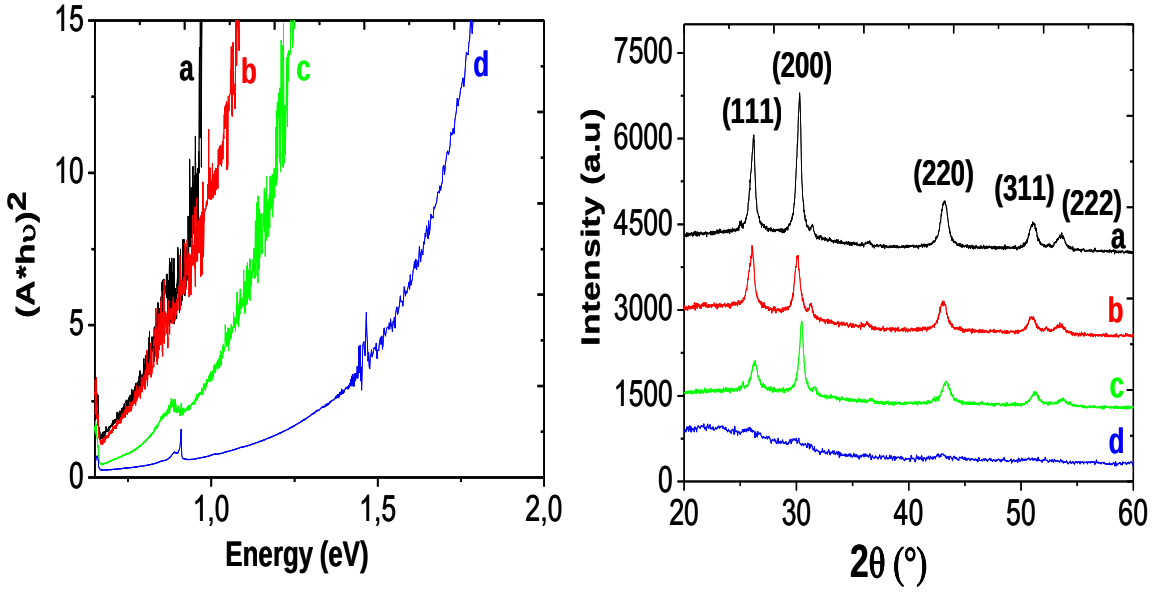

Figure III. 27 *Left: Tauc plots for the direct transition of PbS nanocrystals in samples doped with different concentrations. Right: XRD patterns recorded in the irradiated area; (a) C = 0.37 mol.L^{-1}, (b) C = 0.28 mol.L^{-1}, (c) C = 0.18 mol.L^{-1}, (d) C = 0.06 mol.L^{-1}.*

The size of nanocrystals was then estimated from the cluster model and reported in Table III.9.

Concentrations (mol.L^{-1})	Size from absorption (nm)	Size from XRD (nm)
0.37	**9**	**11**
0.28	**7**	**10.5**
0.18	**5**	**10**
0.06	**4**	**8**

Table III. 9 *Calculated values of nanoparticle sizes from absorption and XRD measurements for different concentrations.*

Unsurprisingly, the diameter of the PbS nanocrystallites increases with the concentration. Figure III.27 (right) shows the evolution of the XRD patterns in the irradiated area of the impregnated xerogels when decreasing the precursor's concentration. These patterns all exhibit reflexes corresponding to the PbS cubic structure, the intensity of which becomes very weak in the case of the lowest concentration. The diameter of the PbS nanoparticles calculated by the Scherrer formula are summarized in Table III.9 together with the values deduced from the absorption.

It is clear that both characterization methods confirm the trend of the PbS nanoparticles size to increase with the precursors concentration. However, the diameters calculated from the absorption spectrum are somewhat smaller than those calculated from the XRD measurements. As previously explained, this difference could be attributed to the absence of an exciton peak in the absorption spectra of the irradiated samples, so that the determination of the absorption band edge has been performed with a weak precision.

(N.B: This size dependence on the concentration has also been confirmed by using different laser powers 105, 70 and 35 mW).

III.2.3.2. Influence of the incident power on the size of PbS QDs created by 514.5 nm irradiation

The irradiation with three incident powers 140, 105 and 70 mW have been performed on the xerogels doped with a PbS precursors concentration of 0.37 mol.L^{-1}. The corresponding XRD measurements are shown in Figure III.28.

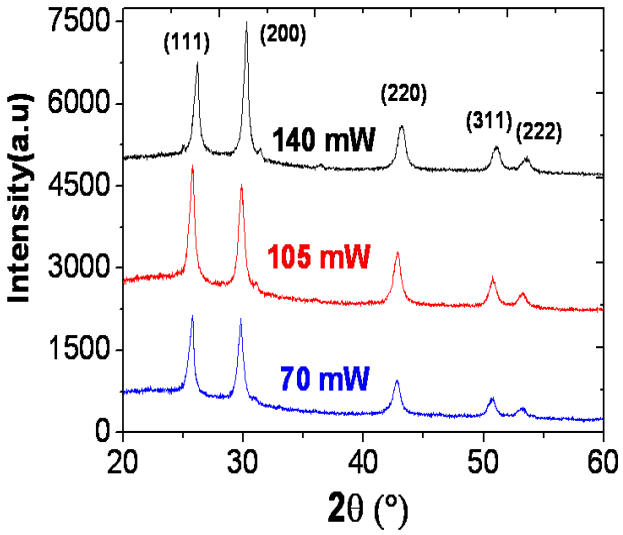

Figure III. 28 *XRD patterns of PbS precursors-doped silica matrices irradiated with different incident powers: (140, 105 and 70 mW).*

The mean diameters of PbS nanoparticles have been calculated by Scherrer formula. The sizes were 11, 11.5 and 11 nm for the samples irradiated at 140, 105 and 70 mW respectively. This result suggests that, at least for the highest concentration C = 0.37 mol.L^{-1}, there is no influence of the incident power on the size of the precipitated PbS particles. However, this latter conclusion contradicts the optical absorption measurements on the same sample, as shown in Figure III.29 (A).

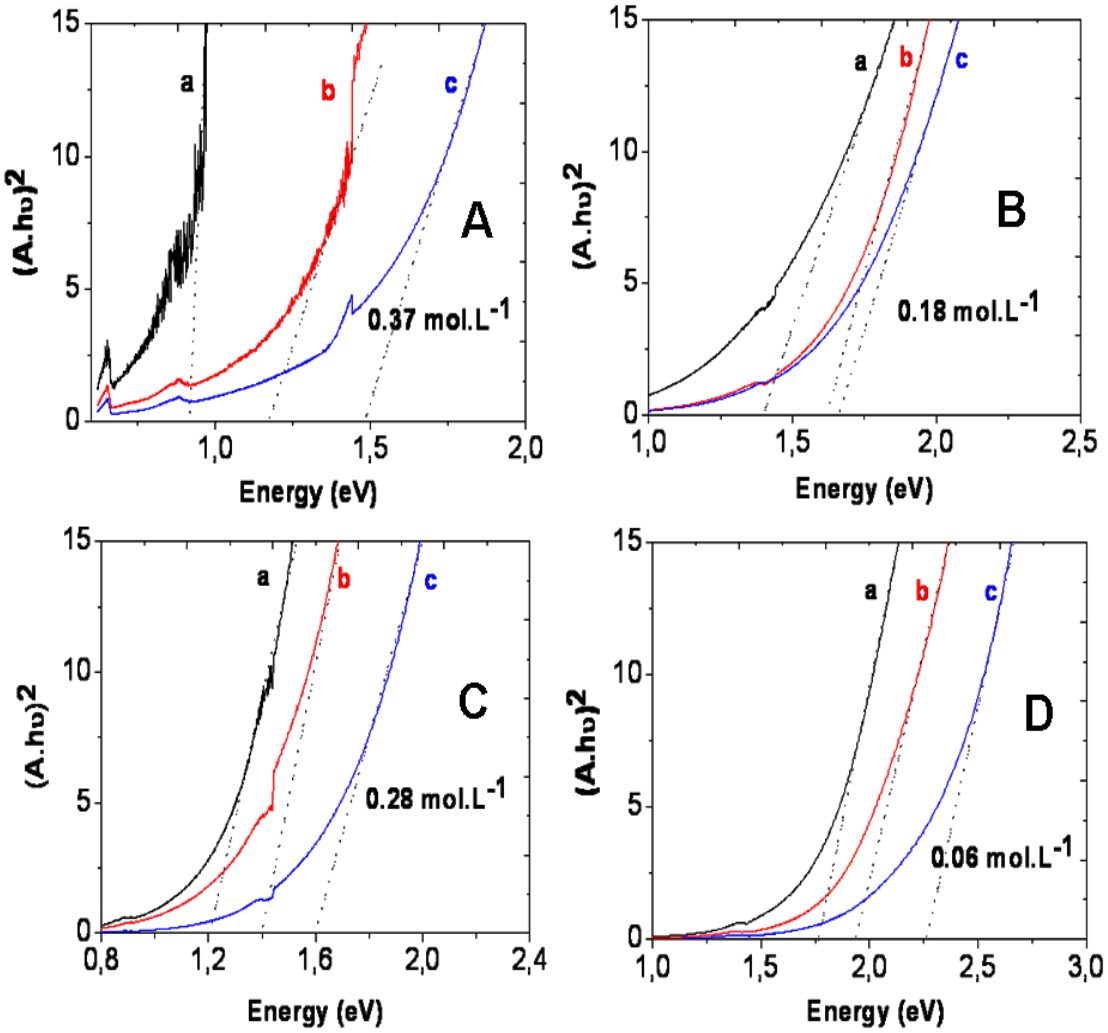

Figure III. 29 *Tauc plot of the absorption data for all irradiated samples at different incident powers and different concentrations. (a) 140mW, (b) 105 mW and (c) 70 mW.*

Indeed, the absorption edge blue-shift reflects an increase in the effective band gap when decreasing the incident power, which would mean the diameter PbS particle size decreases with the incident power. This apparent influence of the incident laser power has been studied at various concentrations by using 140, 105 and 70 mW. The corresponding absorption spectra are shown in Figure III.29. Slight blue shifts are systematically observed as the incident power is

decreased from 140 to 70 mW for all samples. The band gap energies for all irradiated samples have been estimated and summarized in Table III.10.

Concentrations (mol.L^{-1})	140 mW		105 mW		70 mW	
	E_g (eV)	Diameter (nm)	E_g (eV)	Diameter (nm)	E_g (eV)	Diameter (nm)
0.37	**0.85**	**9**	**1.1**	**7**	**1.4**	**5**
0.28	**1.2**	**7**	**1.35**	**5**	**1.6**	**4**
0.18	**1.4**	**5**	**1.6**	**4**	**1.7**	**3.8**
0.06	**1.6**	**4**	**1.9**	**3.5**	**2.25**	**2.8**

Table III. 10 *PbS band gap energies estimated at different concentrations and different incident powers.*

These estimated band gap energies are significantly higher than the bulk PbS value, indicating a strong confinement effect. Hence, Table III.10 seems to point out that the mean diameter of the PbS NPs not only depends on the impregnation concentrations, but also on incident laser power.

To summarize this section, the nanoparticle size, which can be adjusted by choosing the concentration of precursors in the post-doping solution, may apparently exceed the mean pore diameter of the silica xerogel. The formation of PbS nanoparticles larger than the pore size could be correlated to a fast diffusion of Pb^{2+} and S^{2-} ions under laser irradiation, due to the presence of interconnected pores inside the silica host matrix. Hence, the growing of large PbS nanoparticles is accompanied by the deformation and even the destruction of the pore walls in their vicinity, as it has already been evidenced in a recent work with metallic nanoparticles [24]. However, PbS nanoparticles with size smaller than the pore diameter could be generated by adjusting the concentration of the precursors and eventually the incident laser power.

III.2.4. Growth of PbS nanoparticles by heat-treatment

To better understand the mechanism involved in the precipitation of PbS nanoparticles under continuous laser irradiation, these results have been compared with those obtained from a classical temperature-induced nanocrystal growth. To this purpose, xerogels with pores average diameter of 6 nm and a specific surface area of 372 m^2g^{-1} doped by impregnation in the same conditions as the ones used before laser-induced crystal growth were submitted to heat-treatment. Initially transparent, the samples quickly turned deep orange, brown or even black, depending on the precursors concentration and on the thermal treatment duration. Figure III.30

(left) shows the optical absorption spectra of a xerogel doped with PbS precursors in a solution of concentration 0.37 mol.L^{-1} before and after heat-treatment at 120°C for 2 hours. The heat-treatment produces a red-shift from 300 nm to 750 nm, probably due to the formation of the PbS nanoparticles. Moreover micro-PL measurements have been performed on the same heated sample, as shown in Figure III.30 (right). Under excitation with 647 nm, a rather narrow emission band (~ 200 meV) centred at 950 nm has been observed, which can be attributed to PbS nanoparticles.

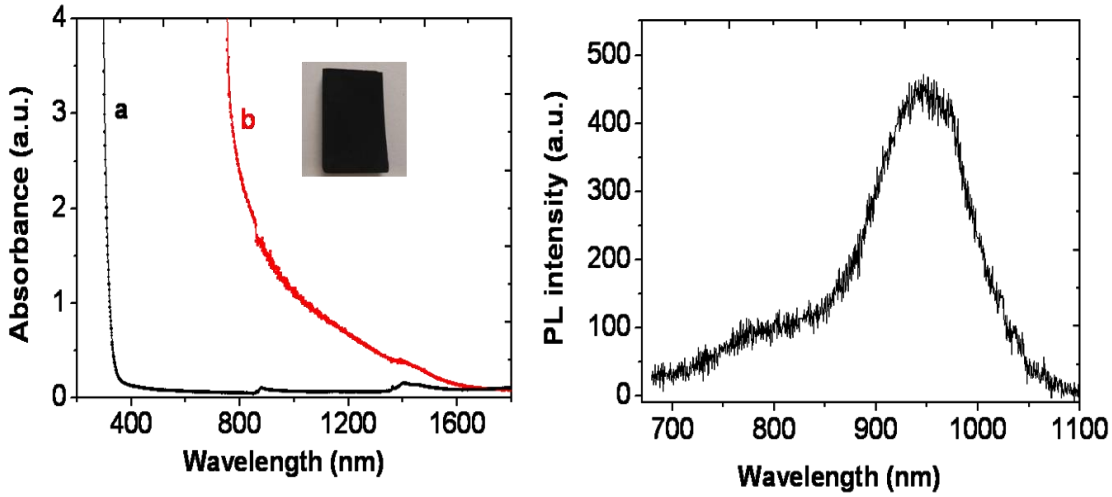

Figure III. 30 *Optical absorption of PbS-doped silica with 0.37 mol.L^{-1}, (a) without heat-treatment (b) heated at 120°C for 2h. Right: emission spectra of the heated sample under excitation with 647 nm.*

III.2.4.1. Influence of the precursors concentration on the size of PbS QDs created by heat-treatment at 120°C

Xerogels loaded with different concentrations of PbS precursors have been heated at 120°C for 2 hours. Absorption spectra have been exploited using equation (III.4), as shown in Figure III.31 (left).

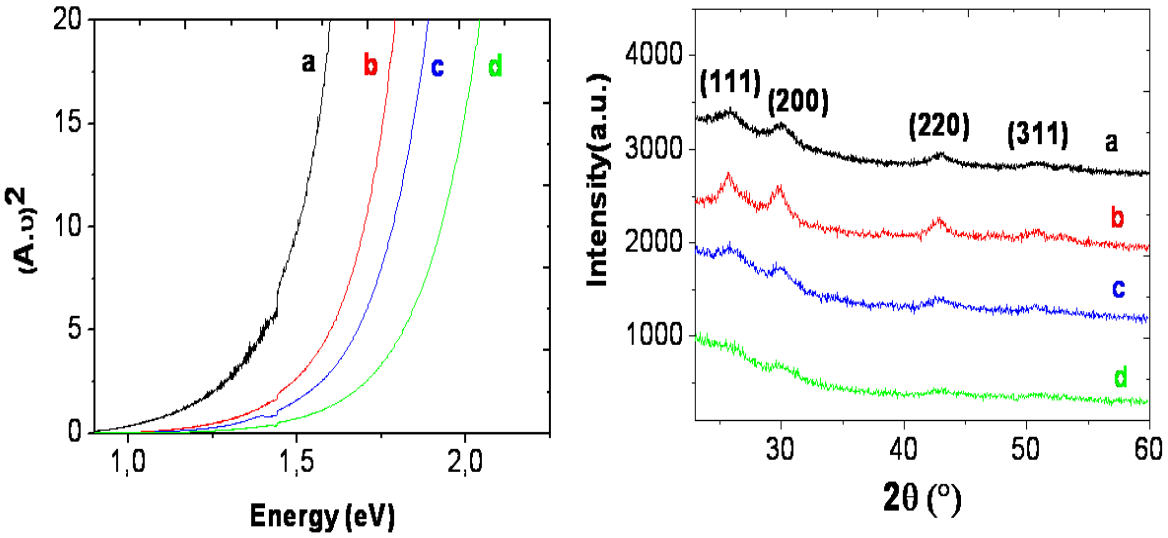

Figure III. 31 *Left: Tauc's plots for the direct transition of PbS nanocrystallites in samples doped with different concentrations and heated at 120°C for 2h. Right: XRD patterns performed on the same samples (a) C = 0.37 mol.L^{-1}, (b) C = 0.28 mol.L^{-1}, (c) C = 0.18 mol.L^{-1}, (d) C = 0.06 mol.L^{-1}.*

The cluster model [23] has been used to evaluate the mean particle sizes from the blue-shift of the front edge. The calculated diameters of PbS nanoparticles at different concentrations are summarized in Table III.11, together with the obtained sizes calculated from the XRD patterns shown in Figure III.31(right), showing here a good correlation between the two methods.

Concentration (mol.L^{-1})	**size from absorption (nm)**	**Size from XRD (nm)**
0.37	**5**	**6**
0.28	**4**	**5**
0.18	**3.5**	**4**
0.06	**3**	**-**

Table III. 11 *PbS nanoparticle size calculated from absorption and from XRD measurements*

Furthermore, this table shows that the PbS nanoparticles size increases as a function of the precursors concentration, which is consistent with the behaviour observed under visible laser irradiation. The significant difference in diameter between thermally induced and light-induced PbS nanoparticles might be explained by the low temperature employed here for the heat-treatment as compared to the temperature arising from the laser irradiation.

III.2.4.2. Influence of the heating time on the size of PbS QDs at 120°C

A silica xerogel doped with PbS precursors in a concentration of 0.37 mol.L^{-1} has been prepared and heated at 120°C for several durations ranged from 20 minutes to 2 hours. The color of the sample changed from deep orange for 20 min annealing to black for annealing durations starting from 30 min. Figure III.32 shows, the absorption edge shifting towards higher wavelengths as the heating time increases, which may be attributed to the increase in the size of the PbS crystallites.

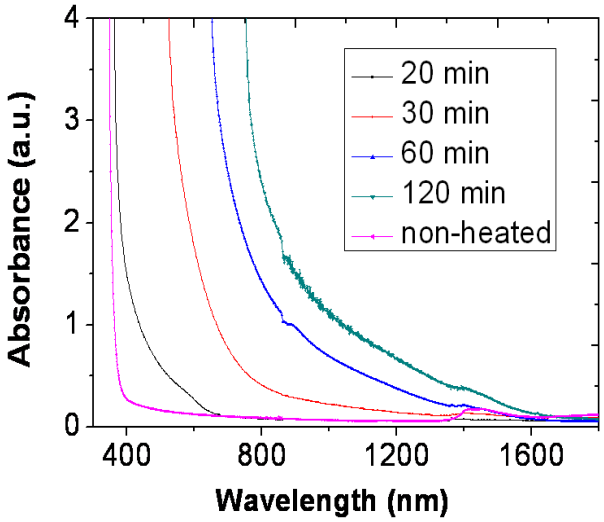

Figure III. 32 *optical absorption of a PbS-doped silica xerogel with the highest concentration heated at 120°C for different durations.*

The estimated nanoparticles sizes were 5, 4, 3 and 2 nm, corresponding to heating times 120, 60, 30 and 20 min respectively.

It is worthy to stress that no significant change in the absorption spectra could be noticed when the same doped xerogels were heat-treated for a longer time. This could mean that the nanocrystal growth is limited by the matrix porosity.

III.2.4.3. Influence of heating temperature on the size of PbS QDs

Xerogels post-doped with the highest PbS precursors concentration were prepared, then heated at 120, 200 and 300°C for 2 hours. The color of the heated samples changed from black at 120°C and 200°C to light brown at 300°C. The corresponding optical absorption spectra and XRD patterns are shown in Figure III.33.

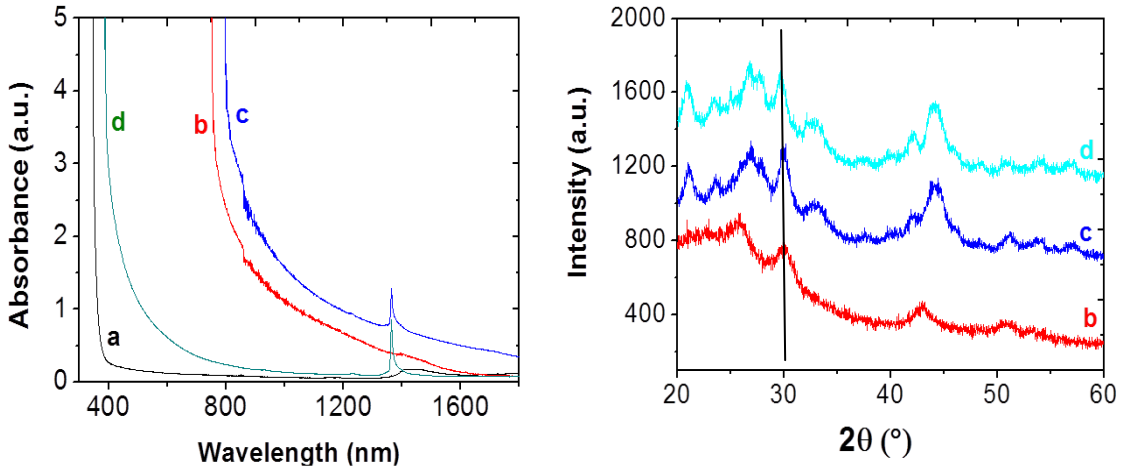

Figure III. 33 *Left: Optical absorption spectra of xerogel doped with 0.37 mol.L^{-1} and heated at different temperatures. Right: XRD patterns recorded on the heated samples (a) non-heated, (b) 120°C 2h, (c) 200°C 2h, (d) 300°C 2h.*

For the heat-treatment temperatures up to 200°C, the absorption band edge is red-shifted as compared to the non-heated sample, which is consistent with the formation of bigger particle under heating. On the contrary, a strong blue-shift is observed after heating at 300°C for 2h. This one could be explained by the oxidation of the PbS nanoparticles. Figure III.33 (right) presents the XRD patterns for the samples heated at 120°C, 200°C and 300°C. Most of the XRD peaks are in good agreement with the crystalline phase of PbS (cubic phase). The observed increasing peak width when the heating temperature is increased indicates a decreasing size of the nanoparticles, which could be correlated with an oxidation of the particles shell. However, the noisy signal made it very difficult to calculate a particle diameter. More important are the new reflexes observed in the diffractograms (20.73°, 24. 032°, 28.126°, 31.474° and 42,611°) after heating at 200°C and 300°C. These ones may be attributed to the probable oxidised compound $PbO.PbSO_4$ (JCPDS card, reference code 00-006-0275).

III.2.5. Stability of PbS nanoparticles

The important drawback that limits the use of PbS nanoparticles in many applications is their low chemical stability. This is due to their high ability to oxidize, which reduces their lifetime in ambient conditions. The speed of PbS oxidation depends on different parameters such as particle size, medium where they are formed, etc...

III.2.5.1. Stability of PbS nanoparticles created by 514.5 nm continuous laser irradiation

A naked eye observation allows noticing the oxidation of PbS nanoparticles after their creation by irradiation at 514.5 nm in ambient conditions, as shown in Figure III.34.

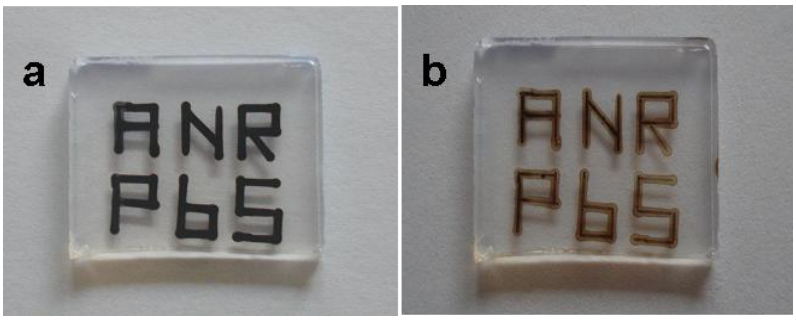

Figure III. 34 *Pictures of 514.5 nm continuous laser writing inside a silica xerogel doped with 0.37 mol.L^{-1} PbS precursors: (a) just after irradiation, (b) after several days.*

As shown in Figure III.35 (left), the absorption band edge was blue-shifted with time, which may correspond to the fast oxidation of PbS nanoparticles in the silica xerogel. XRD patterns of the irradiated sample, as reported in Figure III.35 (right), show the PbS characteristic main reflexes, the intensities of which decreased with time. Furthermore, a new phase has been detected, with a peak position (circled in the graph) probably corresponding to the compound $PbO.PbSO_4$.

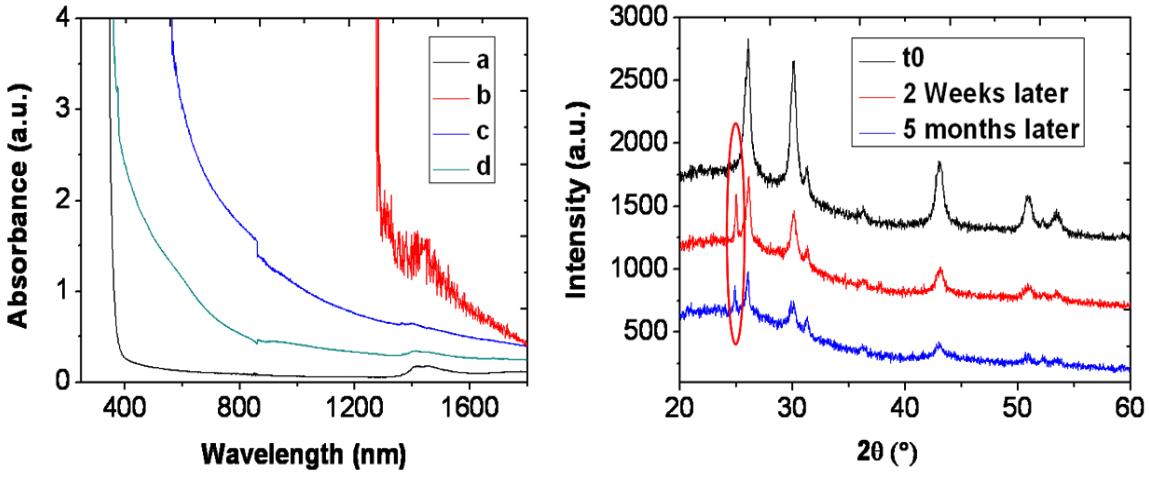

Figure III. 35 *Stability of PbS nanoparticles created by laser irradiation at 514.5 nm. Left: optical absorption spectra. (a) Non-irradiated area, (b) t_o just after irradiation, (c) after 2 weeks, (d) after 100 days. Right: XRD pattern at different times after irradiation.*

Two main reasons could explain such an oxidation. Firstly, most of the PbS nanoparticles are formed near the surface of the silica xerogel, which allows PbS to directly interact with ambient atmosphere. Secondly, the formation of PbS nanoparticles with a size greater than the average pore diameter of the silica xerogel tends to break the walls of the interconnected pores, allowing the penetration or the diffusion of a sufficient amount of oxygen to oxidize the PbS nanoparticles.

In order to stabilise the PbS nanoparticles, they were tentatively covered with a polymer PMMA. The idea was to block the penetration of the oxygen into the irradiated area. A desired quantity of methyl methacryliate acid (MMA, from Aldrich) was put in a round bottom flask at room temperature. To it was added Azobisisobutyronitrile AIBN for catalyzing the free radical polymerization. The reaction mixture was then stirred at about 60–75°C for 30 min. The irradiated xerogel was immersed in the mixture solution for one hour. After that, it was taken out from the mixture and put in an oven at 50°C for 24h. Figure III.36 reports the optical absorption of an irradiated sample (0.37 mol.L^{-1}, 514.5 nm and 140 mW) impregnated with the polymer, at different times after its drying step.

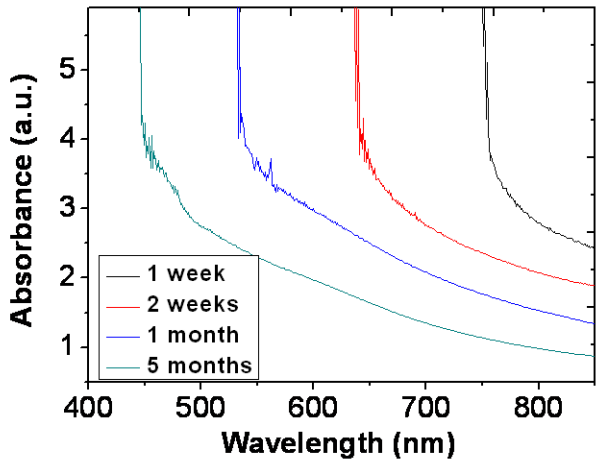

Figure III. 36 *Optical absorption of the irradiated area impregnated with PMMA at different times.*

The polymer PMMA clearly does not completely prevent PbS from any oxidation, but the oxidation rate is slowed down in comparison with a sample without PMMA.

III.2.5.2. Stability of PbS nanoparticles created using pulsed femtosecond laser

Femtosecond laser-irradiated samples have been left in ambient air for a long period and optical absorption spectra has been recorded at different times after the irradiation. Figure III.37 shows

such absorption spectra for two samples irradiated with 10 mW and 40 mW at three different times after the irradiation. One can note that the absorption edge of the sample irradiated with 40 mW undergoes a blue-shift after several days. This blue-shift is attributed to the oxidation of PbS nanoparticles created inside the silica matrix. On the other hand, the absorption edge of the sample irradiated with 10 mW presents no shift after 100 days.

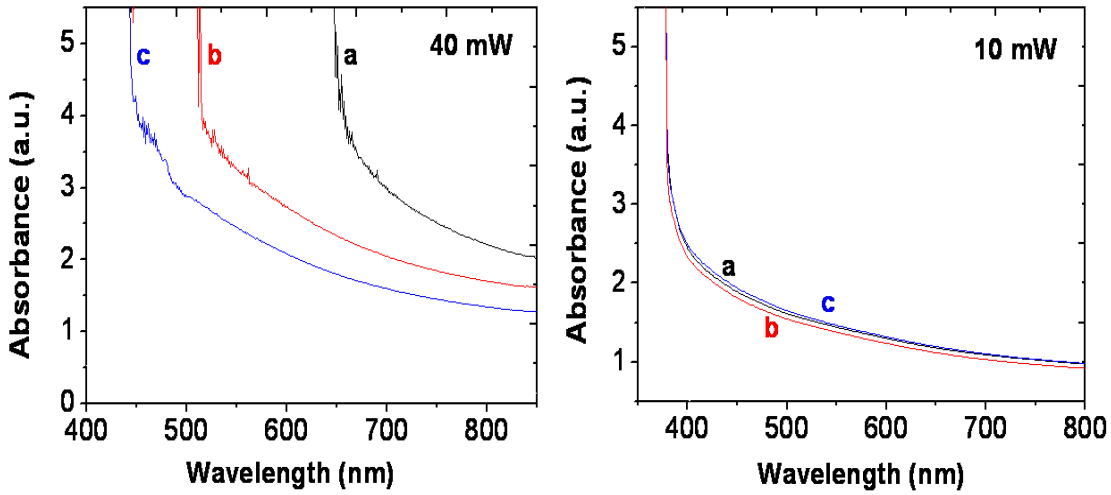

Figure III. 37 *Optical absorption of PbS nanoparticles created by femtosecond laser at different times after irradiation; Left: sample irradiated with 40 mW, Right: sample irradiated with 10 mW. (a) t_0 just after irradiation, (b) 50 days after irradiation and (c) 100 days after the initial irradiation.*

These preliminary results demonstrate that the stability of PbS nanoparticles, inside the porous host matrix, depends on their size. It is worthy to be recalled that the PbS particle mean size, as deduced from the XRD measurements around time t_0, has been evaluated to 4 and 8 nm after irradiations with 10 mW and 40 mW respectively. In the first case, the crystallite size is thus smaller than the average matrix pore size of 6 nm, as opposed to the case of 40 mW irradiation. Since the diameter of PbS nanoparticles created with 40 mW is greater than the pore diameter, it implies that, under the extreme local conditions of the femtosecond laser-induced plasma, the nanoparticles are able to break the walls of the interconnected pores during their formation. An important amount of oxygen is then allowed to diffuse inside the matrix and to react with PbS nanoparticles, leading to their oxidation in several days. On the contrary, with a lower laser power of 10 mW, most of the nanoparticles have a size (4 nm) fitting to the pores. In this case, it is likely that the nanoparticles have grown without any modification of the silica matrix and these particles remain protected from oxidation by the silica walls. This effect could explain the stability of PbS nanoparticles, even after 100 days. Hence, both the pore diameter of the host

silica matrix and the power of pulsed femtosecond laser irradiation play an important role in the stability of the obtained PbS nanoparticles.

For further demonstration, a silica xerogel with 11 nm diameter pores has been impregnated with a PbS precursors solution of concentration 0.37 mol.L^{-1}. Femtosecond laser irradiations have been performed inside this PbS-doped silica xerogel with 2 incident laser powers (20 mW and 40 mW), the optical absorption spectra if which are shown in Figure III.38.

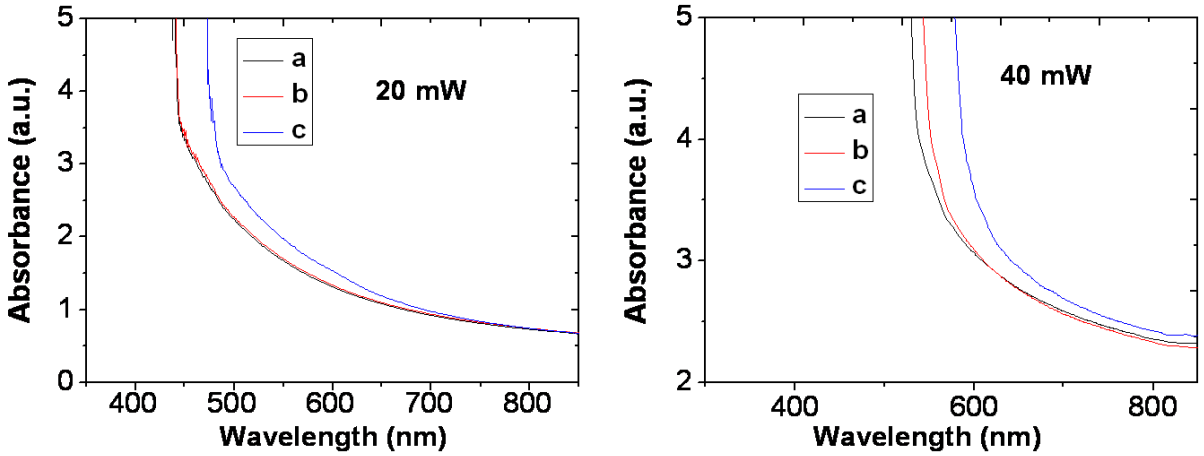

Figure III. 38 *Optical absorption of PbS nanoparticles created by femtosecond laser inside a porous silica of pore diameter 11 nm. Left: sample irradiated with 20 mW. Right: sample irradiated with 40 mW, (a) t_0 just after irradiation, (b) one week after irradiation and (c) 3 months after irradiation.*

For both laser powers, a small red-shift of the absorption edge was observed after 3 months. However, these shifts have almost no impact on the PbS nanoparticles mean size since the band gap energy varies from 2.3 eV to 2.1 eV and from 1.9 eV to 1.7 eV for 20 mW and 40 mW laser powers respectively, which corresponds to a nanoparticle diameter varying from 2.8 to 3 nm and from 3.5 to 3.8 respectively. These diameters of 3 and 5 nm remain much less than the pores diameter of 11nm.

Conclusion

Silica xerogels have been impregnated with CdS or PbS precursors. Both annealing and irradiation processes lead to the pyrolysis and the decomposition of the precursors, which results in CdS or PbS nanoparticles formation. Absorption and PL spectroscopy, Raman spectroscopy, X-ray diffraction analysis and TEM measurements have been used to identify the CdS, PbS crystallites inside the xerogel and to estimate the average particle size. The direct space-selective growth of CdS or PbS nanoparticles has been achieved using pulsed femtosecond and

visible continuous laser irradiation. In the case of femtosecond infrared radiation, the nano-crystallization of CdS or PbS inside the porous silica could occur in the region of the laser beam focus due to two main processes. First, the multiphoton absorption of the porous silica matrix doped with CdS or PbS precursors at 800 nm results in the decomposition of the precursors and the enrichment of the irradiated zone with cadmium or lead and sulfur ions. The second process is due to the subsequent temperature rising, which is sufficient to aggregate the molecular CdS or PbS into nanoparticles. In the case of a continuous laser irradiation in the visible domain, a direct photo-thermal mechanism at relatively high temperature (greater than 120°C) is at the origin of the laser-induced crystallization of CdS. Indeed, one can expect that under visible irradiation, the dissolved precursors absorb a small part of the laser energy, which heats the surface atoms and allows CdS or PbS nanoparticles to grow in the silica matrix. Through both fabrication methods, the nanoparticle size can be adjusted by choosing the concentration of precursors in the post-doping solution, the laser wavelength in case of irradiation and the temperature in the case of heating. Two different structural phases of CdS have been observed, one cubic and one hexagonal, while the structure phase for PbS was always cubic. The stability of PbS nanoparticles precipitated inside the silica host by laser irradiation and then let in ambient conditions, have been shown to depend on the particle size and on the porosity of the host matrix.

References

1. A.N. Murashkevich, V.G. Vashina, I.M. Zharskii. J. Sol-Gel Sci.Technol. **20,** 7 (2001).
2. K. Rajeshwar, N.R. de Tacconi, C. R. Chenthamarakshan. *Chem. Mater.* **13,** 2765 (2001).
3. Y. Wang, N. Herron. *J. Phys. Chem.* **95,** 525 (1991).
4. J.J. Shiang, S.H. Risbud, A.P. Alivisatos. J. Chem. Phys. **98,** 8432 (1993).
5. N.F. Mott, E.A. Davis. Electronic Processes in Non-Crystalline Materials. Oxford, Clarendon: 1979.
6. P.E. Lippens, M. Lanno. Phys. Rev. B **39,** 10935 (1989).
7. H. Yang, P. Holloway. Appl. Phys. Lett. **82,** 196 (2003).
8. H.Y. Zhao, E.P. Douglas. Chem. Mater. **14**, 141(2002).
9. F. Zezza, R. Comparelli, M. Striccoli, M.L. Curri, R. Tommasic, A. Agostiano, M. Della. Synth. Met. **139,** 59 (2003).
10. B. Capoen, T. Gacoin, J.M. Nedelec, S. Turelle, M. Bouazaoui. J.Mater.sci. **36,** 2565 (2001).
11. K. Raulin , O. Cristini, P. Baldeck, O. Stéphane, C. Kinowski, S. Turrell, B. Capoen, M. Bouazaoui. J. Nanopart. Res. **12,** 1459 (2010).
12. H. El Hamzaoui, R. Bernard, A. Chahadih, F. Chassagneux, L. Bois, D. Jegouso, L. Hay, B. Capoen, M. Bouazaoui. Nanotechnology **21,** 134002 (2010).
13. H. El Hamzaoui, R. Bernard, A. Chahadih, F. Chassagneux, L. Bois, D. Jegouso, L. Hay, B. Capoen, M. Bouazaoui. Mater. Lett. **64,** 1279 (2010).
14. J.P. Gordon, R.C. Leite, R.S. Moore, S.S. Porto, J.R. Whinnery. J. Appl. Phys. **36,** 3 (1965).
15. JCPDS card, reference code 00-041-1049.
16. K. Santanu, M. Biswanath. J. Phys. Chem. C **111,** 16734 (2007).
17. R.J. Bandaranayake, G.W. Wen, J.Y. Lin, H.X. Jiang and C.M. Sorensen. Appl. Phys. Lett. **67,** 831 (1995).
18. B. Cullity. Elements of X-Ray Diffraction 2nd edn. Addison-Wesley, 1978.
19. JCPDS card, reference code 00-001-0647.
20. T. Vossmeyer et *al*. J. Phys. Chem. **98,** 766 (1994).
21. S. Gorer, G. Hodes, Y. Sorek, R. Reisfeld. Mater. Lett. **31,** 20 (1997).
22. G. Ehrhart. Elaboration et caractérisation de films vitreux nanostructurés par voie sol-gel. Mise en évidence du transfert d'énergie entre les nanoparticules semi-conductrices de CdS ou de ZnS et les ions Eu^{3+}. Univ. lille 1, 2006.
23. Y. Wang, N. Herron. J. Phys. Chem. **91,** 257 (1987).

24. M.T. Bore, H.N. Pham, E.E. Switzer, T.L. Ward, A. Fukuoka, A.K. Datye. J. Phys. Chem. B **109,** 2873 (2005).

Chapter IV: Precipitation of Metallic Nanoparticles inside different Dielectric Matrices

Since the Antiquity, the elders were already using metal nanoparticles, in particular noble metals, without even understanding the exact nature of these particles. Nowadays, noble metal nanoparticles still exhibit interesting chemical and physical properties, which are considerably different from the properties of the bulk material. One of them is the optical absorption band known as surface plasmon resonance (SPR), which originates from the collective oscillation of the conduction electrons when they are excited by a light wave [1, 2]. The physical phenomenon SPR is of practical interest in optoelectronics [3], optical devices [4], solar cells [5] and catalysis [6] or sensor development [7].

In this chapter, our attention is mainly focused on the photo-assisted organized growth of metallic nano-objects inside silica materials prepared by sol-gel routes. In this study, we aim to master the localization, the organization and the preparation of various nano-metals, such as Au, Ag and Cu nanoparticles embedded inside different dielectrics matrices.

In the first section, precipitations of Au and Ag nanoparticles inside a silica xerogel using laser irradiation and heat-treatment are described. The growth of Ag or Cu nanoparticles embedded inside a dense silica glass is then reported in the second section. Herein, are provided different precipitations methods, based either on laser irradiations or heat-treatments.

In addition, the effects of laser power and heating conditions on the optical response of the metallic nanoparticles are studied. Finally, in the last section, Cu -doped silica preforms and capillaries were obtained for the first time with the aim to use it in the core of a microstructured optical fibre (MOF).

IV.1. Precipitation of metallic nanoparticles inside a silica xerogel

IV.1.1. Embedding of Au nanoparticles inside a silica xerogel

IV.1.1.1. Experimental conditions

The colorless free-of-cracks silica monoliths were obtained using a sol-gel technique from tetramethylorthosilicate (TMOS) as already described in Chapter II (subsection II.1.2.1). Porous silica samples of mean pore diameter 5.4 nm, a specific surface area of 360 m^2g^{-1} and a pore volume of 0.49 $cm^3\ g^{-1}$ were immersed for 4 hours into an aqueous solution S1 or S2. While the

solution S1 was composed of the hydrogen tetrachloroaurate ($HAuCl_4$) as a gold precursor and sodium carbonate as an additive, the solution S2 contained $HAuCl_4$ only. In both solutions, the concentration of the gold precursor was $[HAuCl_4] = 0.02$ mol.L^{-1} and in S1, the molar ratio $[Na_2CO_3]/[HAuCl_4]$ was kept to 2. Then, the samples were taken out and dried at 50°C for several hours to remove solvents and to retain the precursor within the pores. The resulting doped xerogels are still transparent.

To localize the growth of the Au nanoparticles inside the xerogel, we have also used both a femtosecond laser and a visible continuous laser. The femtosecond irradiation experiments of the loaded silica samples were performed using a Ti:sapphire oscillator, followed by a regenerative amplifier producing 120 fs pulses at 800 nm with a 1 kHz repetition rate. The laser beam, with an average power of 25 mW corresponding to deposited energy density 1250 J.cm^{-2}, was focused on the samples through a 10× microscope objective with a numerical aperture of 0.30. The obtained spot, with a diameter estimated to 2 μm, was located inside the volume of the silica matrix (about 1 mm under the surface) and scanned transversely to the laser beam direction at a rate of 1 mm s^{-1}.

The visible continuous irradiation was realized using a micro-Raman set-up. The incoming 514.5 nm laser radiation was focused on the surface of the matrix, via a microscope objective ×10, giving a spot diameter of 10μm and with a translation speed of 1 mm/s. The incident laser power for the visible irradiation was 70 mW corresponding to a deposited energy 700 J.cm^{-2}. The threshold power required to create Au nanoparticles using visible irradiation is 21 mW independent from the impregnated solutions (S1 or S2) and their concentrations. In each sample, a tight grating structure was inscribed, covering a surface sufficiently large to be used in the subsequent characterization techniques. Such laser irradiation conditions have been chosen to avoid any macroscopic structural modification of the silica matrix.

In parallel, doped silica xerogels were submitted to heat-treatments at different temperatures. The threshold temperature to precipitate the CdS nanoparticles is about 120°C.

IV.1.1.2. Local precipitation of Au nanoparticles using pulse femtosecond laser irradiation

Figure IV.1 shows the absorption spectra of the S1-doped silica xerogel irradiated by the femtosecond laser. One can note the appearance of an absorption band centred at about 537 nm (plot (b)) in comparison with the non-irradiated area (plot (a)). This band can be assigned to the SPR of gold nanoparticles in a silicate glass [8].

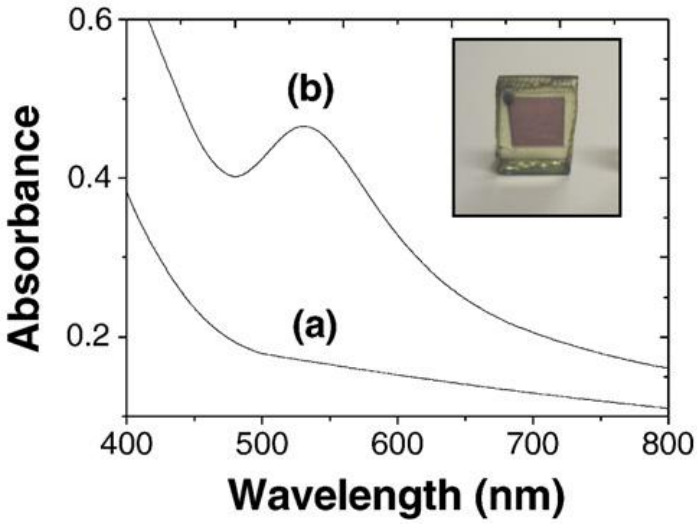

Figure IV. 1 *Optical absorbance spectra of an S1-doped silica matrix (a) non-irradiated area and (b) femtosecond laser irradiated area. Inset: photograph of the sample showing the irradiated area (colored portion).*

As shown in Figure IV.2 (a), transmission electron microscopy confirms that approximately spherical particles with a diameter between 50 and 60 nm, thus larger than the matrix pore size, are dispersed inside the irradiated area.

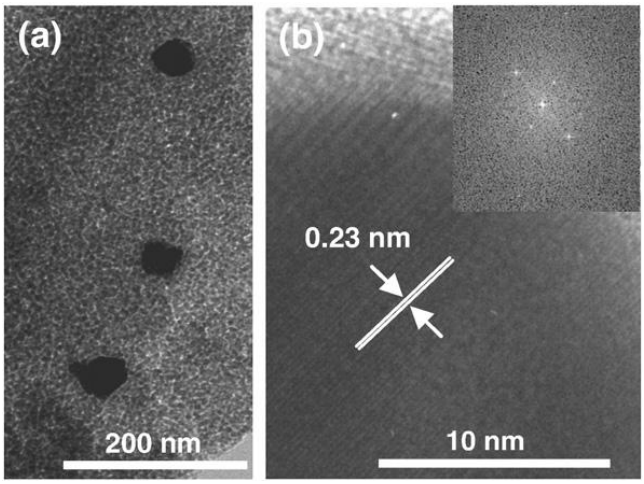

Figure IV. 2 *(a) TEM micrograph of the femtosecond laser irradiated area of an S1-doped silica matrix. (b) HR-TEM micrograph of a single particle in the irradiated area and the corresponding FTT shown in the inset.*

Moreover, the high-resolution TEM (HR-TEM) micrograph of a single particle (Figure IV.2 (b)) exhibits a fringe spacing around 0.23 nm in good agreement with the inter-planar distance between the (111) planes of "cubic" gold [9]. In the inset of Figure IV.2 (b), the Fast Fourier Transform (FFT) pattern of the HR-TEM micrograph clearly corresponds to the diffraction pattern of face-centred cubic-structured gold in the direction of (110) zone axis.

These results reveal the formation of crystalline gold nanoparticles after the femtosecond irradiation. The formation of gold nanoparticles larger than the pore size could be correlated to a fast diffusion of gold atoms, due to the presence of interconnected pores inside the silica host matrix, as it has been evidenced in a recent work. Hence, the growing of large Au nanoparticles is accompanied by the deformation and even the destruction of the silica pore walls in their vicinity [10]. Such a large size of the obtained nanoparticles may be inadequate for a number of applications because of the induced light scattering, especially in devices requiring a quantum size effect. However, by reducing the deposited mean power in the sample, the growth of smaller nanocrystals can be expected.

In recent works, the mechanism of formation of metallic nanoparticles in dense silicate glasses by femtosecond laser irradiation has been shown to involve the creation of non-bridging oxygen hole centers and E′ centers as sources of electrons [11, 12]. These electrons are consecutively trapped by the metallic ions, reducing them to metallic atoms and leaving a large amount of hole centers. Then, the aggregation of metallic atoms occurs during the high temperature heat-treatment. In the case of sol–gel samples however, the mechanism of electron generation is quite different. Experimentally, no gold nanoparticles were evidenced in the case of the S2-doped silica matrix after the femtosecond irradiation. Consequently, the presence of the additive (Na_2CO_3) is essential to yield the photo-precipitation of gold nanoparticles under the femtosecond irradiation at room temperature. The carbonate ion brought by the additive could play the role of electron donor. Indeed, an analogous molecule (Na_2SO_3) has already been used to initiate a metallic gold deposition on the surface of a glass substrate under UV irradiation from an aqueous solution containing $HAuCl_4$ [13]. In our work, Na_2SO_3 has not been used due to its high reactivity with hydrogen tetrachloroaurate in the aqueous solution, which leads to an unstable solution and impedes the impregnation of the silica matrix. On the contrary, the solution S1 is stable for several days.

Figure IV.3, showing the optical absorption spectra of the solution S2 (curve b), exhibits two absorption bands located at 230 and 310 nm, respectively.

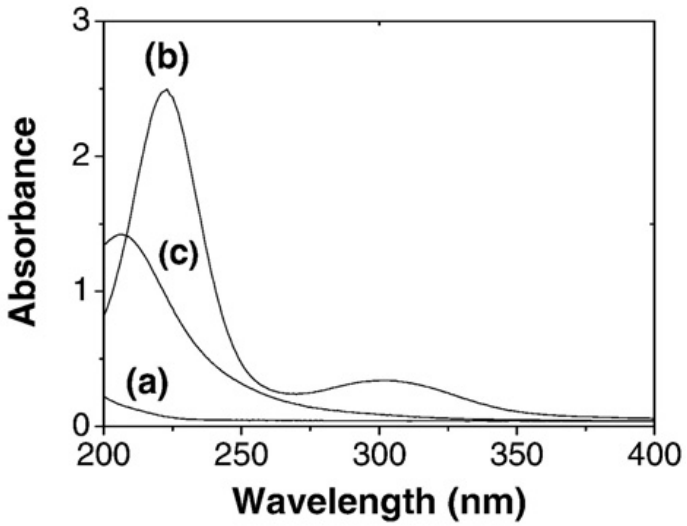

Figure IV. 3 *Optical absorbance spectra of an aqueous solution of Na_2CO_3 (curve a), S2 (curve b) and S1 (curve c).*

The band around 230 nm is attributed to the charge transfer of $[AuCl4]^-$ ions, and the band around 310 nm originates from the 5d transitions of the gold ions [14, 15]. Comparatively, the spectrum of solution S1 (curve c) presents only one absorption band centred at 207 nm. This could be ascribed to the formation of a gold complex with CO_3^{2-} anion. Such a formation of gold carbonate compound has been demonstrated previously [16]. Moreover, the use of sodium carbonate as a reducing agent has also been reported recently [17].

Under our experimental conditions, the temperature rise ΔT corresponding to 25 mW estimated to be 1142 K. This temperature, probably underestimated due to the nonlinear absorption effects, is sufficient to create locally and very shortly a melted zone or even a plasma, which expands into the surrounding volume, bringing the Au atoms to aggregate into nanoparticles [18]. It is to be noticed that such an instantaneous temperature, even multiplied by a factor 10 (in order to account for nonlinear effects), cannot be measured because the corresponding average temperature rise is about 2 K. But this quick and intense event is able to generate crystallized particles with diameters of several dozens of nanometres in one or two shots only. However, under these conditions, and in the absence of the additive, no gold nanoparticles have been evidenced. Thus, the presence of the additive is essential to obtain gold nanoparticles under femtosecond irradiations. Furthermore, since gold particles can grow in the silica xerogels with or without the additive under thermal treatment at 120°C (the precipitation will be shown in the next section of this chapter), a pure thermal photo-decomposition mechanism is not to be considered in the case of the femtosecond irradiation experiments. To explain the precipitation

of gold nanoparticles under the femtosecond irradiation in the presence of the additive, we propose a photo-electrochemical mechanism. This mechanism may include two principal steps. In the first step, a nonlinear multi-photon interaction with the carbonate groups occurs, in which photoelectrons are produced by the carbonate ions oxidation, which could lead to peroxodicarbonate anion and a hot plasma, according to the equation:

$$3CO_3^{2-} + nhv \longrightarrow 3/2\ C_2O_6^{2-} + 3e^- + Q$$

where n is the number of photons involved in the multi-photon process. Indeed, the existence of $C_2O_6^{2-}/CO_3^{2-}$ redox couple has been reported recently in the literature [19] and $K_2C_2O_6$ has been synthesized by anodic oxidation of potassium carbonate [20]. Then, the released electrons are trapped by gold ions, permitting their reduction into metallic atoms:

$$Au^{3+} + 3e^- \longrightarrow Au^0$$

Parallel to these reactions, the heat resulting from the hot plasma (Q) [18] increases the local temperature and promotes the diffusion of gold atoms. This diffusion, facilitated by the porosity of the silica matrix, allows the aggregation of the obtained gold atoms into nanoparticles.

IV.1.1.3. Local precipitation of Au nanoparticles using continuous laser irradiation

After irradiation of the S1-doped xerogel with a laser power higher than a threshold of 21 mW, it was visible to the naked eye that the color of the irradiated area changed from pale-yellow to dark red. For quantitative optical measurements, we chose a higher power of 70 mW, corresponding to a deposited energy of 700 $J.cm^{-2}$, in order to obtain a good compromise between a sufficient nanocrystals concentration and a correct optical transparency (insert of Figure IV.4 (a)). Figure IV.4 (a) shows the optical absorption spectrum of an irradiated area. The absorption band centred at 526 nm is assigned to the surface plasmon resonance (SPR) due to gold nanoparticles in a silica environment [21]. The XRD pattern of the irradiated area (Fig.IV.4 (b)) presents two reflexes at 38.4° and 44°, which can be indexed to the (111) and (200) lattice planes of cubic gold (JSPDS card, reference code 00-004-0784). The broad amorphous pattern at about $2\theta = 23°$ corresponds to the amorphous silica matrix. Accordingly, XRD analysis confirms the formation of gold nanocrystals inside the silica matrix. Their average size can be evaluated at about 14 nm from the reflex width by using the Scherrer equation [22].

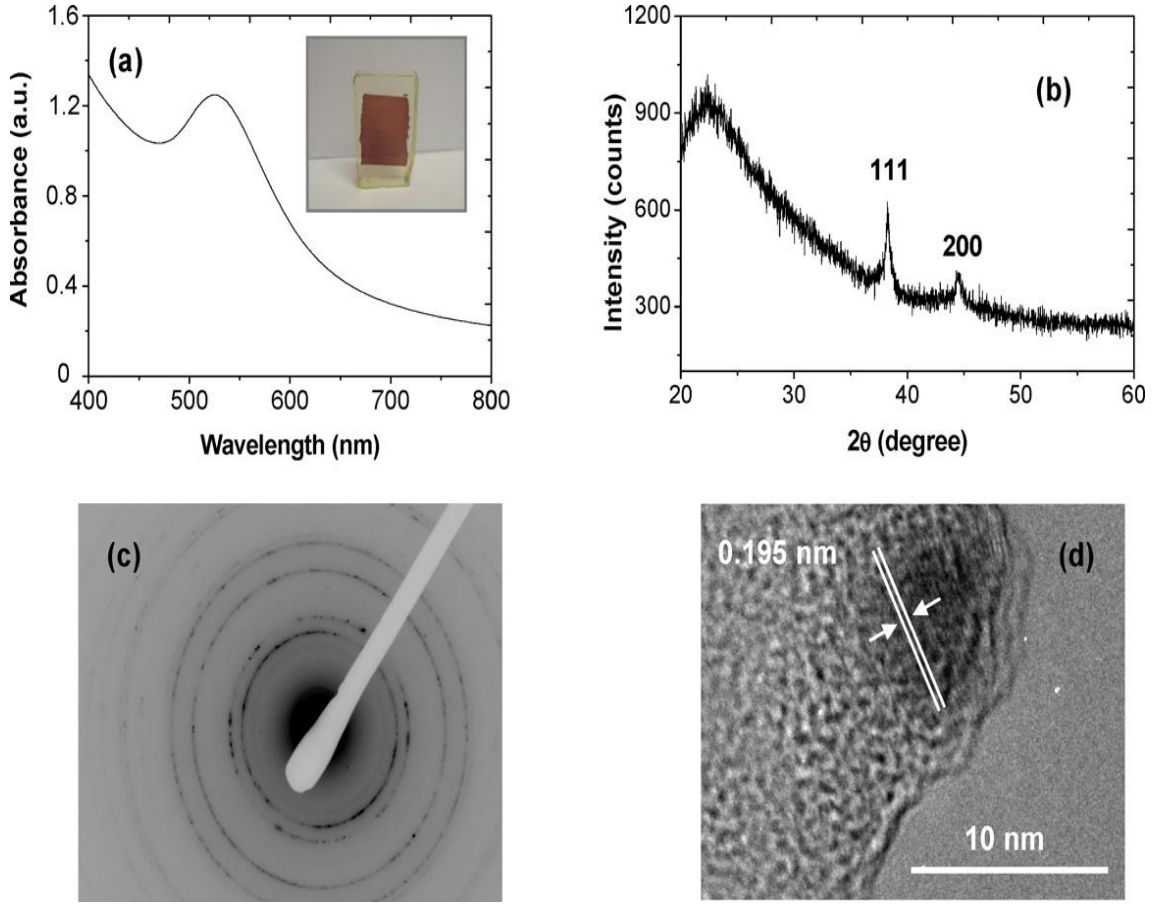

Figure IV. 4 *Characteristics of a S1-doped silica matrix taken in the irradiated area: (a) optical absorbance spectrum (insert: photograph of the sample showing the irradiated colored area, (b) XRD pattern, (c) TEM electron diffraction pattern, (d) HR-TEM micrograph of a single particle.*

TEM analysis has been performed in order to observe nanocrystallization inside the irradiated area of such a silica xerogel. The TEM electron diffraction pattern of the irradiated zone is shown in Figure IV.4 (c). As expected in the case of nanocrystals, the electron diffraction pattern shows a set of rings that can be indexed to (111), (200), (220), (311), (222), (400) and (331) planes of the cubic crystalline gold. The presence of rings instead of spots is due to the random orientation of the nanocrystallites. Moreover, the HR-TEM image of an individual crystallite was recorded in order to resolve the lattice planes. Thereby, the HR-TEM micrograph presented in the Figure IV.4 (d) shows an approximately spherical single particle with an inter-planar distance of 0.195 nm, which is close to the distance between (200) lattice planes of cubic gold (JSPDS card, reference code 00-004-0784).

In the case of S2-loaded samples, the power threshold for which coloration appeared inside the irradiated area was slightly higher (about 28 mW) than for the S1-loaded matrices. So as to compare both doping methods, the S2-doped xerogels were irradiated in the same conditions as

S1-doped ones, namely at ambient temperature and with an incident power of 70 mW. It is worthy to mention that the color of the irradiated area was dark purple (insert of Figure IV. 5(a)), that is different from the one obtained after the irradiation of a S1-doped matrix. In the Figure IV.5 (a) showing the optical absorption spectrum of the irradiated area, one can note the presence of a wide band centred on 549 nm. This band could be attributed to SPR of gold nanoparticles too [23]. The observed difference with the spectrum of the S1-impregnated sample might have its origin in the size dispersion of the generated Au particles.

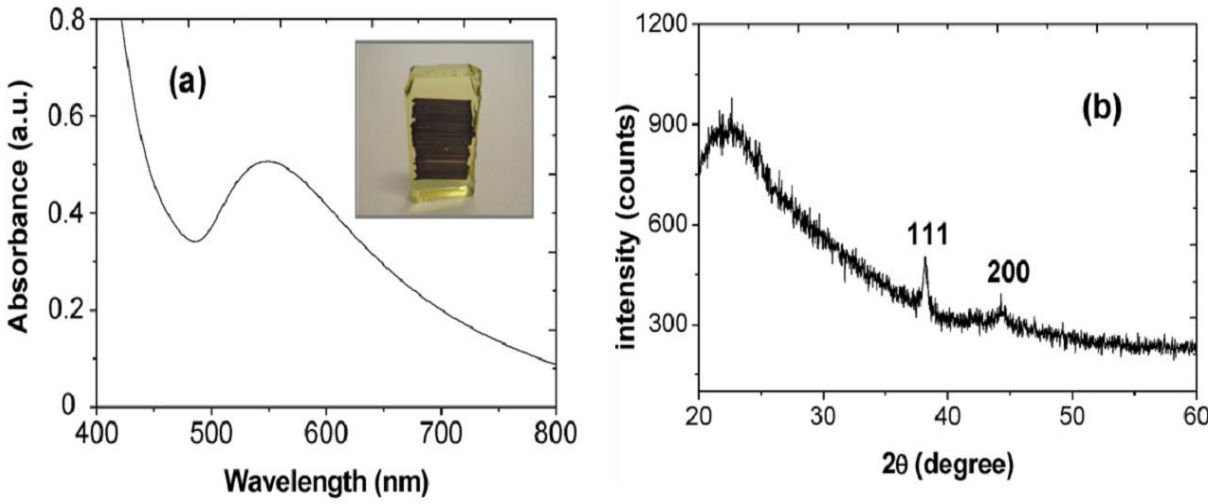

Figure IV. 5 *Characteristics of a S2-doped silica matrix continuous laser irradiated area: (a) optical absorbance spectrum, (b) XRD pattern.*

The presence of metallic gold in the S2-doped silica matrix irradiated by the continuous laser was confirmed by XRD analysis. As shown in Figure IV.5 (b), the diffraction pattern of the irradiated area exhibits the two reflexes for 2θ equal to 38.4° and 44°, respectively assigned to (111) and (200) lattice planes of the cubic structure of crystalline gold, like it was the case for the S1-loaded sample. The average crystallite size was estimated to 15 nm using Scherrer formula. Thereby, we have given rise to a very easy and practical method to fabricate nanoparticles in xerogels, based on a simple matrix impregnation followed by an irradiation using a conventional continuous laser.

By using this maskless technique, we carried out direct-writing of letters containing gold nanoparticles on doped silica monoliths at room temperature and using a laser power of 70 mW (Figure IV.6).

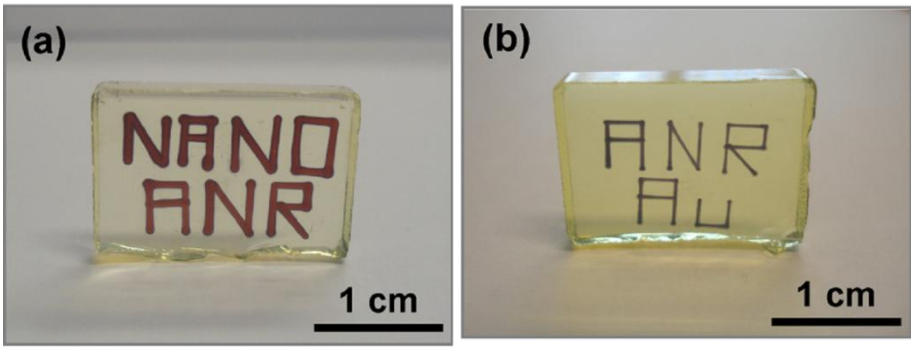

Figure IV. 6 *Photograph of the sample showing a direct-writing of gold nanoparticles inside (a) S1- and (b) S2-loaded silica monolith.*

In this example, the widths of the written lines were about 700 μm and 360 μm, corresponding to the doping with solution S1 and S2 respectively. However, this line thickness can be easily lowered down to about 20 μm by decreasing the doping concentration. Moreover, by decreasing the laser power, still thinner lines may be obtained.

In order to understand the mechanisms involved in the precipitation of gold nanoparticles under continuous laser irradiation, a silica xerogel loaded with gold precursors has been subjected to a heat-treatment in a furnace. As it is known, the decomposition of $HAuCl_4$ to yield metallic Au usually occurs in air at a temperature higher than 170°C, according to following reaction [24]:

$$2HAuCl_4 \rightarrow 2Au^0 + 2HCl + 3Cl_2$$

On the other hand, in a recent work, it has been shown that, due to the presence of silanol groups in the pore of mesoporous silica, this temperature was reduced to 80°C for 12h of heat treatment [25]. Au^{3+} ions reduction could occur under the surface-mediated reduction process as:

$$3 \equiv Si\text{-}OH + Au^{3+} \rightarrow 3 \equiv Si\text{-}O^- + 3\ H^+ + Au^0$$

Figure IV.7 (a) (solid line) shows the optical absorption spectrum of a sample doped with the solution S1 and annealed at 120°C for 30 mn. The SPR band of gold nanoparticles is detectable with its maximum centred at 540 nm. For the same sample, Figure IV.7 (b) presents the XRD pattern, which shows both reflexes at 38° and 44°, corresponding to (111) and (200) planes of metallic gold respectively. Using Scherrer formula, (111) and (200) reflexes yield a particle size around 15 nm.

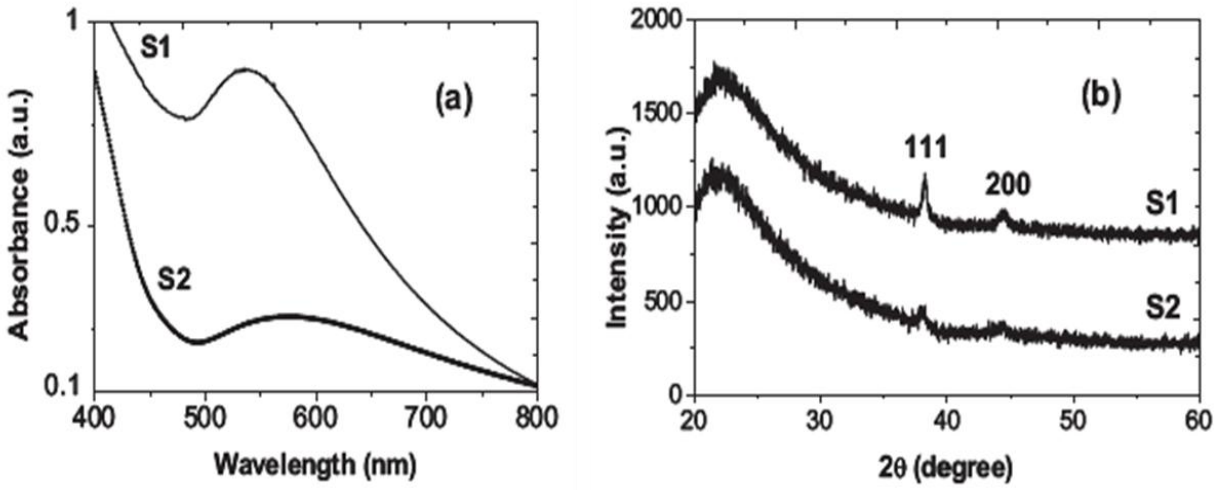

Figure IV. 7 *Optical absorbance spectra (a) and XRD patterns (b) of silica matrices doped with solutions S1 and S2, then heat-treated at 120°C.*

In the case of the S2-loaded sample annealed in the same conditions, the SPR band shown in Figure IV.7 (a) (dashed curve) is wider: the full width at half maximum (FWHM) is 1.5 times the one measured in Figure IV.7 (a) (solid line). This broadening is accompanied with a red-shift to the lower energies (the absorbance maximum wavelength is at about 578 nm). Such a phenomenon is usually ascribed to an increase in the mean size of large Au nanoparticles of diameter greater than 20 nm, when they are analyzed in solution or inserted in a glass [26]. However, the broad nature of the XRD peaks presented in Figure IV.7 (b) indicates that dimensions of the crystalline domains are probably small. Indeed, the average crystallite size calculated using the Scherrer equation is about 9 nm. Hence, the observed red-shift is not expected in this size range and is anyway contrary to most of the models based on the Mie theory, since it occurs for a decreasing mean size (9 nm instead of 15 nm).

Yet, the same kind of result has been already reported when the gold nanoparticles are dispersed within the pores of similar silica mesoporous xerogels [27, 28]. This red-shift behaviour of the SPR band for the smallest Au particles has been attributed to the increasing boundary coupling (interface interaction) between the Au particles and the silica pore walls, due to the predominance of surface dangling bonds.

The comparison between the results obtained under continuous laser irradiation and ones obtained by heat-treatment allows us to propose a photo-thermal mechanism for the gold nanoparticles formation, with or without the additive (Na_2CO_3). When exposed to a laser irradiation, the doped matrices absorb a small part of the photons energy and convert it into local

heat, leading to a temperature increase of several hundreds of degrees. A temperature of the order of 80°C is sufficient to activate the reduction of ionic gold and the diffusion of the obtained gold atoms to form gold nanoparticles [25]. Moreover, it has been shown that the presence of the additive promotes the formation of gold nanoparticles. This could be related to the formation of gold carbonate complexes [29], which decompose easily under laser irradiation and lowers the laser power threshold necessary to obtain gold nanoparticles.

IV.1.2. Embedding of Ag nanoparticles inside a silica xerogel

IV.1.2.1. Experimental conditions

Porous silica xerogels, as already described in Chapter II (paragraph II.1.2.1.), have been prepared and then immersed into solutions of silver nitrate ($AgNO_3$) or silver (I) hexa-fluoro-acetylacetanato (1.5-cyclooctadiene) (Aghfacac). The concentration of the aqueous solution of silver nitrate was equal to 0.02 $mol.L^{-1}$, whereas the concentration of the ethanol-based solution of Aghfacac was kept to 0.001 $mol.L^{-1}$ in order to avoid the absorption saturation due to silver precursors. Porous silica samples were soaked for 4 hours in the solutions, then taken out from the solutions and dried at 50°C for 1 hour. The visible irradiation was achieved using the micro-Raman set-up of a T64000 Jobin-Yvon spectrometer with a microscope objective ×10, giving a spot diameter of 10 µm and with a translation speed of 1mm/s. The threshold power necessary to create Ag nanoparticles using $AgNO_3$ is 28 mW independent from the concentration. This mean power corresponds to a deposited energy density of 280 $J.cm^{-2}$. On the other hand, in the case of (Aghfacac) precursors, the threshold power is 70 mW, corresponding to an energy density of 700 $J.cm^{-2}$. Hence, this difference could be explained by the fact that for the Aghfacac precursor there are several bonds to Ag atoms that need higher laser power to be broken (Figure IV.8)).

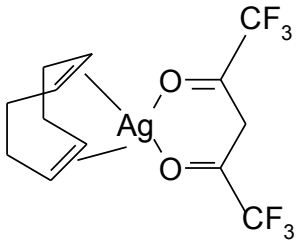

Figure IV. 8 *Empirical formula of silver (I) hexa-fluoro-acetylacetanato (1.5-cyclooctadiene)*

In each sample, a tight grating structure was inscribed, covering a surface sufficiently large to be used in the subsequent characterization techniques. To understand the formation mechanisms of

Ag nanoparticles, impregnated xerogels were also thermally treated at 120°C in an oven under air atmosphere.

Femtosecond irradiation experiments have been performed on the same kind of samples, but no formation of silver nanoparticles inside the silica xerogel has been detected in this case. When the silica doped silver ions were submitted to the femtosecond laser irradiation, no reduction of silver atoms was induced, and consequently no aggregation of silver nanoparticles was observed. In the case of gold nanoparticles precipitation inside silica xerogels using femtosecond irradiation, it was shown that the addition of photo-initiator is necessary. The same approach was followed for silver-doped xerogels but the addition of sodium carbonate to the impregnation solution led to rapid precipitation under mixing.

IV.1.2.2. Precipitation of silver nanoparticles inside a silica xerogel using visible continuous laser irradiation

IV.1.2.2.1. With $AgNO_3$ precursors

The absorption spectra of the undoped silica xerogels and the nitrate solution with 0.02 mol.L^{-1} have been added to Figure IV.9 for comparison. The nitrate solution and the doped silica xerogel with 0.02 mol.L^{-1} present an absorption band centred around 260 nm which attributed to the presence of silver ions [30]. The irradiation using continuous laser with an average power of 70 mW (energy deposited density 700 J.cm^{-2}) leads to a colour change in the irradiated area, from transparent to yellow, as shown in the inset of Figure IV.9.

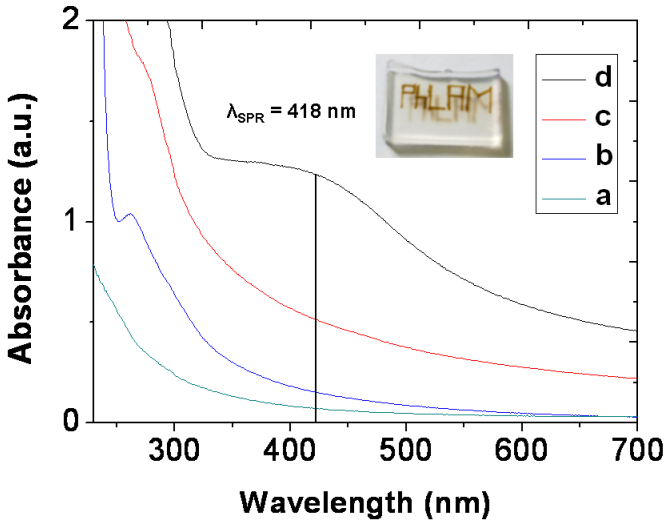

Figure IV. 9 *Absorption spectra of: (a) undoped silica xerogel, (b) silver nitrate solution of 0.02 mol.L^{-1} (c) non-irradiated area of silica matrix impregnated with 0.02 mol.L^{-1} nitrate solution and (d) 514.5 nm irradiation with 70 mW, Inset: Photograph of the irradiated sample.*

The absorption spectra of the irradiated area show a well-defined SPR band centred on 418 nm in the irradiated area. To confirm that this signature was due to Ag nanoparticles, the resulting colored zone was characterized using TEM analysis. The sample was irradiated with 70 mW and then grinded into a powder and deposited onto a copper grid previously coated with a thin carbon membrane. Figure IV.10 (left) shows a TEM image of the irradiated area. Approximately spherical nanoparticles have been observed. The HR-TEM of a single nanoparticle (Figure IV.10 (right)) exhibits a fringe spacing of 0.253 nm, in good agreement with the spacing distance d_{hkl} between the (111) lattice planes of cubic Ag (JCPDS No. 04-0783).

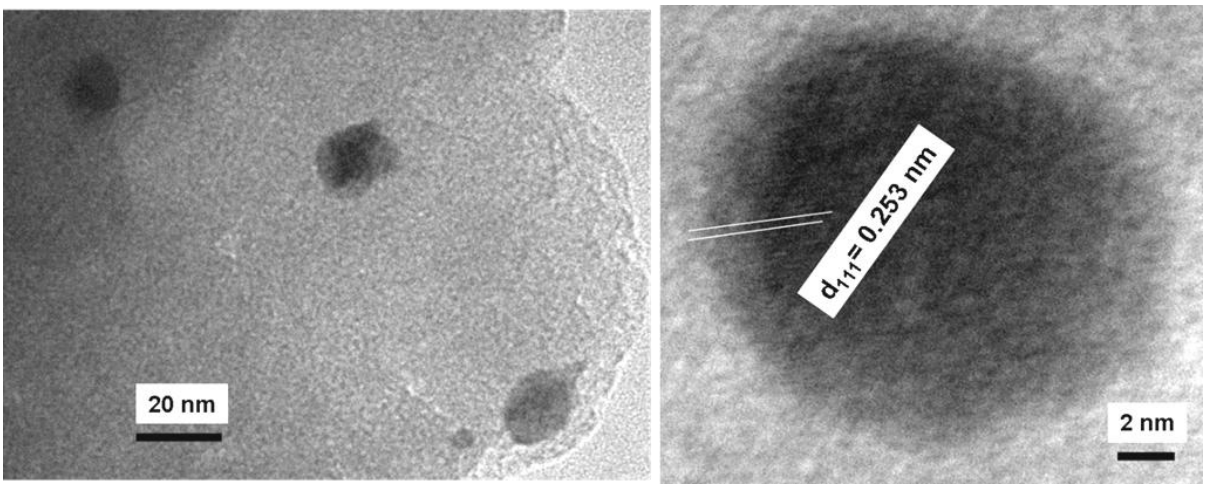

Figure IV. 10 *Left: TEM image taken in the irradiated area, Right: HR-TEM of a single nanoparticle.*

This result is consistent with the formation of crystalline silver nanoparticles after the visible continuous irradiation. As shown in Figure IV.10, the size of Ag nanoparticles can be larger than the mean pore diameter. As in the case of PbS nanoparticles (chapter III), this phenomenon could be explained by a fast diffusion process of silver atoms, due to the presence of interconnected pores inside the silica xerogel matrix, and to a rearrangement of silica network during the growth of silver nanoparticles [29, 31].

The formation mechanism of silver nanoparticles crystallization could be explained photo-thermally [29, 32]. We propose the following reactions which might occur during the irradiation process:

1- $SiOH + Ag^{+} \xrightarrow{h\upsilon} Si\text{-}O^{-} + Ag^{0} + H^{+}$

2- $Ag^{0} \xrightarrow{Q} (Ag)_n$

We assume that the reduction of metallic ions in an irradiated area is initiated by photon absorption of the visible continuous laser beam, which produces sufficient electrons in order to reduce the silver ions into atoms. Since the xerogel pores are interconnected, diffusion and aggregation of the metallic atoms are accelerated to form silver nanoparticles through the heating generated by the same photon absorption.

Silver nanoparticle was not the only compound generated upon irradiation using continuous laser irradiation. Silver oxide could also be formed, due to the reaction between Ag nanoparticles and the oxygen from the surrounding atmosphere. Figure IV.11 presents a HR-TEM image of a single oxide nanoparticle, with (111) lattice planes of Ag_2O (d_{111} = 0.273 nm, JCPDS cards 4-0783).

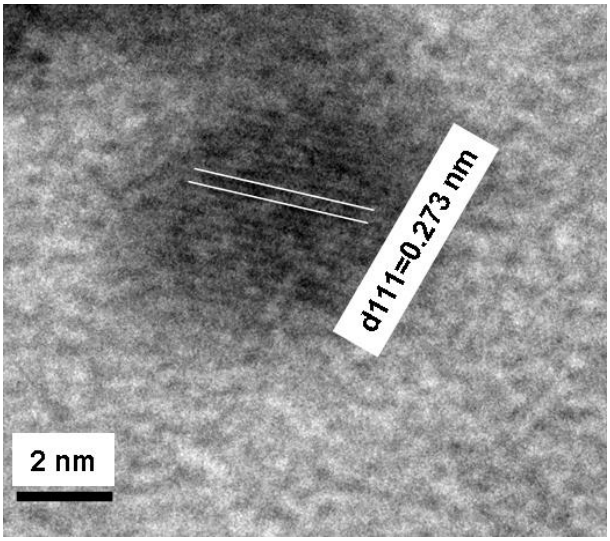

Figure IV. 11 *HR-TEM taken from a set of nanoparticles formed inside silica xerogel after laser irradiation with 70 mW.*

To study the influence of the average laser power on the optical response of the Ag nanoparticles, the doped xerogels with the $AgNO_3$ solution concentrated at 0.02 $mol.L^{-1}$ have been irradiated at different incident powers: 50, 70, 105 and 140 mW. These powers are corresponding to deposited energy densities of 500, 700, 1050 and 1400 $J.cm^{-2}$, respectively. The corresponding absorption spectra are shown in Figure IV.12.

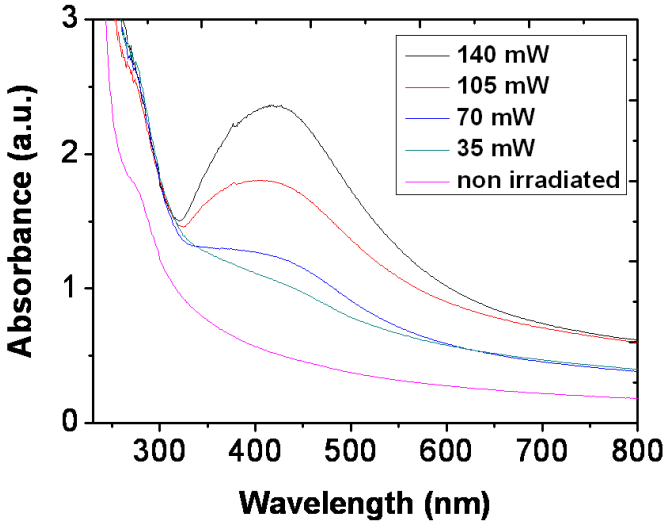

Figure IV. 12 *optical absorption of silica matrices impregnated with a $AgNO_3$ solution of 0.02 mol.L^{-1} and then irradiated with different incident powers: 140 mW, 105 mW, 70 mW and 50 mW.*

One can observe that the absorbance of Ag SPR (418 nm) increases with the incident average power. This effect is probably due to the reduction of the silver ions amount. This figure also shows that, the further irradiation does not lead to a shift in the absorption bands of the SPR Ag particles which indicate that the particle size remains unchanged.

IV.1.2.2.2. With silver (I) hexa-fluoro-acetylacetanato (1.5-cyclooctadiene) (Aghfacac) precursors

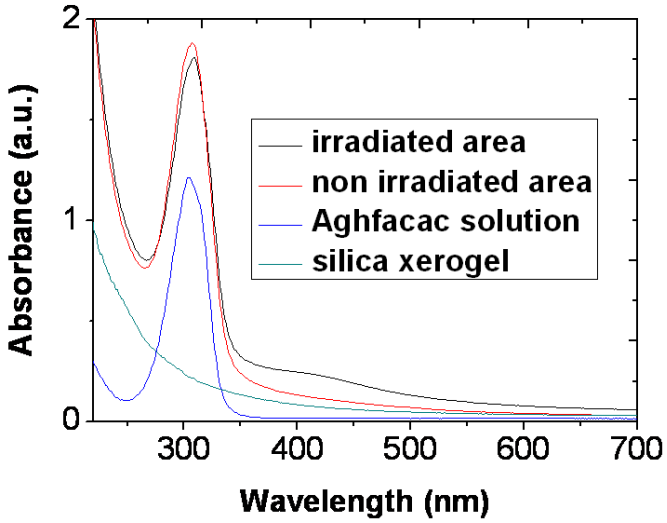

Figure IV. 13 *optical absorption spectra recorded in: the undoped silica xerogel (green), the Aghfacac solution with 2 x10^{-4} mol.L^{-1} (blue), the doped xerogel with Aghfacac solution of 10^{-3} mol.L^{-1} (red) and the continuous irradiated area with 70 mW (black).*

A single-step photo-assisted crystallisation of silver nanoparticles inside a silica xerogel has been also achieved using (Aghfacac) precursors. The impregnated silica was irradiated by the 514.5 nm beam in the same conditions as previously described (70 mW, focused on the sample surface using the ×10 objective). Figure IV.13 presents the optical absorption spectra recorded in the undoped silica xerogel, the Aghfacac solution with $2x10^{-4}$ mol. L^{-1}, the non-irradiated irradiated area and the irradiated area with 70 mW. A slight absorption band centred at 420 nm appears in the irradiated zone, as compared to the non-irradiated one. This is evidently assigned to the surface plasmon resonance (SPR) of silver nanoparticles in a silica environment. The absorption peak centred at 307 nm, attributed to the (Aghfacac) precursors [33, 34], undergoes a very slight decrease under laser irradiation, corresponding to a small release of precursors to the benefit of Ag nanoparticles.

IV.1.2.3. Precipitation of silver nanoparticles inside a silica xerogel using heat-treatment

IV.1.2.3.1. With $AgNO_3$ precursors

To understand the mechanisms involved in the precipitation of Ag nanoparticles under continuous laser irradiation, a silica xerogel loaded with a 0.02 mol.L^{-1} solution of silver precursors was subjected to a heat-treatment in a furnace at 120°C. The SPR band of silver nanoparticles was observed with its maximum at 425 nm after 1h of heating, as shown in Figure IV.14.

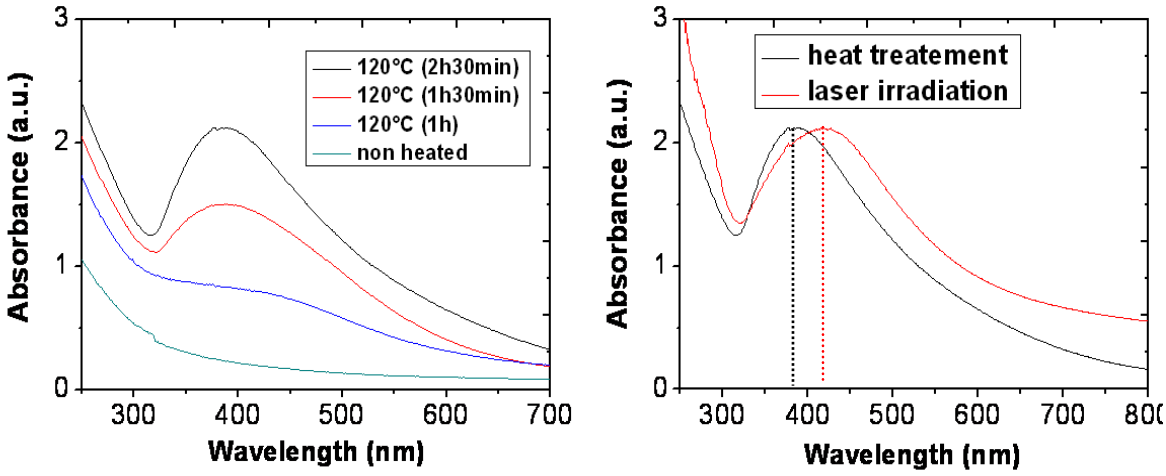

Figure IV. 14 *Left: optical absorbance spectra of doped silica matrix with 0.02 mol.L^{-1} heated at 120°C for different times. Right: doped silica matrix with 0.02 mol.L^{-1}, (black) heated at 120°C for 2h 30min and (red) irradiated with 140 mW.*

It can be noted that the increase in the Ag SPR absorbance as a function of heating time is accompanied by a blue-shifted down to 384 nm. This result suggests that together with a strong increase in the number of formed particles, their mean size is reduces and their size distribution becomes narrower. Such behaviour may be explained by the oxidation of the biggest nanoparticles [35]. Comparing to the heated samples at 120°C, the SPR band obtained in the 514 nm irradiation experiment (Figure IV.14 (right)) is slightly shifted to a longer wavelength (418 nm). This shifting in the SPR position indicates that the Ag nanoparticles within the silica xerogel have grown bigger using laser irradiation [35]. Hence, the temperature arising from the laser irradiation is likely higher than 120°C.

The presence of smaller Ag nanoparticles was confirmed by TEM measurements performed on the sample heated for the longest time (Figure IV.15).

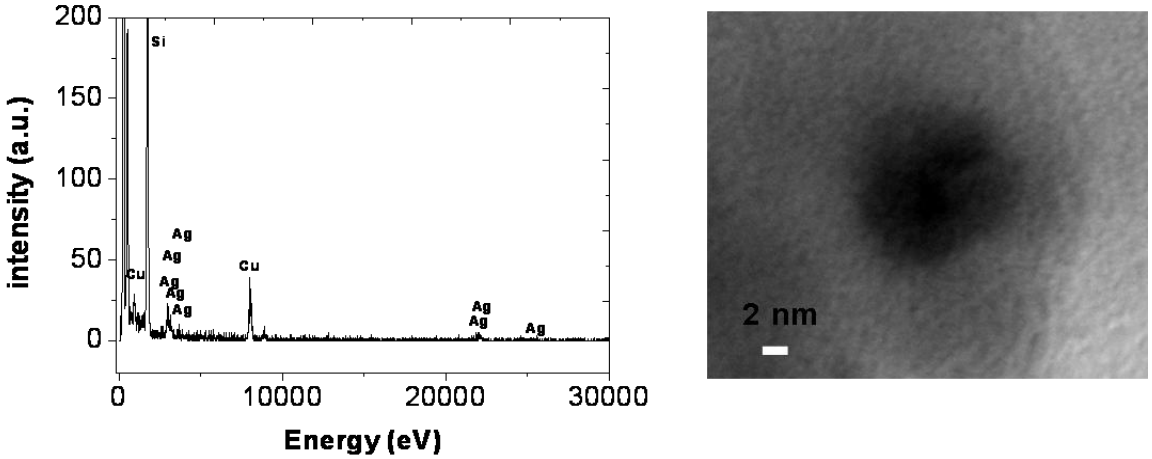

Figure IV. 15 *Left: Energy dispersive X-ray (EDX) spectrum obtained from the inset image. Right: TEM measurements performed on the sample heated for 2h30min at 120°C.*

In Figure IV.15 (right), a quasi-spherical particle with a size of about 8 nm can be observed. The EDX analysis confirms the presence of silver in silica (the peak for copper element came from the TEM grid and from the microscope itself).

IV.1.2.3.2. With Aghfacac precursors

Since it is difficult to observe the absorption band corresponding to the silver ions starting from the $AgNO_3$ solution, (Aghfacac) precursor was used. Figure IV.16 shows the optical absorption spectra recorded on the sample heated at 120°C for various durations.

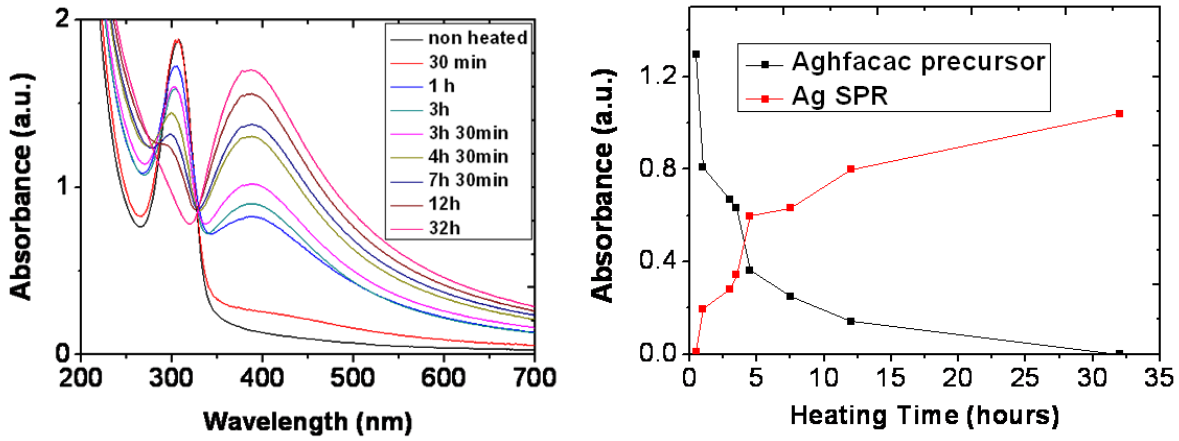

Figure IV. 16 *left: Optical absorption spectra of a xerogel doped with a 0.01 mol.L^{-1} Aghfacac solution, heated at 120°C for different times. Right: Calculated absorbance amounts of silver ions and Ag SPR as a function of heat-treatment time.*

The band around 305 nm, assigned to the (Aghfacac) precursors [33], strongly decreases while the absorbance of Ag SPR band increases. This confirms our suggestion about the thermal origin of the mechanism by which the silver nanoparticles are formed under laser irradiation (Section IV.1.2.2.1.). The absorbance for the (Aghfacac) precursor and Ag SPR were calculated and represented in Figure IV.15 (right). The heating threshold time needed to create Ag nanoparticles at 120°C was around 1 hour. The increasing in the heating time treatment rises the reduction of Ag^+ ions to silver atoms up to a heating time of 32 hours. At this heating time, the peak centred at 307 nm disappears that suggests a complete reduction of the silver precursors.

IV.2. Ag and Cu nanoparticles inside a dense silica glass

IV.2.1. Precipitation of Ag nanoparticles in silica glass

IV.2.1.1. Sample preparation

The synthesis of the doped dense silica glass matrix has been already described in Chapter II (paragraph II.1.2.2). Silver ion-doped sample was obtained from a silica xerogel impregnated with an alcoholic solution of a precursor: silver (I) hexa-fluoro-acetylacetanato (1.5-cyclooctadiene) (Aghfacac). This precursor has been chosen, instead of an aqueous solution of $AgNO_3$, due to its solubility in the alcoholic solution. A few hours later, the doped xerogel was densified under air atmosphere using a gradual increase of the temperature from room

temperature to 1200°C. In this case, a transparent silica glass matrix, doped with silver ions, was obtained. Before any characterisation, the obtained cylindrical glass rod was cut into small cylindrical pieces and polished to yield high optical transparency as shown in Figure IV.17 (inset picture).

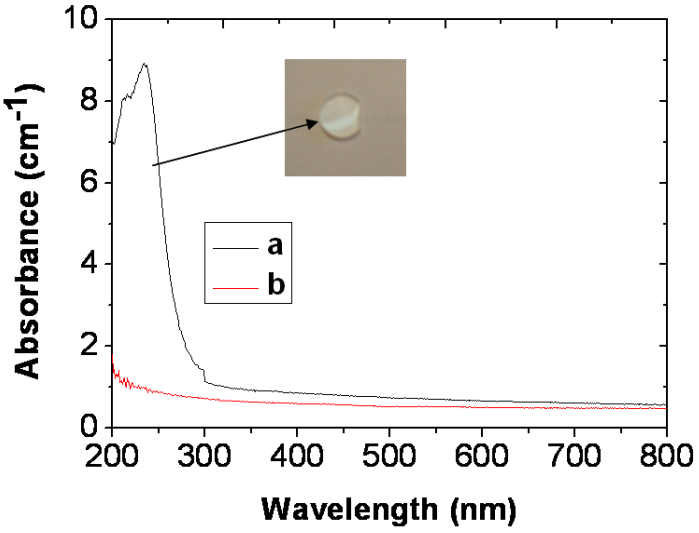

Figure IV. 17 *Optical absorption spectra of silica glass: (a) doped with Aghfacac solution and (b) non doped. Inset: a picture of the doped silica glass after annealing at 1200°C.*

Figure IV.17 reports the optical absorption spectra of doped and non-doped samples after annealing at 1200°C. None of both glasses present any absorption in the visible region, whereas two peaks appear in the UV region for the doped sample. These two peaks, centred at 234 nm and 213 nm, are attributed to the silver ions [34].

Precipitation of silver nanoparticles inside the silica glass matrix has been achieved using two methods: pulsed laser irradiation followed by a heat-treatment, or single heating under gas atmosphere. Detailed information about these methods is given in the following paragraphs.

IV.2.1.2. Silver nanoparticles in silica glass using pulsed laser irradiations

IV.2.1.2.1. Femtosecond laser irradiations

Irradiations using a femtosecond laser at 800 nm with different incident laser powers were performed inside the volume of the doped silica glasses. The incident laser powers were 10, 20 and 40 mW corresponding to deposited energy densities of 500, 1000 and 2000 J/cm^2, respectively. The irradiated zone showed a white diffusive colour, visible to the eye (see Figure IV.18).

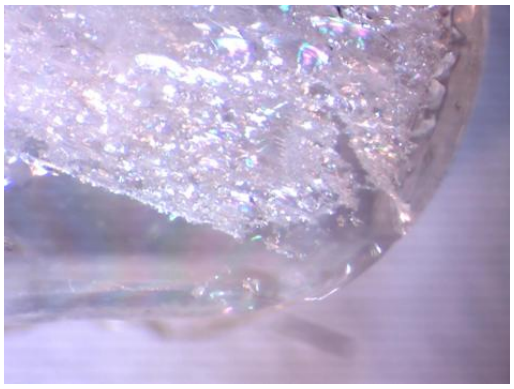

Figure IV. 18 *photo of the irradiated zone with average laser power of 40 mW.*

After heating the samples under air conditions at a temperature greater than 600°C (threshold temperature to create silver nanoparticles (see Figure IV.19-right)), the colour of the irradiated area turned to pale yellow, which was hardly visible to the eye and could not be recorded on a photograph.

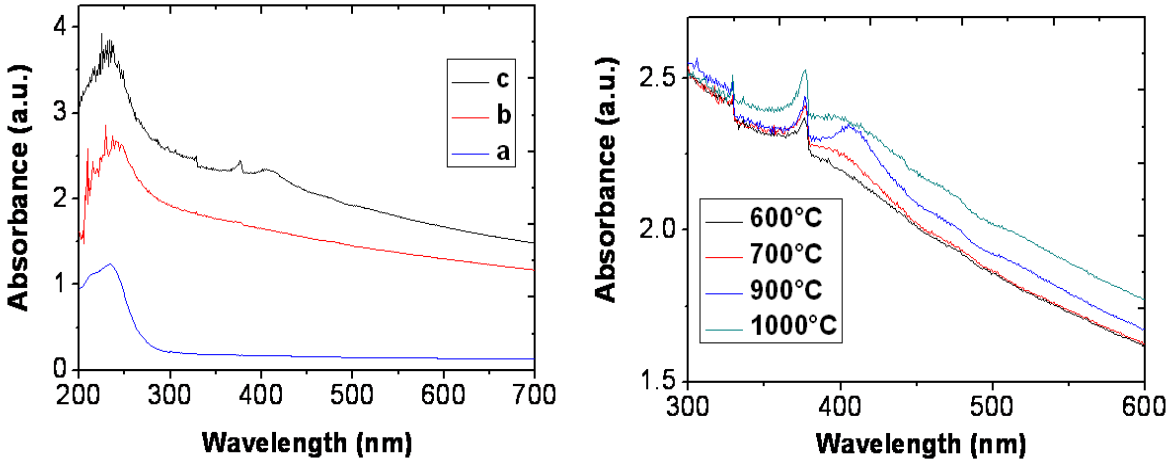

Figure IV. 19 *Left: Optical absorbance spectra of Ag^{+}-doped silica matrix, (a) non irradiated area, (b) irradiated area with 40 mW, (c) irradiated area followed by annealing at 900°C for 1h30min. Right: samples irradiated with 40 mW and annealed with different temperature.*

Figure IV.19 (left) reports the optical absorption spectra at different steps of the sample processing. After irradiation and before heat-treatment, no SPR band was observed, but the apparent absorbance of the irradiated zone increased considerably as compared to the unirradiated area. This apparent absorption, smoothly decreasing with increasing wavelength, is in fact ascribed to light scattering by the micro-defects generated under extremely high power densities. On the other hand, the Ag SPR, centred at 410 nm, was detected after annealing at 900°C for 1h30 min.

To study the influence of the heating temperature on the optical response of the Ag-nanoparticles, a doped silica sample was irradiated by 40 mW, and then annealed at different temperatures for 1h 30min. After heat-treatment at 600, 700, 900 and 1000°C, Figure IV.19 (right) shows that the absorbance level of the SPR band increased as a function of temperature to reach a maximum at 900°C. Hence, this temperature seems to be optimal for the Ag nanocrystals growth. The heat-treatment at 1000°C results in a broadening of the SPR band, probably due to the silver nanoparticles oxidation at high temperature.

To confirm the formation of silver nanoparticles in silica glass, XRD measurements were performed on the irradiated zones after heating at 900°C. Figure IV.20 exhibits no reflex from the silver nanoparticles and only a wide shape around 2θ = 22°, ascribed to the amorphous silica, appears. This absence of crystalline signature could be attributed to the weak concentration of the formed silver crystallites after irradiation and heat-treatment at 900°C, as can be deduced from the weakness of the SPR band in the absorption spectra of Figure IV.19.

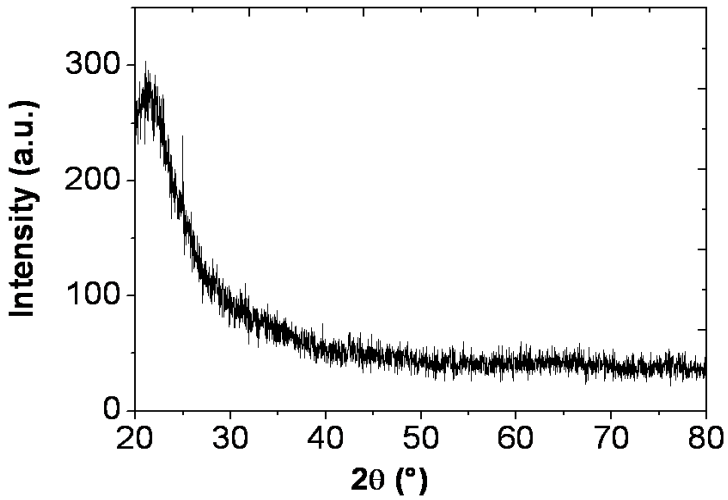

Figure IV. 20 *XRD figure of Ag^+-doped silica irradiated by femtosecond laser at 800 nm with 40 mW and heat-treated at 900°C for 1h30min.*

Since it was very difficult to characterize the formed nanoparticles by XRD or TEM measurements, and in order to get information about the nanoparticle size, this one has been roughly deduced from the SPR bandwidth using equation I.16 (see section I.2.1.1):

$$d = \frac{V_F}{\Delta\omega_{1/2}}$$

Where d is the diameter size of nanoparticles, V_F is the Fermi velocity of electron in bulk silver (1.39×10^6 m/s) and $\Delta\omega_{1/2} = 2c\pi\,(1/\lambda_1 - 1/\lambda_2)$ is the bandwidth at half-maximum (FWHM) in the

SPR absorption band. The so-calculated mean average diameter of Ag nanoparticles was about 4 nm after irradiation with a laser power of 40 mW.

The formation mechanism of silver nanoparticles embedded in a silica glass could be explained by the following reactions:

$$SiO_2 \xrightarrow{h\upsilon} \text{Silica defects} + e^-$$

$$Ag^+ + e^- \rightarrow Ag^0 \xrightarrow{Q} (Ag)_n$$

To study the influence of the average laser powers on the optical response of the Ag-nanoparticles, the doped sample were irradiated with three different laser powers, after annealing at 900°C. As can be deduced from the absorption spectra in Figure IV.21, for the used scan speed, the threshold power to create silver nanoparticles inside the silica glass lies between 10 and 20 mW. Moreover, the intensity of Ag SPR slightly increased as the power increased from 20 to 40 mW, indicating that the number of formed silver nanoparticles increased. On the other hand, the unchanged position of this SPR band suggests there is almost no variation of the mean particle size (about 4 nm).

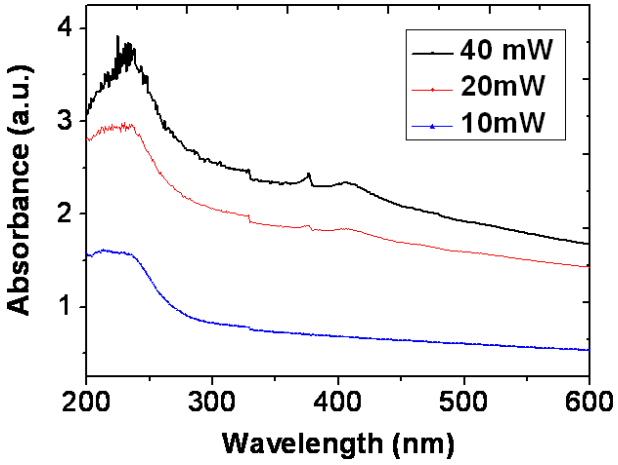

Figure IV. 21 *Absorption spectra of Ag^+-doped silica glass irradiated with different powers (10, 20 and 40 mW) and heated at 900°C for 1h30min.*

IV.2.1.2.2. Nanosecond excimer laser irradiations

The 193 nm pulsed beam from an excimer laser was used to irradiate silica glasses doped with silver ions. The focused laser beam, with an energy per pulse of 60 mJ, was 1.4 cm long and 300 µm wide. The energy density has been estimated to 1.4 $J.cm^{-2}$. A pale green line appeared at the surface of the sample, but it could not be recorded on a photograph. The laser beam was then

translated in order to cover a sufficient area for absorption characterisation. After that, the irradiated sample was brought to 620°C with a slope of 10°C/min and then kept at this temperature for 1h30min. Optical absorption spectra were recorded on a sample irradiated with 200 pulses and compared with non-irradiated samples, as shown in Figure IV.22 (left).

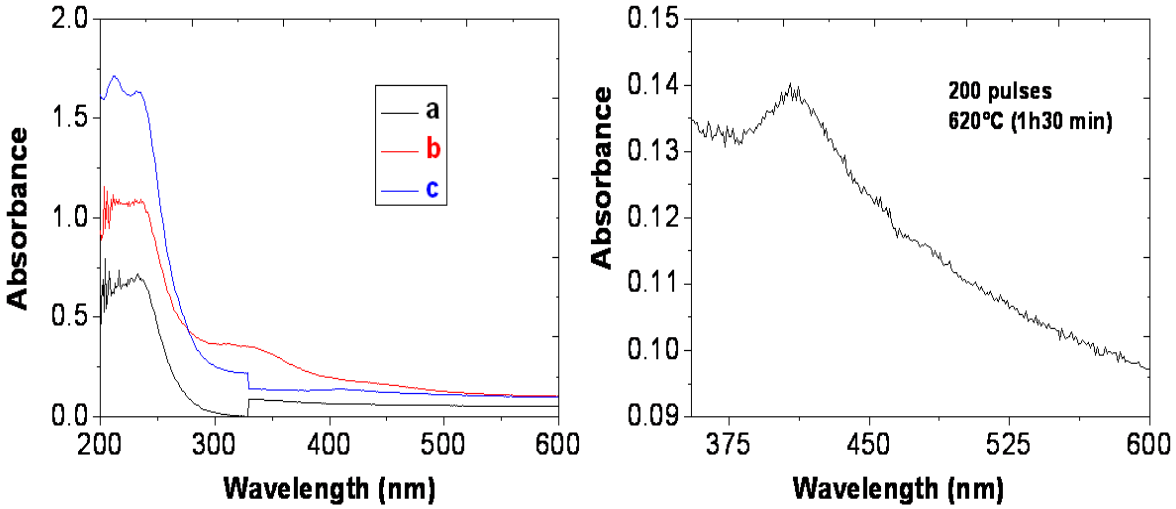

Figure IV. 22 *Optical absorption spectra of silica doped Ag. Left: (a) non irradiated sample, (b) irradiated with 200 pulses, (c) irradiated with 200 pulses followed by heating. Right: scale zoom spectra of irradiated sample with 200 pulses and heated at 620°C.*

Before heating, the irradiation leads to a global increase in absorbance and to the appearance of a new band that centred at 330 nm. This latter band could be assigned to atomic silver [34]. After heating at 620°C, this peak disappeared and the SPR band of Ag nanoparticles can be detected at 410 nm (Figure IV.22 (right). The weakness intensity of the SPR attests to the low concentration of the nanoparticles. For this reason, it was not possible to detect silver nanocrystals by XRD analysis or TEM measurements. Once again, equation I.16 was used to estimate the particle size from the SPR bandwidth. The obtained mean diameter 3 nm is of the same order as in the case of femtosecond laser irradiations.

Figure IV.23 shows the influence of the pulse number on the optical response of Ag nanoparticles created by irradiation at 193 nm.

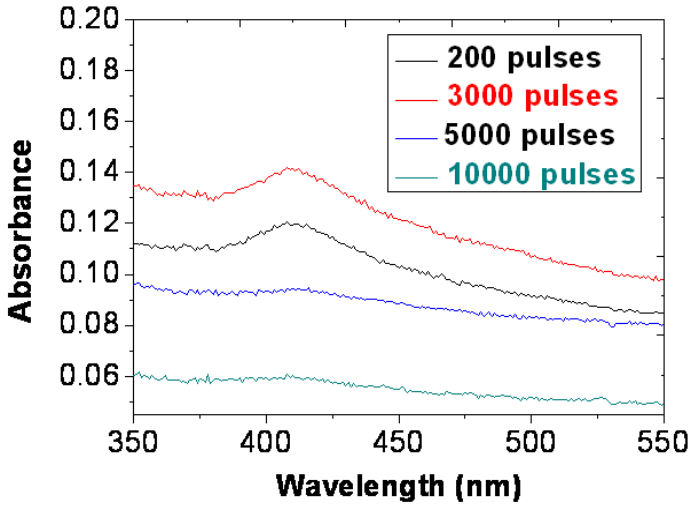

Figure IV. 23 *Optical absorption spectra samples irradiated with different pulses (200, 3000, 5000 and 10000 pulses) and heated at 620°C (1h30min).*

Between 200 and 10000 pulses, the SPR position does not shift, which means that the nanoparticle size remains more or less identical. On the contrary, the number of nanoparticles seems to decrease between 3000 and 5000 pulses. Hence, when silver ions were irradiated with a number of pulses less than 3000, the cumulative heat quantity is just sufficient to reduce silver ions into atoms and bring them together to form small nanoparticles. A higher pulse number probably results in too much heat generation, which makes it possible re-oxidize silver atoms.

IV.2.1.3. Silver nanoparticles in silica glass by heat treatment

IV.2.1.3.1. Using a blowlamp

Blowlamp fire generated from mixed oxygen and propane (C_3H_8) gas was used to heat the silica glass matrix doped with silver ions. The heating time was of about 60 seconds. The generated temperature was estimated between 1800°C and 2200°C. The colour of the heated sample turned yellow (inset of Figure IV.24). Figure IV.24 presents the optical absorption spectra recorded on the heated and on the unheated samples. The intense SPR band centred at 398 nm, assigned to silver nanoparticles, corresponds to the presence of high particles concentration at the sample surface.

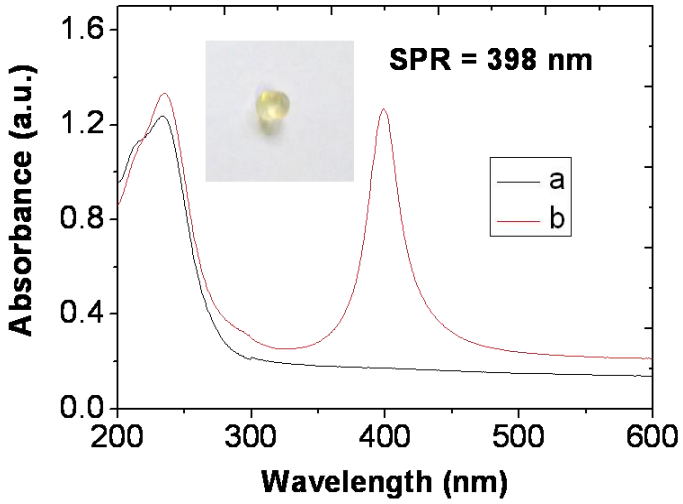

Figure IV. 24 *Photograph image of silica glasses doped with silver ions: (a) non heated sample, (b) sample heated by a blowlamp.*

The main products of the decomposition of C_3H_8 are H_2, C_2H_4, C_2H_2, CH_4, and C_3H_6 [36]. Hence, we suggest that the produced hydrogen (H_2) is at the origin of silver ions reduction, as shown in the following reaction [37]:

$$\equiv Si-O^{-}Ag^{+} + \tfrac{1}{2}\,H_2 \longrightarrow \equiv Si-OH + Ag^{0}$$

The temperature employed in this process is close to the melting temperature of silica, thus allowing a quick reduction of Ag^{+} ions and an efficient Ag atoms migration to form a great number of nanoparticles. Moreover, the yellow colour appeared only at the surface of the sample and not in the volume, since the silica glass is dense and thus prevents the produced hydrogen in the burner flame [36] to penetrate and diffuse rapidly inside the volume in order to reduce the silver ions. The formed nanoparticles were assumed to be spherical, and the size of Ag nanoparticles was calculated to be about 4 nm using Eq I.16. Apart from the novelty of the blowlamp method, which is a one-step method to obtain silver nanoparticles in a silica glass matrix at a high concentration, the interest of this study lies in the possibility to precipitate and to preserve silver nanoparticles at such a high temperature. This is promising for the achievement of silver doped-optical fibre core.

IV.2.1.3.2. Using hydrogen atmosphere

Hydrogen gas is known as an efficient reducing atmosphere. In a first step, a Ag^{+}-doped sample was heated under a 140 atm pure hydrogen atmosphere at 80°C for 2 weeks. After that, the hydrogenated sample was re-heated under ambient conditions at different temperatures ranging

between 100°C and 1200°C. The colour of the sample turned yellow after heating at 500°C for 1h 30min, as shown in the inset picture of Figure IV.25. This coloration is shared by the whole volume of the doped silica glass. In fact, after polishing the sample at different depths, we still observe this yellow coloration.

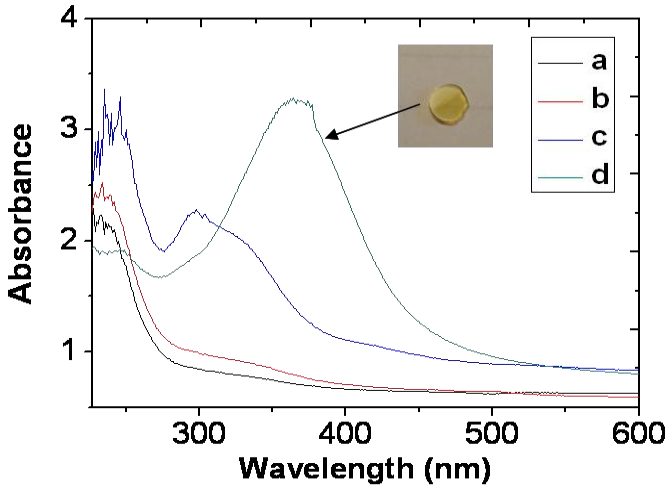

Figure IV. 25 *Optical absorption spectra of the hydrogenated silica glass doped with silver. Left: (a) non-heated, (b) heated under air condition at 100°C, (c) heated at 300°C and (d) 500°C. Inset: photograph image of sample heated under air condition at 500°C for 1h 30min.*

The absorption spectrum of the hydrogenated sample before heating in air condition, identical to the absorption spectra for the non hydrogenated silica glass, exhibits a band at 230 nm attributed to silver ions and a smooth shoulder around 330 nm, corresponding to atomic Ag^0 [34]. Heating at 100°C under air condition did not change the spectrum, but from an annealing temperature of 300°C, the peak at 330 nm became more intense, revealing a much larger amount of reduced species. Heating at 500°C leads to a beginning aggregation of the silver atoms into small clusters, as indicated by the presence of a silver SPR at 367 nm, attested by a considerably blue-shifted SPR band with regard to its normal position in silica (410 nm). This normal position is attained when the temperature is increased up to 900°C, as shown in Figure IV.26.

Moreover, the intensity of the SPR strongly increased with the heating temperature up to 1100°C. On the contrary, after annealing at 1200°C, the SPR band decreased, probably due to oxidation of Ag nanoparticles. Meanwhile, the SPR band divided into two sub-bands, the first one being centred at 390 nm and the second one at 450 nm. The appearance of these two peaks could be explained either by the formation of two different size distributions or by the formation of elongated shapes of silver nanoparticles, such as nanorods [38] (see chapter I.2.3).

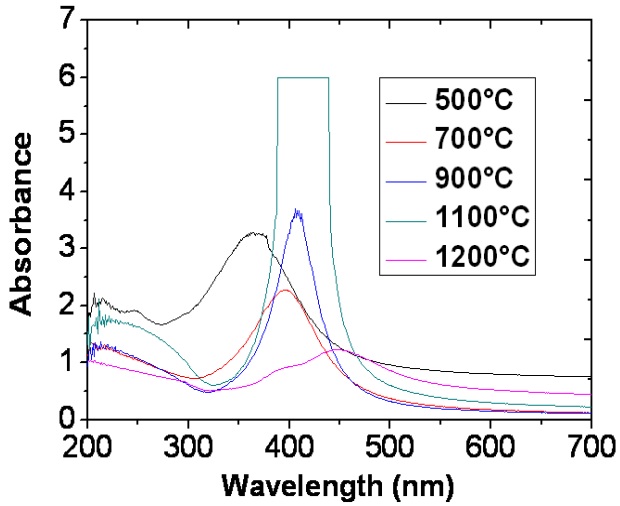

Figure IV. 26 *absorption spectra of the hydrogenated sample heated at different temperatures under air atmosphere.*

To confirm the formation of silver nanoparticles, and to explain the appearance of these two SPR position after heating at 1200°C, TEM measurements were performed on the samples heated at 1100°C and at 1200°C (Figure IV.27).

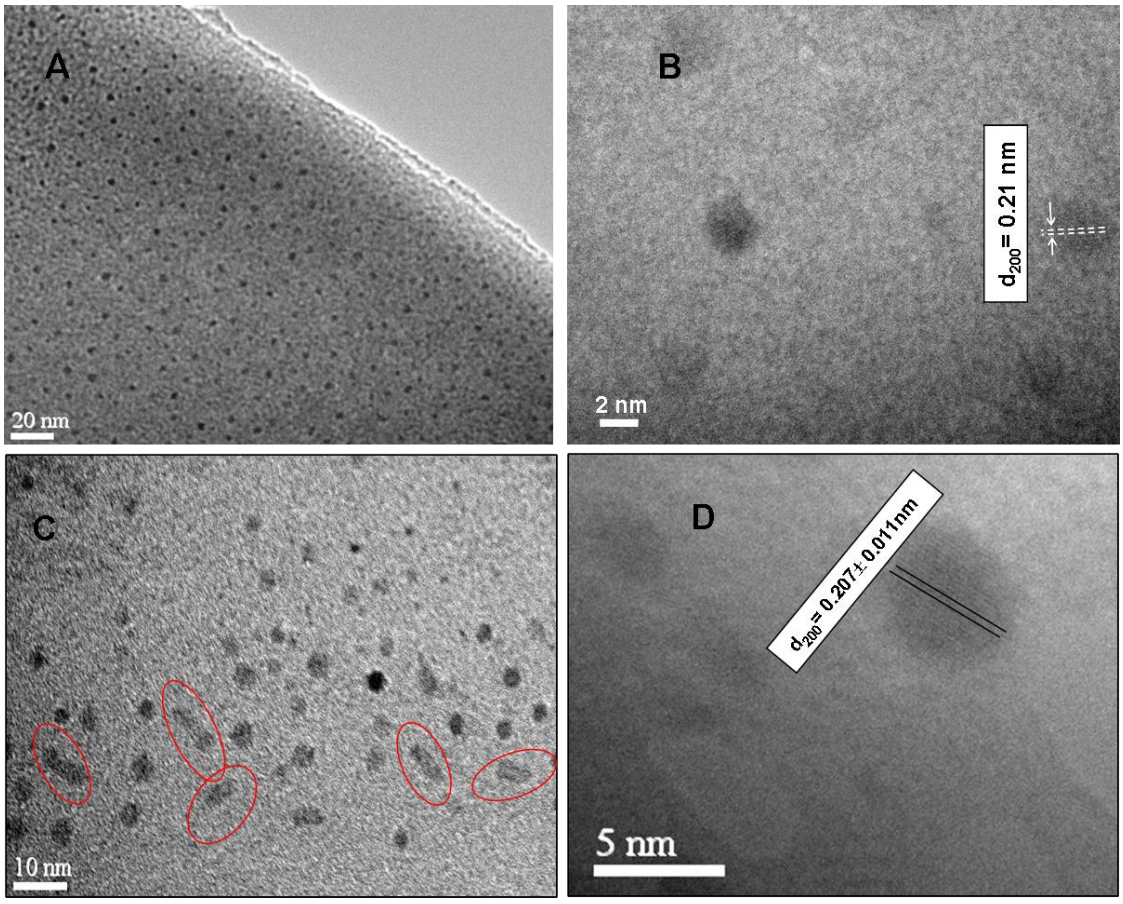

Figure IV. 27 *TEM measurements performed on hydrogenated silica doped with silver and heated at 1100°C (A, B) and 1200°C (C, D).*

Figure IV.27 (A) shows a TEM image of the heated sample at 1100°C for 1h30min.Quasi-spherical nanoparticles, with a size distribution ranging between 2 and 5 nm, were observed. IV.27 (B) presents an HR-TEM image of a single nanoparticle. The atomic interplanar distance has been measured around 0.21 nm, which are attributed to the (200) lattice planes of cubic Ag (d_{200} = 0.2044 nm, JCPDS cards 4-0783). In Figure IV.27 (C) showing the TEM image of the sample heated at 1200°C, spherical and non spherical nanoparticles with a size distribution ranging between 3 and 10 nm were observed. One can note that the nanoparticles associate to each other to give small rods. These non spherical nanoparticles could explain the observation of the two SPR bands in the absorption spectrum. In the HRTEM image of a single nanoparticle (Figure IV.27 (D)), the observed lattice planes (200) of Ag metal can be once again identified.

Furthermore, Eq (I.16.) was used to roughly estimate the size of the formed silver nanoparticles after each heating temperature from the SPR peak width. Table IV.1, presents the calculated sizes of silver nanoparticles upon the annealing temperature, showing the growth of the nanoparticles as function of the heating temperature.

Temperature	**500°C**	**700°C**	**900°C**	**1100°C**	**1200°C**
SPR position (nm)	**367**	**395**	**410**	**-**	**-**
Diameter (nm)	**1**	**1.6**	**2.7**	**-**	**-**

Table IV. 1 *Calculated sizes of Ag nanoparticles grown in silica glass after heat-treatment at different temperatures.*

Moreover, silver oxide has been also formed after heating at 1200°C for 1h 30min, due to the reaction between Ag nanoparticles and the oxygen from the heating atmosphere. Figure IV.28 presents a HR-TEM image of a single oxide nanoparticle, with (111) lattice planes of Ag_2O (d_{111} = 0.273 nm, JCPDS cards 4-0783).

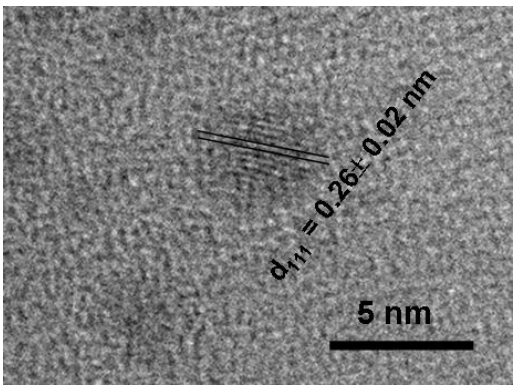

Figure IV. 28 *HR-TEM image taken from the sample heated at 1200°C.*

IV.2.2. Precipitation of Cu nanoparticles inside a dense silica matrix

IV.2.2.1. Sample preparation

As in the case of silver-doped silica glasses, a non transparent xerogel was obtained from the hydrolysis and condensation of tetraethylorthosilicate (TEOS) after various drying and annealing steps in air at 850°C. The obtained xerogel was impregnated in an alcoholic solution of copper (II) hexafluoroacetylacetonate hydrate. The impregnated sample was then densified at 1200°C so as to obtain a transparent cylindrical silica glass doped with copper ions (Figure IV. 29 (a)).

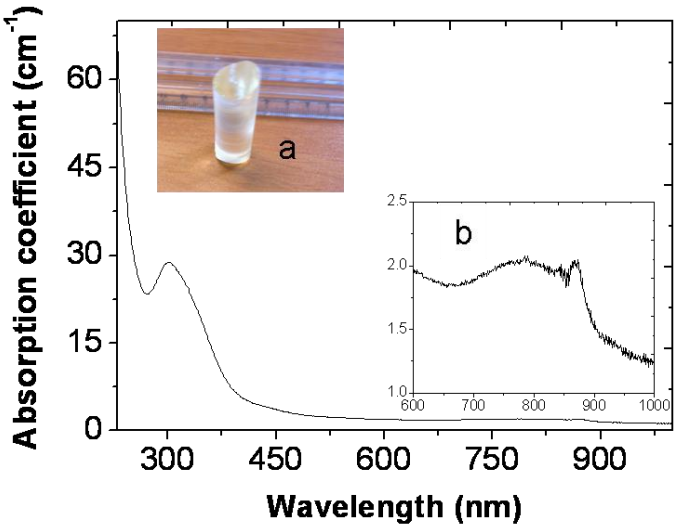

Figure IV. 29 *Optical absorption spectrum of silica glass doped with copper ions; Inset: (a) photograph picture of the glass sample, (b) a zoom scale of the absorption spectrum near 800 nm.*

Before any characterisation, the obtained cylindrical glass rod was cut into pieces of 1 mm thickness that were polished to get high optical transparency. The colour of the samples was yellow. The corresponding optical absorption spectrum exhibits two absorption bands at 303 and 800 nm. The peak centred at 303 nm can be related to Cu^{+} ions stabilized in the silica glass [39], while the lower and wide band around 800 nm is attributed to Cu^{2+} ions [40].

IV.2.2.2. Heat-treatment using a blowlamp

Approximately one minute blowlamp heating was applied to the surface of the doped silica glass. The colour of the sample changed from light green to red, as shown in the inset picture of Figure IV.30.

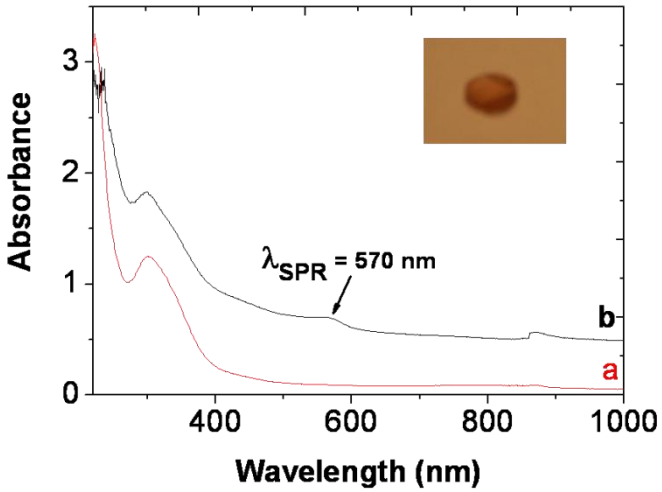

Figure IV. 30 *Optical absorption spectra of silica glass doped with ionic copper, (a) non-heated sample, (b) sample heated with a blowlamp.*

The red color appeared only at the surface of the sample and not in the volume of the silica matrix, since the polishing of the introduced sample to different depths led to a red color disappearing. This change of colour may be attributed to the formation of copper nanoparticles. Figure IV.30 shows the absorption spectra of heated and non-heated samples. The global absorbance level increased after heating due to light scattering by the silica defects generated under blowlamp heating, and the magnitude of the Cu^{+} peak decreased while a new peak appeared at 570 nm. This peak corresponds to the SPR of copper nanoparticles in a silica matrix [41]. The diameter size of the formed nanoparticles, calculated by Eq.(I.16), was of about 6 nm.

IV.2.2.3. Heat-treatment under hydrogen gas

Silica glasses doped with copper ions have been heated under a 140 atm pressure of hydrogen atmosphere for two weeks at 80°C. The color of the hydrogenated sample was pale yellow similar to the non hydrogenated sample (inset of Figure IV.31 (b). Then, the hydrogenated samples were heated under air atmosphere at different temperatures for 1h30min (temperature slope: 10°C/min) between 100 and 1100°C. The colour of the sample turned to red after heating at 700°C, as shown in Figure IV.31 (inset picture), but the red colour was not homogenous inside the sample. This inhomogeneity in the copper nanoparticle concentration may have two reasons: a higher concentration of ionic copper collected near the surface of the samples in the impregnation process and a possible higher amount of hydrogen diffused near the sample border as compared with its volume.

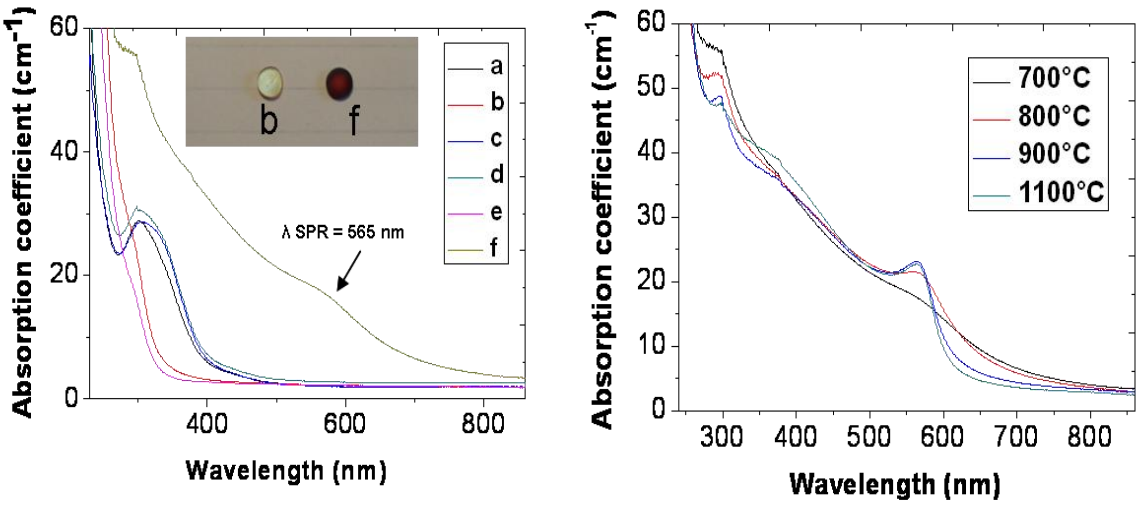

Figure IV. 31 *Left: (a) Absorption spectra of non hydrogenated doped silica, (b) hydrogenated sample doped with copper and heated at different temperature: (c) 100°C, (d) 300C, (e) 500°C and (f) 700°C. Right: Absorption spectra of hydrogenated sample heated under air condition at different temperatures for 1h30min.*

According to Figure IV.31 (left), the sample heated at 100°C under air condition shows approximately the same absorption spectrum as the non-heated sample. On the other hand, a heat-treatment at a temperature between 300 and 500°C led to a decrease in the absorbance of the Cu^{+} peak at 350 nm, likely due to the reduction of Cu^{+} into Cu^{0}. The band of the Cu^{2+} centred around 800 nm was also disappeared after heating at 300°C. The annealing at 700°C led to the formation of copper nanoparticles indicated by the apparition of a SPR band around 565 nm. When the annealing temperature was further increased (Figure IV.31 (right)), the maximum of the SPR band did not shifted, but it became narrower because of the increase in the nanoparticle size. Finally, heating at 900°C and 1100°C led to the formation of a new band around 400 nm, which can be related to the Cu_2O phase [42] (see Figure II.11 chapter II). The mean diameter of Cu nanoparticles after annealing at each temperature has been evaluated using Eq.(I.16) and summarized in Table IV.2.

Temperature (°C)	**700**	**800**	**900**	**1100**
Diameter (nm)	**3.3**	**4.3**	**5.6**	**5.6**

Table IV. 2 *Calculated diameter of Cu nanoparticles as function of heating temperature*

TEM analyses were performed on the sample heated at 900°C (Fig. IV.32). To this purpose, a sample was cut and polished to a 50 μm thickness and deposited on a molybden microscope grid. Then, an argon ion gas milling process allowed to obtain a thin area before a carbon film

was evaporated on it. Figure IV.32 (a) shows quasi-spherical nanoparticles with a size distribution ranging between 4 and 15 nm. Figure IV.32 (b) shows the EDX analysis recorded on the same area as in Figure IV.32 (a), confirming that the obtained nanoparticles contained Cu atoms. Ar and Mo element peaks were obviously due to the milling process and the grid, respectively.

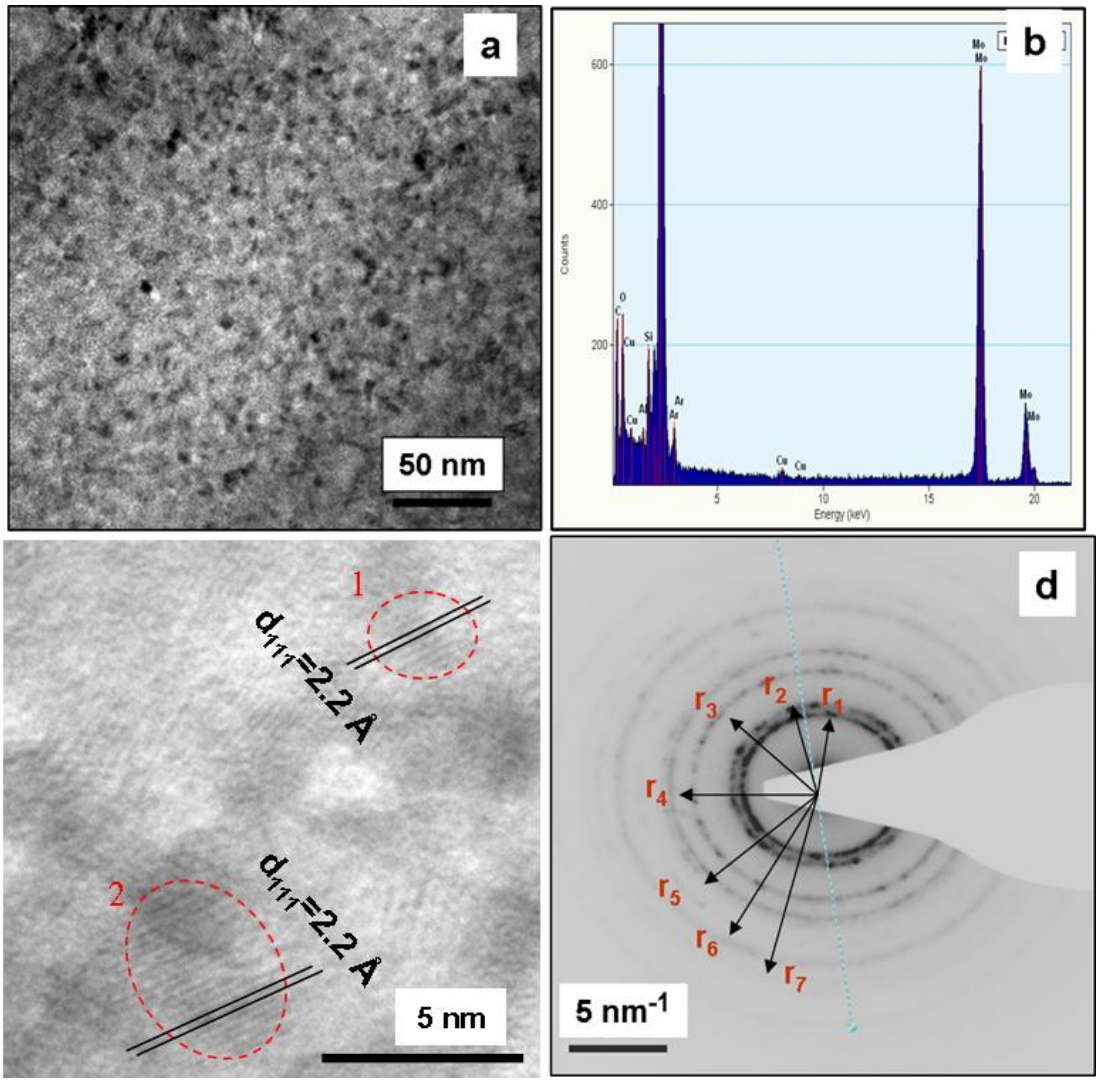

Figure IV. 32 *(a) TEM image taken from the sample heated at 900°C, (b) Energy dispersive X-ray (EDX) spectrum obtained from an ensemble of nanocrystals, (c) HR-TEM image of several Cu nanoparticles, (c) Electron diffraction image taken from a zone filled with nanoparticles.*

Figure IV.32 (c) presents a HR-TEM image of different nanoparticles. The analysis of the two circled zones gives an interplanar distance of (2.2 ± 0.1) Å, which can be attributed to the (111) lattice planes of metallic copper (d_{111} = 2.09 Å**,** JCPDS card no. 4-0836). In addition, Figure IV.32 (d) presents an electron diffraction pattern taken in a zone containing several nanoparticles. The estimated diffraction radii r_1, r_2, r_3, r_4, r_5, r_6 and r_7 correspond well to the Cu

lattice planes (111), (200), (220), (311), (222), (400) and (331) respectively. These results reveal the formation of copper nanoparticles inside the silica glass prepared by a sol-gel route.

However, copper oxide Cu_2O could also be formed after heating under air atmosphere at 900°C. Figure IV.33 presents an HR-TEM image taken from a set of nanoparticles. The interplanar distance of the zone denoted by circle correspond to d_{111} ~ 2.47 Å (JCPDS card no. 4-0836), expected for the copper oxide Cu_2O.

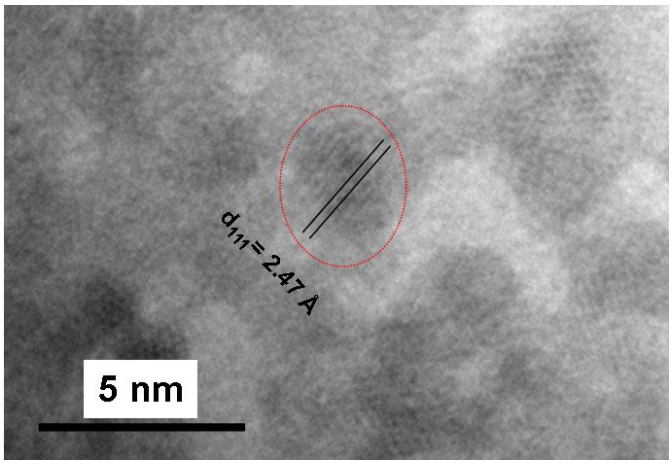

Figure IV. 33 *HR-TEM taken from a set of nanoparticles formed inside silica glass after heating at 900°C.*

IV.3. Cu nanoparticles inside the core of microstructures optical fibre

Two microstructured optical fibres (MOFs) were designed to receive a Cu-doped silica rod in its core with the aim of obtaining a strong interaction between waveguided light and copper nanoparticles. The fabrication of the MOFs was achieved using a stack and drawn method [43]. A first sol-gel-derived silica rod of centimetre length was doped with copper nanoparticles, while the second one was doped with ionic copper. The preparations of these preforms were already explained in IV.2.2.1.

IV.3.1. Drawing of a silica preform doped with Cu nanoparticles

Naturally, the aim is to keep the copper nanoparticles inside the doped rod at each step of the MOF fabrication. It is worthy to recall that the fibre fabrication process implies several steps including re-melting at temperatures as high as 2000°C. In order to take up the challenge of

preserving the particles in the glass in such extreme conditions, it was useful to study the influence of the initial copper nanoparticles concentration. To this purpose, two sol-gel silica glass rods of length 5 cm and diameter 0.5 cm, doped with ionic copper, were treated at 80°C under 140 atm of hydrogen gas using two different durations of hydrogenation: 2 weeks and 5 days. After that, the hydrogenated preforms were annealed at 900°C for 1h30min. Figure IV.34 (left) shows photograph pictures of the heated preforms. The hydrogenation for two weeks led to a dark, almost opaque colour, corresponding to a high concentration of copper nanoparticles. Meanwhile, the hydrogenation for 5 days led to a deep red colour in the volume of the preform.

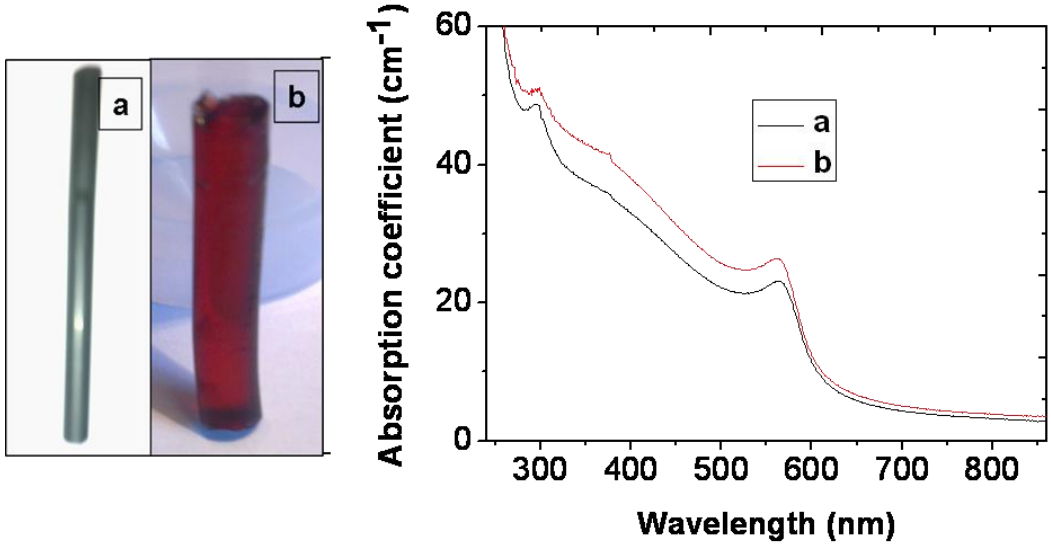

Figure IV. 34 *Visual aspect and absorption spectra of Silica rods doped with copper nanoparticles and heat treated at 900°C in air after being.(a): hydrogenated for 2 weeks.(b): hydrogenated for 5 days.*

Figure IV.34 (right) presents the optical absorption spectra recorded on two samples of 1 mm thickness taken from both rods. The SPR absorbance level increases with hydrogenation time, reflecting the number of nanoparticles. No spectral shift is observed between the two spectra, suggesting that particles remain small, whatever the hydrogen diffusion time is. The mean diameter of Cu nanoparticles has been estimated using Eq.(I.16), and it was 5.6 nm and 4.9 nm for the samples treated under hydrogen atmosphere for 2 weeks and 5 days, respectively.

To fabricate a MOF, smaller cylindrical rods of around 1 mm in diameter needed to be drawn at 2000°C from the initial rods. After this process, the thinner rods generated from the sample hydrogenated for 5 days showed an absence of copper nanoparticles (Figure IV.35 (a), due to the total oxidation of these ones at 2000°C. This oxidation is confirmed by the presence of the absorption band of Cu^{2+} (around 900 nm).

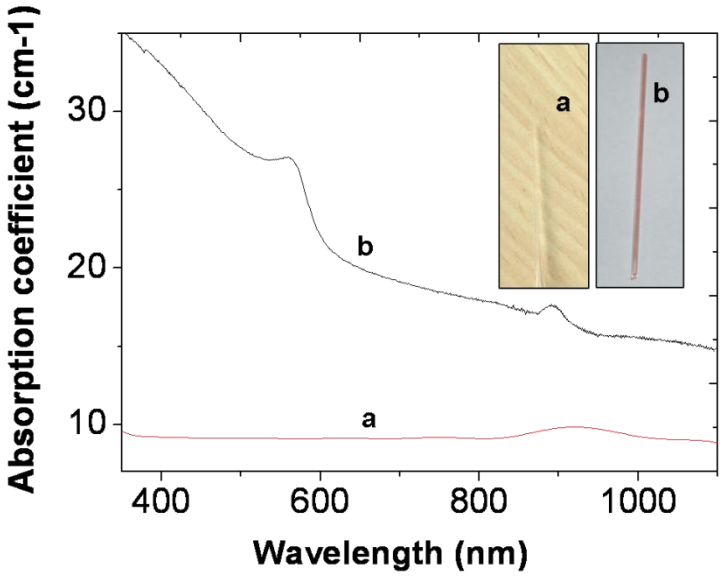

Figure IV. 35 *Optical absorption spectra and photograph images of the cylindrical rods, drawn into a thinner rod at 2000°C, generated from the rod hydrogenated for: 5 days (a) and 2 weeks (b).*

On the other hand, the drawing of the rod hydrogenated for 2 week, led to cylindrical thinner rods with a bright red color as shown in Figure IV.35 (inset picture (b)). The SPR band centred at 565 nm was observed in the absorption spectra, which attests to the presence of copper nanoparticles after drawing one time at 2000°C. The change of colour from deep red to bright red after drawing is also to be ascribed to a partial oxidation of copper nanoparticles.
This oxidation was confirmed by the large absorption band centred around 400 nm. The calculated absorption coefficients at the SPR maximum, before and after drawing were 0.9 mm^{-1} and 0.14 mm^{-1} respectively. Assuming the same absorption cross-section of Cu nanoparticles before and after drawing, such a decrease in the absorption coefficient by a factor 6 reflects a decrease in copper nanocrystal concentration after a heat-treatment at 2000°C.

The obtained small cylindrical rod was stacked with pure silica tubes in order to get the holey preform. Then, the ensemble was drawn into a cane and finally into a microstructure fibre. This means that the doped glass has been heated for 3 times at 2000°C before reaching the desired final fibred form. Scanning electron microscopy (SEM) image of the central region of the microstructured fibre is presented in Figure IV.36 (A).

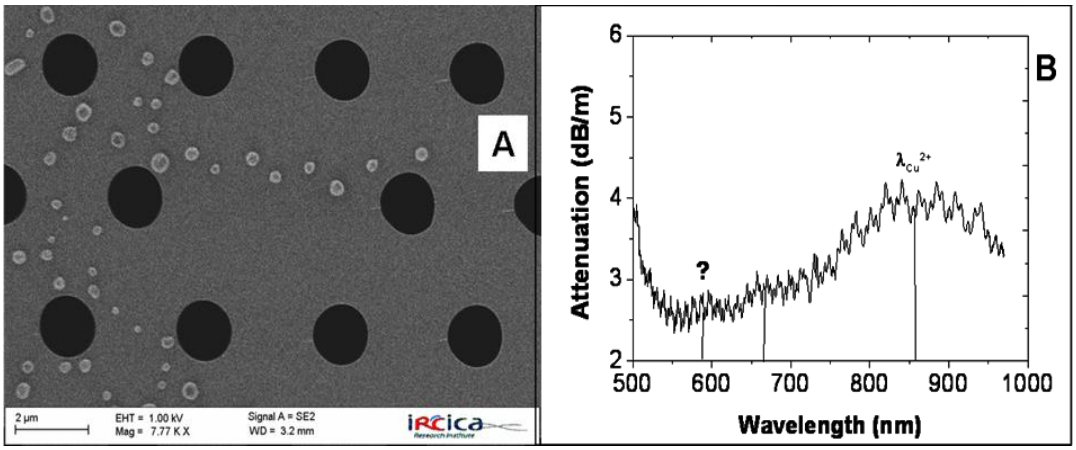

Figure IV. 36 *Scanning electron microscopy (SEM) image of the central region of the Cu-doped microstructured fibre. B: Attenuation spectrum of a 1 m-length piece of this microstructure fibre.*

The fibre has an outside diameter of 38 µm for a core diameter (defined as the distance between two diametrically opposite holes) of 5.4 µm. The pitch Λ of the periodic cladding and the diameter d of the air holes are 2.1 µm and 1.51 µm, respectively. The optical attenuation of this fibre was measured by the conventional cut-back technique using a super-continuum source (Fianium SC-400) and an optical spectrum analyzer (ANDO 6315).

Figure IV.36 (B) presents an optical attenuation spectrum obtained from the subtraction between the optical attenuation responses of a 3 m- and a 2 m-length fibre. Three attenuation bands, centred at 590, 667 and 855 nm, can be guessed in this attenuation spectrum. The peak centred at 855 nm may correspond to the presence of Cu^{2+} as previously shown [40]. The small peak around 590 nm could be assigned to Cu nanoparticles. However, one can note that the intensity of this peak is in the same order as the noise, and it is followed with another small peak around 667 nm. It is also clear that the band of the ionic copper is relatively higher than the one at 590 nm, which is compatible with an almost complete oxidation of the copper nanoparticles upon drawing at 2000°C.

Despite further development is necessary to preserve the Cu nanoparticlesin the optical fibre, this process allowed for the first time to fabricate a long microstructured fibre doped with Cu^{2+} starting from a silica preform. This result is very interesting in the application domain of the nonlinear optical devices since it has been shown that such a Cu^{2+}-doped fibre may exhibit Kerr effect 3 orders of magnitude higher than pure silica [44].

IV.3.2. Drawing of a silica preform doped with ionic copper

The same procedure as above has been applied, except for the hydrogenation that occurs at the end. First, a silica rod doped with ionic copper was prepared as described in paragraph IV.2.2.1. The diameter of this rod was reduced by a first drawing. Then, the MOF was obtained using the "stack and draw process". Figure IV.37 (A) presents a SEM image of the central region of the microstructured fibre. The outside diameter of the fibre is 38µm and the core diameter 6.19µm. The pitches Λ of the periodic cladding and the diameter d of the air holes are 2.3 µm and 1.42 µm, respectively. In Figure IV.37 (B) showing the optical attenuation spectrum recorded on 2m length of this fibre, a strong and broad band around 850 nm is ascribed to Cu^{2+}.

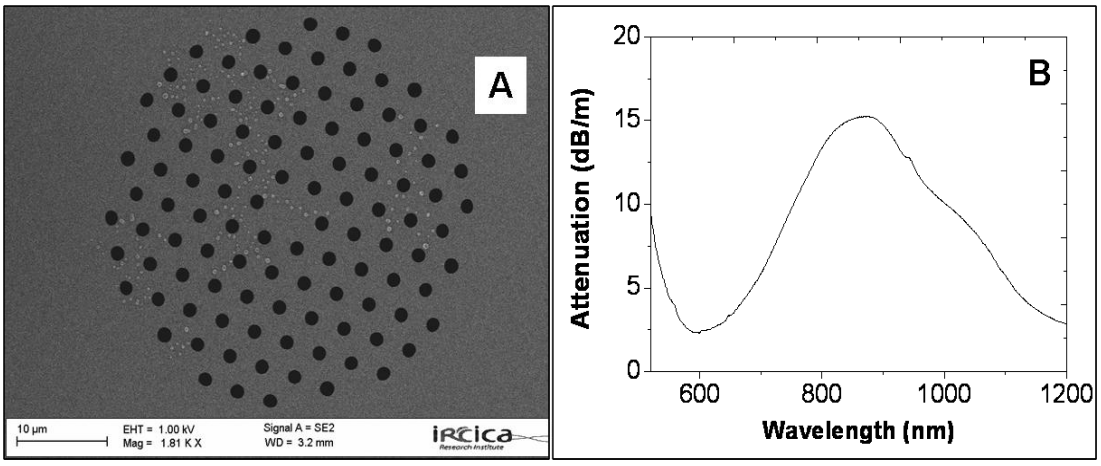

Figure IV. 37 *A: Scanning electron microscopy (SEM) image of the central region of the microstructured fiber obtained directly from the Cu^{2+}-doped rod and B: the corresponding attenuation spectrum measured on 2m-length.*

Subsequently, this fibre was heated at 80°C under hydrogen atmosphere for 5 days in order to reduce copper ions into atoms. Then, the fibre was heated under air atmosphere at 900°C for 1h30min with the aim of aggregating the atomic copper into nanoparticles. This heating led to the stripping of the MOF from its polymer layer, so that it became fragile. The resulting fragility prevented us from characterizing a long fibre.

Conclusion

In conclusion, a one-step method without any heat-treatment has been carried out for the space-selective growth of gold nanoparticles in bulk transparent sol–gel silica. This method, based on a femtosecond laser irradiation inside the silica matrix, allows a direct and localized growth of nanoparticles at room temperature. Experiments showed that the presence of the additive

(Na_2CO_3) is essential to generate the gold nanoparticles. A photo-electrochemical process has been proposed for the reduction of gold through the carbonate. By using a simple technique of post-doping and continuous laser irradiation, gold nanocrystals formation was localized under the surface of a silica xerogels, with or without the addition of (Na_2CO_3). The mechanism of nanocrystal growth is here essentially thermal, contrary to the femtosecond irradiation technique where photo-electrochemical processes had been identified.

Moreover, it has been shown that the Ag nanoparticles can be space-selectively precipitated in a porous silica matrix in a single step using a visible continuous irradiation. By comparison with a simple thermal treatment at 120°C, the formation mechanism of silver nanoparticles using a CW laser irradiation is found to be essentially photo-thermal with a temperature higher than 120°C. The size of the formed silver nanoparticles (10 nm) was greater than the pores in the sol-gel-derived silica matrix (6 nm).

Concerning the dense silica glasses, Ag nanoparticles could be precipitated using 3 routes. Firstly, the local precipitation was achieved using two different kinds of irradiation (with IR Ti:Sa femtosecond laser and with UV ArF excimer nanosecond laser) followed by annealing at temperatures greater than 600°C. Those methods result in Ag nanocrystals with diameter of about 4 nm. In the case of precipitation using heat-treatments, it was shown by TEM analysis that other crystal nano-phases (Ag_2O) were generated at high temperature. In addition, it was demonstrated that the size of the nanoparticles increased as a function of increasing heating temperature. The precipitation of Cu nanoparticles in dense glasses was achieved only by heat-treatment without any localisation. The formation of both copper nanoparticles and copper oxide nanoparticles (Cu_2O) was confirmed by TEM analysis.

Finally, copper-doped MOFs were achieved from sol-gel-derived rods in their core. By adjusting the initial Cu-nanoparticle concentration, the preservation of a significant part of copper nanoparticles inside the capillary was demonstrated after a first 2000°C heat-treatment. However, fibre-drawing implying 3 steps at 2000°C, led to the oxidation of all copper nanoparticles and resulted in a Cu^{2+}-doped fibre. The fabrication of a MOF starting from a silica rod doped with ionic copper seems a more promising method in order to obtain copper nanoparticles in the fibre core.

References

1. L.M. Liz-Marzán: formation and color 2004.
2. U. Kreibig, M. Vollmer. Optical Properties of Metal Clusters. Springer-Verlag, Berlin: 1995.
3. A.F. Koendernik, J.V. Hernandez, F. Robicheaux, L.D. Noordam and A. Polman. Nano Lett. **7,** 745 (2007).
4. S.A. Maier, H.A. Atwater. J. Appl. Phys. **98,** 11101(2005).
5. J.H. Lee, J.H. Park, J.S. Kim, D.Y. Lee, K. Cho. Org. Electron **10,** 416 (2009).
6. G. Schmid. Clusters & Colloids: From Theory to Application, VCH, Weinheim: 1994.
7. J. Hu, Z. Wang, J. Li. Sensors **7,** 3299 (2007).
8. A. Eremenko et *al*. Open access Book. Nanocomposites and Polymers with Analytical Methods, 2011.
9. JSPDS card, reference code00-004-0784.
10. M.T. Bore, H.N. Pham, E.E. Switzer, T.L. Ward, A. Fukuoka, A.K. Datye. J. Phys. Chem. B **109,** 2873 (2005).
11. J. Qiu et al. Angew Chem. Int. Ed. **43,** 2230 (2004).
12. S. Chen, T. Akai, K. Kadono, T. Yazawa. Chem. Commun. 2090 (2001).
13. A.U.S. Kumaran, M. Ichimura. J. Elect. Mater. **37,** 523 (2008).
14. K. Esumi, J. Hara, N. Aihara, K. Usui, K. Torigoe. J. Colloid. Interface. Sci. **208,** 578 (1998).
15. M. Quinn, G. Mills. J. Phys. Chem. **98,** 9840 (1994).
16. P.P. Weimarn. Bull. Chem. Soc. Jpn. **4,** 35 (1929).
17. C.Y. Kim, B.M. Kim, S.H. Jeonga, S.C. Yi. J. Ceram. Process Res. **7,** 241 (2006).
18. C. Zhao, S. Qu, J. Qiu, C. Zhu. J. Mater. Res. **18,** 1710 (2003).
19. J. Zhang, C.W. Oloman. J. Appl. Electrochem. **35,** 945 (2005).
20. R.E. Dinnebier, S. Vensky, P.W. Stephens, M. Jansen. Angew Chem. Int. Ed. **41,** 1922 (2002).
21. J. Gu, W. Fan, A. Shimojima, T. Okubo. J. Solid State Chem. **181,** 957 (2008).
22. A. Guinier, X-Ray Diffraction: In Crystals Imperfect Crystals, and Amorphous Bodies, Dover, New York: 1996.
23. W. Chen, W. Cai, L. Zhang, G. Wang, L. Zhang. J. Colloid Interface Sci. **238,** 291 (2001).
24. S.C. Chen, C.Y. Tang, Z.D. Yu, Important Inorganic Chemical Reactions. Science and Technology. Shanghai: p. 979, 1994.
25. C. Kan, W. Cai, C. Li, G. Fu, L. Zhang, J. Appl. Phys. **96,** 5727 (2004).

26. L.B. Scaffardi, N. Pellegri, O. De Sanctis, J.O. Tocho. Nanotechnology **16,** 158 (2005).
27. H. Shi, L. Zhang, W. Cai, Mater. Res. Bull. **35,** 1689 (2000).
28. W. Chen, W.P. Cai, C.H. Liang, L.D. Zhang, Mater. Res. Bull. **36,** 335 (2001).
29. H. El Hamzaoui, R. Bernard, A. Chahadih, F. Chassagneux, L. Bois, D. Jegouso, L. Hay, B. Capoen, M. Bouazaoui. Mater. Lett. **64,** 1279 (2010).
30. E.M. Govora and A.A. Revina. Colloids Surf. A. **168,** 87 (2000).
31. H. El Hamzaoui, R. Bernard, A. Chahadih, F. Chassagneux, L. Bois, D. Jegouso, L. Hay, B. Capoen, M. Bouazaoui. Nanotechnology **21,** 134002 (2010).
32. G.P. Shevchenko, S.V. Vashchanka, Y.V. Bokshits, S.K. Rakhmanov. J. Sol-Gel Sci. technol. **45,** 143 (2008).
33. A.P. Marchetti and G.L. Bottger. Phy. Rev. B. **3,** 2604 (1971).
34. B.G. Ershov, E. Janata, A. Henglein, A. Fojtik. J. Phys. Chem. **97,** 4589 (1993).
35. C. Sonnichsen, T. Franzl, T. Wilk, Plessen, J. Feldmann. New J. Phys. **4,** 93 (2002).
36. T.A. Cool, et *al*. P. Combus. Inst. **30,** 1681 (2005).
37. C. Mohr, M. Dubiel. H. Hofmeister. J. Phys. Condens. Matter. **13,** 525 (2001).
38. Y. Lu, Y. Wang, W. Chen. J. Power sources. **196,** 3033 (2011).
39. V.S. Gurin, A.A. Alexeenko, S.A. Zolotovskaya, K.V. Yumashev. Mater. Sci.Eng. C **26,** 52 (2006).
40. C. Silva, J. Coelho, A. Ruivo, A. Pires de Matos. Mater. Lett. **64,** 705 (2010).
41. O. A. Yeshchenko, I.M. Dmitruk. Phys. Rev. **75**, 085434 (2007)
42. O.A. Yeshchenko, I.M. Dmitruk, A.M. Dmytruk, A.A. Alexeenko. Mater. Sci. Eng. B **137,** 247 (2007).
43. R. Ramsay. Photonic-crystal fiber characteristics benefit numerous applications. SPIE 2008
44. A. Lin, B.H. Kim, D.S. Moon, Y. Chung, W.T. Han. Opt. Exp. **15,** 3665 (2007).

Conclusion and Outlook

In this thesis, we have used the sol-gel process to produce different silica matrices doped with different kinds of metallic and semiconductor nanoparticles. It has been shown that the sol-gel-derived silica materials, porous and dense glasses, provide convenient host matrices for a variety of inorganic compounds. Photo-assisted growth of metal and semiconductor nano-objects in silica materials constituted the framework of this thesis with the aim to master the localization and organization of theses nanoparticles. Different kinds of semiconductor (CdS, PbS) and metal (Ag, Ag and Cu) nanoparticles incorporated inside SiO_2 matrices have been investigated.

Semiconductor nanoparticles of CdS and PbS embedded inside sol-gel silica xerogels have been generated using laser irradiation at room temperature or using annealing under air atmosphere. Irradiations with a pulsed femtosecond (800 nm) laser or a 514.5 nm visible continuous laser have been performed on the silica xerogels post-doped with PbS or CdS precursors. It has been shown that the semiconductor nanoparticle size could be adjusted by choosing the concentration of precursors in the post-doping solution, the laser wavelength, the irradiation laser power and/or the temperature in the case of thermal precipitation.

In the case of both laser irradiations, a thermal effect mechanism at relatively high temperature (greater than 120°C) is at the origin of the laser-induced crystallization of CdS and PbS. Indeed, one can expect that under laser irradiation, heat is provided by light absorption from the dissolved precursors. This heating leads to the decomposition of the precursors in the irradiated zone and to the ions diffusion in the interconnected silica pores, resulting in semiconductors (CdS, PbS) nanoparticles growth in the silica matrix.

For both semiconductors, nanoparticles could be generated directly under the surface of the silica xerogels using a visible continuous laser or inside the volume of the matrix by femtosecond laser irradiation. This precipitation inside the volume plays an important role for the stability of these nanoparticles and especially in the case of PbS nanoparticles, due to their high ability to be oxidized under ambient conditions. It has been shown that this stability depends on the PbS nanoparticles formation conditions inside the silica xerogels, as well as on their mean size with respect to the pore diameter of the silica matrix.

Moreover, the precipitation of the semiconductor nanoparticles (PbS and CdS) could only be achieved inside porous silica matrices and not inside dense glasses. In fact, the densification of

doped silica xerogels at high temperature made it difficult to avoid the chalcogenide nanoparticles oxidation.

Silica xerogels also provide excellent host matrices for the formation of metallic nanoparticles. A single-step method, based on the irradiation of bulk transparent sol–gel porous silica with the IR beam from a femtosecond laser or with a visible continuous beam (Argon laser) without any heat-treatment, has been carried out for the space-selective growth of gold and silver nanoparticles. Experiments showed that the presence of an additive (Na_2CO_3) is essential to generate the gold nanoparticles using the pulsed femtosecond irradiation. On the contrary, the use of a continuous irradiation led to the formation of gold nanocrystals with or without the addition of Na_2CO_3. In the case of infrared femtosecond irradiation, a photo-electrochemical process, based on multiphoton absorption, has been proposed to explain the reduction of gold ions through the carbonate. As for the visible continuous irradiation, a pure thermal process has been identified. We also showed that Ag nanoparticles can be localized in a porous silica matrix under visible continuous irradiation. By comparison with a simple thermal treatment at 120°C, the formation mechanism of silver nanoparticles using a CW laser irradiation was found to be essentially photo-thermal with a temperature higher than 120°C.

Concerning metallic nanoparticles inside a dense silica glass, we have shown that Ag and Cu nanoparticles can be embedded through different routes. Three methods have been used to precipitate Ag nanoparticles:

- Space selective growth based on laser irradiation and followed with a heating step at high temperature (600°C).
- Direct heating using a blowlamp
- Heating using hydrogen atmosphere followed with annealing under ambient condition at a temperature greater than 600°C.

On the other hand, the growth of Cu nanoparticles in a dense silica matrix has been carried out thermally without any localization.

The local precipitation of Ag nanoparticles occurred under various pulsed laser irradiations: using the 800 nm line of a femtosecond Sa:Ti laser or using a 193 nm nanosecond ArF excimer laser together with a a subsequent annealing at a temperature greater than 600°C. The size of the formed particles was found to be around 4 nm with both irradiation processes. However, the concentration of the formed Ag nanoparticles obtained from both laser irradiations method was weak. The blowlamp flame, generated from mixed oxygen and propane (C_3H_8) gases, was also

used to heat a silica glass matrix doped with silver ions or copper ions. Apart from the novelty of the blowlamp method, which is a one-step method to obtain Ag or Cu nanoparticles in a silica glass matrix at a high concentration, the interest of this study lies in the possibility to precipitate and to preserve these nanoparticles at such a high temperature. This is promising for the achievement of silver or copper doped-optical fibre cores. In the case of precipitation using hydrogen atmosphere, it has shown that the nanoparticles can be preserved at temperatures up to 1200°C. By controlling the annealing temperature, we could control the size of metallic nanoparticles in a transparent material.

Besides this, the results obtained on the bulk matrices doped with copper nanoparticles have been applied to microstructured optical fibres prepared in our group with the aim to preserve the nano-objects in the core of such optical fibres. The characterisation of the capillaries obtained from the Cu-doped preforms after a first drawing at 2000°C actually showed the preservation of copper nanoparticles. However, the drawing at 2000°C for the second time led to a complete oxidation of copper nanoparticles.

To summarize, there are a number of ways in which the current work could be extended and improved. These outlook works could be presented as follows:

- to improve the stability of the PbS nanoparticles for a long duration by a deposition of a thin film of polymer in order to impede the penetration of the oxygen.
- to study the non-linear optical properties of metal and semiconductor nanoparticles embedded inside silica matrices.
- to reduce the dimensions of the nanoparticle patterns in order to design new optical devices.
- to localise the precipitation of the copper nanoparticles inside the silica matrices by hydrogenating the doped samples in order to reduce the ionic copper into atomic and then to irradiate it using a CW laser.

List of Figures

Chapter I

Chapter II

Chapter III

Chapter IV

List of Tables

Chapter I

Chapter III

Chapter IV

List of Publications

1- **Direct-write of PbS nanoparticles inside transparent porous silica monoliths using pulsed femtosecond laser irradiation.**
A. Chahadih, H. El Hamzaoui, R. Bernard, L. Bousseky, L. Bois, O. Cristini, M. Le Parquier, B. Capoen, M. Bouazaoui, Nanoscale Res. Lett. **6,** 542 (2011).

2- **Continuous laser irradiation under ambient conditions: a simple way for the space-selective growth of gold nanoparticles inside a silica monolith.**
H. El Hamzaoui, R. Bernard, A. Chahadih, F. Chassagneux, L. Bois, B. Capoen and M. Bouazaoui, Mater. Res. Bull. **46,** 1530 (2011)

3- **Continuous laser direct-writing of PbS nanoparticles inside transparent silica monoliths.**
A. Chahadih, H. El Hamzaoui, R. Bernard, L. Bois, O. Cristini, B. Capoen, M. Bouazaoui, J. Nanoparticles Res. **13**, 6507 (2011).

4- **Laser-induced direct space-selective precipitation of CdS nanoparticles embedded in a transparent silica xerogel.**
H. El Hamzaoui, R. Bernard, A. Chahadih, F. Chassagneux, L. Bois, D. Jegouso, L. Hay, B. Capoen and M. Bouazaoui, Nanotechnol. **21,** 13402 (2010).

5- **Room temperature direct space-selective growth of gold nanoparticles inside a silica matrix based on a femtosecond laser irradiation.**
H. El Hamzaoui, R. Bernard, A. Chahadih, F. Chassagneux, L. Bois, D. Jegouso, L. Hay, B. Capoen and M. Bouazaoui, Mater. Lett. **64,** 1279 (2010).

List of Conferences

1- **Photo-croissance de nanoparticules métalliques et semi-conductrices dans des matériaux diélectriques**
A. Chahadih, H. El Hamzaoui, R. Bernard, O. Cristini, B.Capoen, M.Bouazaoui. JFLPI, 18-21 Octobre 2011, Villeneuve d'Ascq, France.

2- **Lasers Direct-write Metallic and Semiconducting Nanoparticles inside Transparent Silica Monoliths.**
M. Bouazaoui, H. El Hamzaoui, A. ChahadiH, O. Robbe, K. Raulin, S. Turrell, B. Capoen. Nano - S&T, 23-26 October 2011, Dalian, China.

3- **Metallic and semiconductor nanostructures in glasses and microstructured fibers: structural and optical properties.**

A. Chahadih, , A. Lerouge, H. El Hamzaoui L. Bigot, R. Bernard ,G. Bouwmans , O. Cristini, C. Kinowski, B. Capoen and M. Bouazaoui, VCIAN, 20-25 Avril 2011, Las Vegas, USA.

4- **Croissance organisée et photo-assistée de nanoparticules de PbS dans des matériaux diélectriques.**

A. Chahadih, H. El Hamzaoui, R. Bernard, D. Jegouso, O. Cristini, B. Capoen, M. Bouazaoui, JFJPC11, 17-21 October 2010, Autrans, France.

5- **Localisation de la croissance de nano-cristaux pour l'optique.**

B. Capoen, H. El Hamzaoui, K. Raulin, A. Chahadih, O. Cristini, S. Turrell, R. Bernard, M. Bouazaoui, Matériaux, 18-22 Octobre 2010, Nantes, France.

6- **Photo-assisted growth of nanostructures in glasses: Structural and optical properties.**

H. El Hamzaoui, B. Capoen, R. Bernard, L. Bigot, A. Chahadih, K. Raulin, O. Robbe, S. Turrell, O. Stephan, P. Baldeck, M. Bouazaoui, VCIAN, 6-11 September 2009, St. Thomas, U.S. Virgin Islands.

7- **Laser space-selective precipitation of metallic or semiconductor nanoparticules inside transparent silica xerogels.**

H. El Hamzaoui, R. Bernard, A. Chahadih, D. Jegouso, L. Hay, B. Capoen, M. Bouazoui, Nano and Giga Challenges in Electronics, Photonics and Renewable Energy Hamilton, Ontario, Canada, 10-14 august 2009.

8- **Précipitation localisée de nanoparticules métalliques ou semiconductrices par laser dans un xerogel transparent de silice.**

H. El Hamzaoui, R. Bernard, A. Chahadih, D. Jegouso, L. Hay, B. Capoen, M. Bouazoui, JNOG, 6-9 juillet 2009, Lille, France.

Titre de la thèse : Photo-croissance organisée de nano-objets métalliques ou semiconducteurs dans les matériaux diélectriques destinés à la photonique

Ce sujet de recherche ambitionne le contrôle du procédé de réalisation in situ de nano-objets en matrice diélectrique en vue du développement de nouvelles applications. Les matrices de silice comportant des nanoparticules métalliques et semi-conductrices ont suscité un intérêt considérable en recherche fondamentale et appliquée dans le cadre de l'amélioration des catalyseurs, capteurs, ou de composant optiques linéaires et non linéaires. L'utilisation d'une irradiation laser est souvent mentionnée comme méthode prometteuse de croissance localisée. L'objet de ce travail est d'explorer les différentes possibilités de photo-cristallisation de différents types de nanoparticules dans des matrices poreuses ou vitreuses, en faisant varier les conditions de dopage et d'irradiation.

Dans cette thèse, des monolithes de silice poreuse produits par le procédé sol-gel ont été post-dopés et densifiés. Une méthode simple, basée sur une irradiation laser, a été développée pour localiser la croissance des nanoparticules semi-conductrices (PbS, CdS) ou métalliques (Au, Ag) à l'intérieur de la matrice de silice poreuse. Les nanoparticules sont précipitées localement sous la surface du xérogels de silice en utilisant un laser visible continu, ou encore dans son volume par une irradiation infrarouge en régime femtoseconde. Il est ainsi apparu qu'une croissance par irradiation en régime femtoseconde dans le domaine infrarouge procède de mécanismes tout à fait différents de ceux d'une synthèse par insolation continue, où le thermique a un rôle prépondérant. Par ailleurs, il est montré que la taille des nanoparticules peut être ajustée par le choix de la concentration des précurseurs dans la solution de post-dopage, par la longueur d'onde du laser, sa puissance ou par la température dans le cas de la précipitation thermique.

En outre, différentes méthodes ont été utilisées pour précipiter des nanoparticles métalliques (Ag, Cu) à l'intérieur d'une matrice de silice dense. Ces techniques sont basées soit sur la combinaison d'une insolation laser et d'un traitement thermique, soit uniquement sur des traitements thermiques sous des atmosphères différentes. La structuration spatiale de ces nanoparticules est effectuée par irradiation laser à impulsions, suivie d'un recuit à 600°C. Enfin, le dopage de verre massif par des nanoparticules de Cu a permis d'envisager leur utilisation pour fabriquer des cœurs de fibres optiques micro-structurées dopés. Les premiers tirages de capillaires ont montré que les nanoparticules de Cu peuvent être préservées après avoir subi une fusion à 2000°C.

Mots clés: Nanoparticules semiconducteurs, Confinement quantique, Nanoparticles métalliques, Résonance de plasmon de surface, Irradiation laser, Xerogels, Silice dense, Fibre optique.

Thesis title: Photo-assisted organized growth of metallic and semiconductors nano-objects in dielectric materials designed for photonics

The thesis project aims to master the localization and organization of metallic and semiconducting nano-objects formed inside sol-gel silica materials for novel applications. The nanostructuration method used in this thesis is based on the laser irradiation and, if necessary, heat-treatment. The local character of the matter-light interaction leads to the formation of nano-objects only in the irradiated areas. Hence, it is possible to control the spatial distribution of the nano-crystallites as well as their size distribution by varying the irradiation parameters.

In this thesis, porous silica monoliths produced via the sol-gel process were doped and densified. Different kinds of semiconductors (CdS, PbS) and metallic (Au, Ag) nanoparticles incorporated inside the porous SiO_2 matrix have been precipitated with the assistance of laser irradiation at room temperature or by an annealing process. The local generation of nanoparticles could be performed directly on the surface of the silica xerogel using a visible continuous laser or inside the volume of the matrix by a femtosecond laser irradiation. Moreover, it has been shown that the nanoparticle size could be adjusted by choosing the concentration of the precursors in the post-doping solution, the laser wavelength, the irradiation power and/or the annealing temperature in the case of thermal precipitation.

Furthermore, different methods were used to precipitate metallic nanoparticles (Ag or Cu) inside dense silica matrix. Those techniques are based on laser irradiations and/or heat treatments. Under pulsed laser irradiation, the space selective growth of noble metal nanoparticles was achieved in two steps: first, metallic nucleation centres were generated by the pulsed laser (nanosecond or femtosecond) in the irradiated areas; next, the metallic nanoparticles growth was obtained by annealing at 600°C. Besides, the doping of glassy matrices with copper nanoparticles allows foreseeing their use in the core of microstructured optical fibres. First capillary drawings have shown that the copper nanoparticles can be preserved after undergoing a melting at 2000°C.

Keywords: Semiconductor nanoparticles, Quantum confinement, Metallic nanoparticles, Surface Plasmon resonance, Laser irradiation, Xerogels, Dense silica, Optical Fibre.